UNIVERSITY OF SOUTHAMPTON

CIRCULATION AND FLUXES IN THE SUB-POLAR NORTH ATLANTIC

by

Sheldon Bacon

A dissertation submitted in candidature for the degree of Doctor of Philosophy at the University of Southampton Department of Oceanography.

February 1996

UNIVERSITY OF SOUTHAMPTON

ABSTRACT

FACULTY OF SCIENCE

OCEANOGRAPHY

Doctor of Philosophy

CIRCULATION AND FLUXES IN THE SUB-POLAR GYRE OF THE NORTH ATLANTIC

by Sheldon Bacon

This thesis is primarily concerned with inverse techniques which are developed and applied to hydrographic data. A standard linear inverse method with an established history is chosen, the application of which is intended to calculate geostrophic reference currents. The first development of the method is a means to estimate skill in the inversion solution; this is also used to assist in solution selection. The second development of the method concerns the finding of an optimal hydrographic configuration to input to the inversion.

The inverse method, with the above modifications, is applied to a data set which consists of three approximately 500-km-sided boxes of CTD stations, with vessel-mounted acoustic Doppler current profiles, collected as the U. K. Control Volume Experiment (CONVEX-91) during summer 1991 on the RRS *Charles Darwin* in the North Atlantic between Cape Farewell at the southern tip of Greenland and the European continental shelf west of Ireland. The East Greenland Current is represented by selected stations from the International Geophysical Year surveys of the R/V *Anton Dohrn*, because foul weather prevented CONVEX-91 from sampling there. Climatological wind stress data are used to estimate Ekman fluxes. We derive from the results an estimate of net (poleward) heat flux across the CONVEX-91 region (0.28±0.08 PW), and an estimate for the rate of freshwater gain by the Arctic Basin ($0.17\pm0.04\times10^6$ m^3s^{-1}). The results are compared, where possible, with work by previous authors. A quantified circulation scheme for the part of the Sub-Polar Gyre covered by the survey is presented, in which the most significant difference over previous schemes is that the Denmark Strait Overflow appears very weak – $5\text{-}6\times10^6$ m^3s^{-1}, compared with *ca.* 13×10^6 m^3s^{-1}.

TABLE OF CONTENTS

LIST OF FIGURES

LIST OF TABLES

ACKNOWLEDGEMENTS

Thanks are due to the officers and crew of the RRS *Charles Darwin* for demonstrating fortitude in adversity (good humour in bad weather). The quality of the CTD data was assured by Peter Saunders, Jane Read, John Gould, Pat Gwilliam (IOSDL), Mark Brandon (SPRI), and Chris Paulson (RVS). Particular thanks are due to Harry Bryden and Nick Fofonoff, and Peters Challenor, Killworth and Saunders, for advice and assistance; to Grant Bigg (UEA) and Peter Saunders, for providing some code on which I got started; and to John Gould, as Principal Scientist of RRS *Charles Darwin* cruise 62 (CONVEX-91), for handing me the job of doing something with the cruise data.

Supervisors were Dr. Kelvin Richards (Southampton University Department of Oceanography), Dr. John Gould (Institute of Oceanographic Sciences, for the first half of the study period) and Dr. Harry Bryden (James Rennell Centre, for the second half), all now affiliated to the Southampton Oceanography Centre.

This thesis is dedicated to my father, George William Bacon (1917–1995).

1. INTRODUCTION

1.1 Thesis outline

This thesis revolves around a data set collected in the Sub-Polar Gyre of the North Atlantic Ocean in summer 1991 as part of the U. K. contribution to the World Ocean Circulation Experiment (WOCE). The cruise, described in chapter 3, is called the Control Volume Experiment (CONVEX-91), and consists of three boxes of CTD stations defining the circulation between Cape Farewell at the southern tip of Greenland and the European continental shelf west of Ireland. This cruise, comprising modern, high quality hydrographic data, was ideally suited to (indeed designed for) the application of inverse techniques, which could be employed to attempt to determine geostrophic reference currents. Additional acoustic current profile data also suggested the possibility of some developmental work on the inverse methods, and so a project of wider scope was possible. Furthermore, since the ultimate goal of the data analysis was the determination of net fluxes of heat and freshwater across the CONVEX-91 region (approximately 55° N), this study came to view a few other topics as well. So the objectives of the thesis became (1) the development of new inverse techniques applicable to hydrographic data, (2) the testing of those techniques on a data set, and (3) the application of the techniques 'for real' with a view to deriving circulation and fluxes from the data set. Accordingly, this thesis is set out as follows.

Chapter 2 contains in its first section a critical review of the inverse methods employed here, and in its second section, a review of the standard method of calculating oceanic heat flux, wherein an inconsistency is identified and 'cured'. Chapter 3 describes the cruise and data. Chapter 4 sets out the first piece of development work on the inverse method, describing a new method for assessing skill in the inverse solution, which can be used to guide the choice of solution itself. Chapter 5 describes the second such piece, whereby an optimal solution (in fact, an optimal hydrographic configuration) is sought. Chapter 6 contains the main hydrographic results, consequent on the application of the preceding developments.

In particular, we present, and compare with work by previous authors, the net heat and salt fluxes across the CONVEX-91 region, and estimate the rate of freshwater gain by the Arctic Basin, together with estimates of error on these quantities. A self-consistent circulation scheme derived from these results is also presented and compared. In section 7 we summarise the conclusions from this thesis and discuss a few points about inversions which experience suggests may be true, but which we cannot presently prove. We conclude with indications of the direction of likely future work.

1.2 Contexts

There are broad scientific contexts which inform this thesis. One is the global heat balance. We quote from Bryden (1993; first paragraph): "The earth gains heat from the sun in the form of short-wave incoming radiation principally in the tropical regions, but radiates heat back to space in the form of outgoing long-wave radiation nearly uniformly over all latitudes. Thus, there is a net radiational heating of the earth equatorward of about 35° latitude and a net radiational cooling poleward of 35°. Since there is little storage of heat by the earth, particularly averaged over an annual period, compared with the latitudinal imbalances, the atmosphere and ocean must transport heat poleward from the tropical regions to the polar regions in order to maintain the observed radiation balance at the top of the atmosphere."

Now the distribution of the earth's total incoming and total outgoing radiation are becoming increasingly well-established, by top-of-the-atmosphere satellite radiation measurements; eg, Stephens, Campbell and Vonder Haar (1981). The difference between incoming and outgoing gives a picture of the net (zero mean) radiation imbalance by latitude; and any understanding of the maintainence of the present climate of the planet must be able to account for the partition between atmosphere and ocean of the net poleward heat flux (eg, Gleckler and Randall, 1995). The disagreements between satellite, atmospheric and oceanic heat flux estimates are described in Bryden (1993) and will not be rehearsed here, but suffice it to say that direct estimates of ocean heat fluxes, in each ocean and at representative latitudes in both hemispheres, are crucial for scientists ultimately to arrive at an understanding of the maintenance of the present global heat balance, and there are presently rather few of these direct estimates. If the present balance can be accounted for, one might then be able to place more confidence in predictions of climate change. One goal of this thesis, therefore, is the production of a new, direct estimate of (meridional) oceanic heat flux for the CONVEX region.

As well as heat flux, there is interest in measuring freshwater flux: the addition to and removal from the ocean surface of freshwater by continental run-off (including ice) and over-ocean precipitation and evaporation. Here too, oceanic estimates are required for comparison with atmospheric model-derived estimates, and with surface estimates. There are many levels of interest in the oceans' rôle in the global hydrological cycle; from the weak forcing of the ocean circulation by the freshwater flux (the Goldsborough circulation; eg, Huang, 1993), to the rôle of hydrological processes in ocean-atmosphere interactions (eg, Webster, 1994), to the apparent ability of the freshwater flux to change the state of the global ocean-atmosphere system in a drastic, climatic sense (eg Broecker *et al.*, 1990; Broecker, 1991; Rahmstorf, 1994, 1995; Manabe and Stouffer, 1995). Another goal of this thesis is the calculation of salt flux across the CONVEX region, and, with the aid of other data sources, the calculation of a freshwater budget for the entire Arctic basin.

The location for the CONVEX survey was selected with a view to the relative paucity of modern measurements in the vicinity of the Sub-Polar Gyre of the North Atlantic. After the comprehensive work of the International Geophysical Year surveys of 1957-58 (Dietrich, 1969), supplemented by the R/V *Erika Dan* cruise of 1962 (Worthington and Wright, 1970), the only published major oceanographic visit to the Sub-Polar Gyre was part of the Transient Tracers in the Ocean (TTO) program in 1983 (Scripps, 1986), so that 'modern' circulation schemes which include the Sub-Polar Gyre, such as Schmitz and McCartney (1993) and Reid (1994), rely largely on old data for the area. The Sub-Polar Gyre is an area of some significance in the global thermohaline circulation. In Broecker's (1991) now famous Conveyor Belt model of the overturning circulation, warm water flows north in the surface layers of the North Atlantic and cold water flows south in the deeper layers. The Sub-Polar Gyre straddles the northern extremity of the Conveyor Belt, where the overturning is shown as occuring in the simplified schematic. We hope that eventually a comprehensive modern view of the circulation in the Sub-Polar Gyre (and the whole north-east Atlantic) will emerge as a result of a group of research cruises carried out in 1990-91, of which CONVEX was one. We intend to present here a circulation scheme derived from the CONVEX data for comparison with other schemes, to indicate where there is evidence for changes in circulation, or at least inconsistencies with previous studies.

2. THE BOX INVERSE METHOD AND CALCULATION OF OCEANIC HEAT FLUX

There is a number of topics covered in this thesis which are best reviewed in situ; for example: optimisation, which has one oceanographic source paper; freshwater flux, the practicability of the calculation of which is usefully illustrated by a simple example; net flux calculation per se, which has been applied successfully in only a handful of locations in the World Ocean; and North Atlantic circulation, which is a vast topic that has received fine recent synthetic reviews of much fragmentary and asynoptic material, to which reference is made in the appropriate chapter, together with selected references appropriate to the present region of interest. Therefore we choose to separate out two topics for specific review in this chapter: inverse methods (in section 2.1) and oceanic heat flux calculation (in section 2.2). While there has been much work on technical development and wider application of inverse methods over the past twenty years or so, very little effort has gone into explicit verification of inverse results. We expand on this comment below, and set out some weaknesses of the method which have been largely bypassed.

Secondly, while inspecting the standard and apparently well-established method of oceanic heat flux calculation (essentially, how to convert potential temperature fluxes into heat fluxes), an inconsistency came to light which we describe and 'cure' below.

2.1 Application of inverse methods to oceanographic problems

Killworth (1983) finds the historical place of hydrographic inversions to be the latest in four discernible levels of dynamics in the literature on large-scale circulation, starting with the inference of flow direction in Wüst's (1935) core-layer method which argues the necessity of spreading from an identifiable source of water of distinct properties. The second level is the dynamic method (Defant, 1941) which uses the geostrophic relationship to relate the vertical shear of flow normal to a hydrographic section to the horizontal density gradient within the section. This method requires the assumption of a constant of integration (in proceeding from shear to current) which is conventionally treated as a level of no motion, defined on pressure or a measure of density, throughout the section, and is usually selected on a Wüstian basis either as a level believed to be within a stationary layer, or as a dividing level between two layers believed to be moving in opposite directions. The development of the third dynamical level, the construction of basin- to global-scale two-dimensional maps of geopotential anomaly between pressure surfaces, was stimulated by the increase in quantity of available data (eg, Leetmaa, Niiler and Stommel, 1977). Finally, the inverse method uses the same physics (geostrophy) at least, but imposes conservation requirements as constraints, thereby generating such self-consistency as is required over the (large) scale of the complete solution.

Since Killworth (1983) appeared, work has moved on, and one may now add a fifth level of sophistication: data assimilation (eg, Ghil and Malanotte-Rizzoli, 1991, and references therein). In this case, a time-dependent model (with as high a degree of dynamical complexity as is required) is forced to pursue a path in model state-space by constraining it to follow such real ocean data as are available. So we see inverse methods in a slightly different light: they are the special stationary (time-independent) case of the data assimilation approach to incorporating data into models.

Now to justify the choice of a particular inverse method. There are several available, and the box method, described below, was selected because the cruise pattern (see chapter 3) was adopted with the application of this method in mind. As additional reasons however, of two of the alternatives, we do not use the Bernoulli method (Killworth, 1986) because another worker (Sherliker, in prep.) is applying it to the same data, although no results are yet available. Nor do we use the Beta-Spiral method (Schott and Stommel, 1978), which is more applicable to studies where the reference velocity to be added to the geostrophic profiles is likely to be constant in magnitude and direction over the study area. This requirement results from the nature of the Beta-Spiral inversion solution, which is a single two-dimensional reference current vector. There is also Mercier's (1986) non-linear method, which is attractive; but we wanted to use the linear box method (amongst other reasons) because of features possessed by the so-called Model Resolution Matrix, which will be described in Chapter 4.

We describe now the motivation for the inverse model development work in chapter 4 (estimation of skill in the inverse solution), which led to further development, presented as the optimisation work in chapter 5. The simple linear inverse technique as applied to hydrographic data is used to compute reference velocities for geostrophic velocity profiles. This is done by requiring property and volume flux conservation through a closed circuit of hydrographic stations and applying suitable constraints to the resulting system of equations. This technique now has an established history and has been applied many times; it is known as the Wunsch (1978; referred to hereafter as W78) or box inverse method. However, since the inception of inversion, no such technique had (until Mercier *et al.*, 1993) been demonstrated to possess 'skill', either absolutely (in that the solution may reproduce an independently known feature of the real world) or relatively (in that the solution may improve on the results of a classical level-of-no-motion analysis). Indeed the most cogent attempt at comparison of different inverse methods with classical hydrographic analysis, Killworth and Bigg (1988), is based on model data and concludes that their null hypothesis of velocities computed from the geostrophic shear assuming zero velocity at the bottom out-performed all of the inverse techniques (Box, Beta-spiral and Bernoulli) in most of the scenarios in the study. Furthermore, Wunsch (1986) states that "any real controversy [over the use of the inverse method] will be resolved by the extent to which inverse methods are found by the oceanographic community to be useful". A suspicion remains that a solution to an underdetermined problem may not contain enough information to be 'right'.

The need for a means of gauging the success of inversions has been evident since W78; the discussion in that paper of the results of applying the inversion solutions to the geostrophic flows of the models therein exemplifies the approaches of most subsequent authors to solution 'gauging'. W78 first notes what one might call (unfairly) the 'cosmetic' effect of inversion solutions on the appearance of computed current sections in that the horizontally-layered 'push-pull' flow of the classical level of no motion analysis is replaced by a vertically-cellular current structure. The W78 Gulf Stream is set beside Richardson's (1977) current meter measurements, and the absence of an obvious level of no motion in the latter, taken as a true picture of the Gulf Stream, is noted. Secondly, comparability is noted between the W78 pictures of North Atlantic transports and the traditional work of previous authors such as Stommel (1965). Thirdly, qualitative (directional and order of magnitude) agreement is noted between a particular feature of model circulations (southward deep flow on the west flank of the Bermuda rise) and (non-contemporaneous) current meter measurements in the same area by Schmitz (1976).

The only available quantitative proof of skill in an inversion rests in Mercier *et al.* (1993). They incorporate float data into a non-linear stationary inversion of North Atlantic circulation and in finding that the floats do not add much new information to the inversion, they also find as a corollary that the inversion solution is to some extent parallel to the float data. Their figure 18 panels B and C show histograms of differences between float and inverse model velocities. The model of figure 18B is made from hydrographic data and dynamic constraints; that of figure 18C includes these and also float constraints. There is a significant reduction of residual (model minus data) variance from the former to the latter.

With the foregoing exception, most studies which apply inverse techniques have made comparisons of the second kind mentioned above, between transport estimates, which are not satisfactory as an independent test of inversion skill because transports are not prognostic quantities. The currents by which they are formed are sums of 'first guess' and inversion solution currents and so cannot provide a 'clean' test of inversion performance. However desirable transports may be as diagnostic quantities, I decided that any comparisons made in this study should consider only the direct product of the inversion process. That is the solution vector, which, in the simple model employed herein, is comprised of the geostrophic reference currents. Validation of the solution will be sought in independent estimates of those currents.

2.1.1 The linear inverse problem: set-up

Firstly we describe the mechanics of the box inverse method. Assume j=1,...,N station pairs form a closed circuit (which may or may not include coastline) about a volume of ocean. We can say that (approximately) the net flux of volume or some property through the volume is zero; so if T_j is the flux through station pair j,

$$\sum_{j}^{N} T_j = 0 \qquad (2.1)$$

Further, if the volume is divided horizontally into layers (where the top and bottom of each layer are defined by measures of density, or potential temperature, or any other suitable measure, plus the sea surface and bottom where appropriate, or some suitable combination) such that i=1,...,M conservation statements are written for some or all of the layers, then

$$\sum_{j}^{N} T_{ij} = 0 \qquad \text{for } i=1,\dots,M \qquad (2.2)$$

assuming no cross-layer flux. Now write the total velocity normal to the line between each station pair as the computed geostrophic velocity $v_j(p)$ plus the unknown reference velocity b_j

$$v_j = v_j(p) + b_j \qquad (2.3)$$

Take layer i in station pair j to have depth limits p_{ij}, p_{ij}', and the profile of some property θ (its variation with depth) to be $\theta_j(p)$; then the transport T_{ij} of that property is

$$T_{ij} \;=\; \Delta x_j \int_{p_{ij}}^{p'_{ij}} v_j(p)\,\theta_j(p)\,dp \;+\; \Delta x_j b_j \int_{p_{ij}}^{p'_{ij}} \theta_j(p)\,dp \qquad (2.4)$$

where Δx_j is station separation for pair j. Now define matrix and vector elements as

$$\{G_{ij}\} = \Delta x_j \int_{p_{ij}}^{p'_{ij}} \theta_j(p)\,dp \qquad (2.5.1)$$

$$\{m_j\} = b_j \qquad (2.5.2)$$

$$\{d_i\} = -\sum_j^N \Delta x_j \int_{p_{ij}}^{p'_{ij}} v_j(p)\,\theta_j(p)\,dp \qquad (2.5.3)$$

Inserting (2.4) into (2.2) and using (2.5) gives

$$\sum_j^N \{G_{ij} m_j\} = d_i \qquad \text{for } i=1,\ldots M \qquad (2.6.1)$$

or in matrix notation

$$\mathbf{Gm} = \mathbf{d} \qquad (2.6.2)$$

It is required to find the vector of unknown reference velocities **m**. The problem is one of matrix inversion, where some inverse of **G** is required, $\mathbf{G}^{-}$, such that an estimate of **m** ($\mathbf{m}^{est}$) can be obtained:

$$\mathbf{m}^{est} = \mathbf{G}^{-}\mathbf{d} \qquad (2.7)$$

In the hydrographic case, there are usually fewer constraints (M) than equations (N) so the system is underdetermined. The 'generalised inverse' due to Penrose (1955) is given as $\mathbf{G}^{+}$ in (2.8) below and could be used to invert **G** but would be prone to failure;

$$\mathbf{G}^{+} = \mathbf{G}^{T}\left(\mathbf{G}\mathbf{G}^{T}\right)^{-1} \qquad \text{(M<N, underdetermined)} \qquad (2.8.1)$$

$$\mathbf{G}^{+} = \left(\mathbf{G}^{T}\mathbf{G}\right)^{-1}\mathbf{G}^{T} \qquad \text{(M>N, overdetermined)} \qquad (2.8.2)$$

If two of the layer equations were the same then the system would be rank deficient and the product in parentheses in (2.8) would be singular. To handle such systems, Lanczos (1961) introduced the 'natural' inverse which was first applied to geophysical problems reducible to the form of (2.6) by Backus and Gilbert (1967, 1968, 1970). Particularly useful reviews and commentaries are given by Lanczos (1961), Jackson (1972), Wiggins (1972), Lawson and Hansen (1974), Parker (1977), Jackson (1979) and Menke (1989), amongst others. This mechanism was first transferred from solid-earth to hydrographic use by Wunsch (1978), but with the immediate difficulty recognised that it was no longer being applied to a stationary structure. We examine such assumptions as stationarity in more detail below (2.1.7).

2.1.2 The natural inverse

Following Lanczos (1961): two sets of eigenvectors $\mathbf{u}_i$ and $\mathbf{v}_j$ may be found such that

$$\mathbf{G}\mathbf{v}_j = \lambda_j \mathbf{u}_j \qquad \mathbf{G}^T\mathbf{u}_i = \lambda_i \mathbf{v}_i \tag{2.9.1}$$

$$\text{or} \quad \mathbf{G}^T\mathbf{G}\mathbf{v}_j = \lambda_j^2 \mathbf{v}_j \qquad \mathbf{G}\mathbf{G}^T\mathbf{u}_i = \lambda_i^2 \mathbf{u}_i \tag{2.9.2}$$

for j=1,...,N and i=1,...,M. The eigenvalues (with corresponding eigenvectors) are ranked in decreasing order of magnitude, forming a diagonal matrix such that

$$\lambda_i = \lambda_j \quad \text{if} \quad i = j \quad \text{and} \quad i \le q$$

$$\lambda_i = 0, \quad \lambda_j = 0 \quad \text{if} \quad i, j > q$$

for some integer q such that $q \le \min(M, N)$. The matrix **G** can be factored into the product

$$\mathbf{G} = \mathbf{U}\Lambda\mathbf{V}^T \tag{2.10}$$

where **U** is an (M×q) matrix whose columns are the eigenvectors $\mathbf{u}_i$, i=1,...,q; and **V** is a (q×N) matrix whose columns are the eigenvectors $\mathbf{v}_i$, i=1,...,q; and Λ is the diagonal matrix of q eigenvalues. This representation is called the spectral or singular-value decomposition (SVD). There remain (M-q) eigenvectors $\mathbf{u}_i$ and (N-q) eigenvectors $\mathbf{v}_i$ which correspond to zero eigenvalues; these are also assembled into matrices $\mathbf{U}_0$ (M×{M-q}) and $\mathbf{V}_0$ (N×{N-q}). If q=M, then **U** contains the complete set of eigenvectors of the symmetric matrix $[\mathbf{G}\mathbf{G}^T]$ and is therefore an orthonormal modal matrix; similarly, if q=N, then **V** contains the complete set of eigenvectors of the symmetric matrix [$\mathbf{G}^T\mathbf{G}$], and is therefore an orthonormal modal matrix. Were **G** square and of full rank (q=M=N), the system would be fully determined. However the 'shortage' of defining equations (constraints) means that no information is provided about the part of the solution **m** that lies in the so-called 'null space'.

The completeness of the eigenvector sets $\mathbf{u}_i$, i=1,...,M and $\mathbf{v}_j$, j=1,...,N enable the data vector **d** and the model parameters **m** to be written as sums of the relevant eigenvectors, thus:

$$\begin{aligned} \mathbf{d} &= \sum_{j=1}^{N} \beta_j \mathbf{u}_j = \sum_{j=1}^{q} \beta_j \mathbf{u}_j + \sum_{j=q+1}^{N} \beta_j \mathbf{u}_j \\ &= \mathbf{U}\, \mathrm{b} + \mathbf{U}_0\, \mathrm{b}_0 \end{aligned} \qquad (2.11.1)$$

and similarly

$$\mathbf{m} = \mathbf{V}\alpha + \mathbf{V}_0\,\alpha_0 \qquad (2.11.2)$$

Substitution of (2.10) and (2.11) into (2.6) gives:

$$\mathbf{U}\Lambda\mathbf{V}^{\mathrm{T}}\left[\mathbf{V}\alpha + \mathbf{V}_0\,\alpha_0\right] = \mathbf{U}\beta + \mathbf{U}_0\,\beta_0 \qquad (2.12)$$

The least-squares-type solution is found by minimising the length (the L_2 norm) of the residual vector ε, where ε=**Gm-d,** such that

$$\left\|\varepsilon\right\|^2 = \left\|\Lambda\alpha - \beta\right\|^2 + \left\|\beta_0\right\|^2 \qquad (2.13)$$

using the orthonormality of the eigenvectors; (2.13) is minimised when

$$\alpha = \Lambda^{-1}\beta \qquad (2.14)$$

leaving the least square error $\left\|\beta_0\right\| = \left\|\mathbf{U}_0^{\mathrm{T}}\mathbf{d}\right\|$; an exact solution exists only if this term is zero, which must be the case if q=M, when $\mathbf{U}_0=\mathbf{0}$. However, the solution is unique only if q=N; if q<N, the system is underdetermined and the elements of α_0 may be

set arbitrarily, since they do not appear in (2.13). Consider now the natural inverse of Lanczos (1961) which is set as

$$\mathbf{G}^{-} = \mathbf{V}\,\Lambda^{-1}\,\mathbf{U}^{\mathrm{T}} \tag{2.15}$$

from which $\mathbf{m}^{\mathrm{est}} = \mathbf{V}\,\Lambda^{-1}\,\mathbf{U}^{\mathrm{T}}\mathbf{d}$. Inserting $\beta = \mathbf{U}^{\mathrm{T}}\mathbf{d}$, derived from (2.11.1) with application of orthonormality conditions, and (2.14) into (2.11.2), it can be seen that the natural inverse, as well as being the solution of minimum ε, is also the solution of minimum **m**, since

$$\left\|\mathbf{m}\right\|^{2} = \left\|\Lambda^{-1}\beta\right\|^{2} + \left\|\alpha_{0}\right\|^{2} \tag{2.16}$$

and with the first term fixed, the second term is minimised by $\alpha_0=\mathbf{0}$. From the mechanics of the solution, it can be seen that the natural inverse gives the least-square-error solution with minimum perturbation from an assumed initial flow field in the hydrographic problem.

The creation of an unique solution to an underdetermined system requires the imposition of extra (artificial) constraints; in the present case, those constraints are described above. However, the prior indeterminacy allows an infinite number of solutions; selecting just two of those, that due to the inversion process ($\mathbf{m}^{\mathrm{est}}$) and an imagined one held to represent 'truth' ($\mathbf{m}^{\mathrm{true}}$) allows the following:

$$\mathbf{G}\mathbf{m}^{\mathrm{est}} = \mathbf{d} \quad \text{and} \quad \mathbf{G}\mathbf{m}^{\mathrm{true}} = \mathbf{d} \tag{2.17}$$

$$\text{so} \quad \mathbf{m}^{\mathrm{est}} = \mathbf{G}^{-}\mathbf{G}\mathbf{m}^{\mathrm{true}} = \mathbf{R}\mathbf{m}^{\mathrm{true}} \tag{2.18}$$

where **R** is called the model resolution matrix and describes how the inverse solution is a filtered impression of the truth. Using the decomposition of (2.10),

$$\mathbf{R} = \mathbf{V}\,\Lambda^{-1}\,\mathbf{U}^{\mathrm{T}}\mathbf{U}\,\Lambda\,\mathbf{V}^{\mathrm{T}} = \mathbf{V}\mathbf{V}^{\mathrm{T}} \tag{2.19}$$

The model resolution matrix is open to simple interpretation only if it is similar to the identity matrix; then, each element of the inverse solution is equal to a weighted average over a few corresponding values of elements of the 'true' solution. The resolution matrix will be discussed at greater length below.

2.1.3 Weighting

Each element of the solution vector **m** is effectively scaled by the cross-sectional area of its station pair thus putting high velocities between wide, deep station pairs and low velocities between narrow, shallow ones. To illustrate this, take a section of N stations, impose one constraint of total mass conservation so that **G** is [1×N] and **m** is [N×1], and write the Moore-Penrose inverse ($\mathbf{G}^+$) to solve:

$$\begin{aligned}\mathbf{m} &= \mathbf{G}^{+}\mathbf{d} \\ &= \mathbf{G}^{\mathrm{T}}\left(\mathbf{G}\mathbf{G}^{\mathrm{T}}\right)^{-1}\mathbf{d} \qquad (2.20)\\ \{m_i\} &= G_i\left(\frac{d}{\sum_{i=1}^{N} G_i^2}\right) \quad \text{for } i = 1,\ldots,N\end{aligned}$$

Each element of **G** is the station pair cross-sectional area, so we see each solution element in this simple example is directly proportional to that cross-sectional area.

This is countered, following W78, by rewriting (2.6) as

$$\mathbf{G}\mathbf{W}^{-1/2}\mathbf{W}^{1/2}\mathbf{m} = \mathbf{d} \quad \text{or} \quad \mathbf{G}'\mathbf{m}' = \mathbf{d} \qquad (2.21.1)$$

where $\mathbf{G}' = \mathbf{G}\mathbf{W}^{-1/2}$ and $\mathbf{m}' = \mathbf{W}^{1/2}\mathbf{m}$ (2.21.2)

W is chosen to be diagonal, with elements

$$W_{ii} = D_i \Delta x_i \qquad (2.22)$$

where D_i is the water depth between station pair i. Thus the condition of least square error remains unchanged, but the solution length to be minimised changes from $\mathbf{m}^{\mathrm{T}}\mathbf{m}$ to

$$\left(\mathbf{m}'\right)^{\mathrm{T}}\mathbf{m}' = \left(\mathbf{W}^{1/2}\mathbf{m}\right)^{\mathrm{T}}\mathbf{W}^{1/2}\mathbf{m} = \mathbf{m}^{\mathrm{T}}\mathbf{W}\mathbf{m} \qquad (2.23)$$

The desired solution is recovered by calculating $\mathbf{m} = \mathbf{W}^{-1/2}\mathbf{m}'$.

A desirable feature resulting from this weighting scheme is that if one chooses volume flux from top to bottom over the whole section as the sole constraint, then all resulting solution vector components are the same; ie, this is the same as adjusting the flux balance by applying a constant velocity correction across the section. This is mentioned in Wunsch and Roemmich (1982), and we briefly set out how this comes about. The rest of the working in this section is derived by the present author. **G** is [1×N], **m** is [N×1] (both vectors) and **d** is [1×1], a scalar, equal to the negative of the amount by which the section flux exceeds zero. The value of each element of **G**, $\{G_i\}$, is the top-to-bottom cross-sectional area (a_i) of the station pair:

$$\{G_i\} = \Delta x_i\, D_i = a_i \tag{2.24}$$

The weighting scheme gives $\{W_{ii}\} = a_i$, so following (2.20.2) gives for each element of $\mathbf{G}'$, $\{G_i'\}$

$$\{G_i'\} = \sqrt{a_i} \tag{2.25}$$

For the SVD, **U** is [1×1], length 1, so $\mathbf{U} = \{u_{11}\} = 1$. Also, Λ is [1×1], size to be determined. So $\mathbf{V}^T$ is proportional to $\mathbf{G}'$ and length 1, from which we get, using κ for a scale factor:

$$\|\mathbf{V}\|^2 = \|\kappa\mathbf{G}'\|^2 = \kappa^2\|\mathbf{G}'\|^2 = 1 \tag{2.26.1}$$

$$\frac{1}{\kappa^2} = \sum_i^N G_i'^2 = \sum_i^N a_i = A \tag{2.26.2}$$

where A is the total section cross-sectional area. So the eigenvalue (λ) and each element of **V**, $\{v_i\}$, are given by

$$\{v_i\} = \sqrt{a_i/A} \quad \text{and} \quad \lambda = \sqrt{A} \tag{2.27}$$

and the elements of the inverse of $\mathbf{G}', \{G_i'^-\}$, are given by

$$\left\{G_i'^-\right\} = \frac{\{v_i\}}{\lambda} = \frac{\sqrt{a_i}}{A} \qquad (2.28)$$

Now the solution elements $\{m_i\}$ are recovered as follows, remembering that **d** is [1×1]:

$$\begin{aligned}\{m_i\} &= W_{ii}^{-1/2} G_i'^- d \\ &= \frac{1}{\sqrt{a_i}} \frac{\sqrt{a_i}}{A} d \qquad (2.29) \\ &= d/A\end{aligned}$$

which, finally, is the usual result: a uniform current correction equal to total flux excess divided by total section area.

Next, in order that each property transport equation (each row) of (2.6) be not weighted by either the magnitude of the units or the range of measured values of the property θ being transported, each property is standardised and normalised to θ':

$$\theta_i'(p) = \frac{\theta_i(p) - \bar{\theta}}{\sigma} \qquad (2.30)$$

where $\bar{\theta}$ is the overall mean value of the variate and σ its standard deviation for each box.

2.1.4 Indeterminacy

When written out in vector form, the solution $\mathbf{m}^{est}$ derived from the natural inverse (2.15) is

$$\mathbf{m}^{est} = \mathbf{W}^{-1/2} \sum_{i=1}^{q} \left(\frac{\mathbf{u}_i^T \mathbf{d}}{\lambda_i} \right) \mathbf{v}_i \qquad (2.31)$$

Subjectivity enters the inversion process in the choice of value for q. Since the eigenvectors **v** are placed in decreasing order of eigenvalue λ (as index i increases), then increasingly large components are added to the solution $\mathbf{m}^{est}$ by the presence of $1/\lambda$ in the coefficient to each **v**. This poses no problem if the constraints which contribute significantly to the solution give rise to an ‘obvious’ cut-off such that the

$(q+1)^{th}$ and subsequent eigenvalues are actually or effectively zero. The ambiguous case arises when the eigenvalues slide continuously from 'high/significant' to 'low/insignificant', when one should impose a criterion of significance in order to choose a value for q. All of the foregoing assumes that a meaning has been developed for significance.

In fact two strategies have been adopted by previous authors in order to avoid having to consider significance explicitly, both of which have recourse to the related subjective notions of 'obviousness' and 'reasonableness', where application of the former has assumed the latter. One strategy requires the selection of a small number of layers, typically four, in the enclosed region, so that few eigenvalues result, all of which contribute to the solution. In simple terms, this may represent identification of layers with distinct water masses, each of which contains information orthogonal to the others. The choice of a value for q is thus 'obvious' and implicitly 'reasonable'; eg, W78, Thompson and Veronis (1980), Fiadero and Veronis (1982, 1983), van Aken (1988). The alternative strategy requires the much finer subdivision of the water column into (say) twelve to eighteen layers so that as much information as possible is extracted from the system, with the additional consequence that the available information is spread more thinly. When multiplied by the number of properties to be conserved in each layer, there may then be several tens of constraints (by no means all providing mutually orthogonal information) with the result that significant and insignificant eigenvalues are separated by a range of 'partially significant' eigenvalues such that the actual solution is relatively insensitive to exactly where the cut-off point is placed, and thus a corresponding range of 'reasonable' values for q exists. Beyond this range, the solution becomes 'unreasonable' in an 'obvious' fashion: eg, Roemmich (1980), Fu (1981), Wunsch and Grant (1982), Wunsch, Hu and Grant (1983), Wunsch (1984), Roemmich and Wunsch (1985), Joyce, Wunsch and Pierce (1986; JWP hereafter). JWP demonstrates the use of a means of selecting the cutoff whereby the subjectivity described above is formalised. Levenburg-Marquardt analysis, described by Lawson and Hanson (1974), involves the display of solution magnitude against solution residual magnitude for each solution degree. As the solution magnitude increases, the residual magnitude decreases, and the 'best' solution is interpreted as a point on the curve where solution magnitude increases for little reduction in residual magnitude.

A cut-off may be selected in a similar fashion by use of the ridge regression procedure (Hoerl and Kennard, 1970a,b), also known as damped or tapered least squares, in which a weighted combination of residual error and solution length is minimised; within the SVD formalism, this results in the λ^{-1} terms in the solution (2.31) being multiplied by $\left(1-[\nu/\lambda]^2\right)^{-1}$. Instead of requiring the arbitrary selection of a cut-off value for solution degree q, this mechanism requires the equally arbitrary selection of a 'noise level' ν for the eigenvalues. Thus the full rank solution may be developed but the components due to eigenvalues of order ν and smaller are damped out.

2.1.5 ADCP data in inversions

It is worth considering separately the uses to which ADCP data have previously been put, where available, in the context of inverting hydrographic data. There are three relevant papers: JWP, Pierce and Joyce (1988) and Bingham and Talley (1991; BT hereafter). Of these, the second uses essentially the same method as JWP and will not be discussed.

It is noted firstly that ADCP performance is not very high quality in any of these papers, when compared with more recent standards. This is principally through (i) low signal penetration with depth, so that none of the above papers uses ADCP-derived current estimates from greater depths than 100m; and (ii) the quality of the then available navigation (satnav / LORAN), which is low compared with present-day GPS.

Secondly, there is no explicit consideration of the contribution of tidal currents (barotropic or internal) to the ADCP measurements. Such currents would appear, for example, as underestimates of model error in JWP. Pursuing the example of the location of JWP, one finds from the data of Schwiderski (1979) – see also Luyten and

Stommel (1991) – that the barotropic M2 tidal current for the offshore vertex of the sections is about 0.5 cm/s, but at the shallower inshore ends of the sections, it increases to 1.5 cm/s (south-west end) and over 10 cm/s (northern end). Furthermore, Hendry (1977) examined the semidiurnal internal tidal currents in the MODE area (centred on 70°W, 28°N), and found currents of order 1 cm/s throughout the water column. JWP's inversion error contribution from ADCP data is about 3 cm/s, and based solely on navigation errors; perhaps that value should be increased somewhat. Baines (1982) suggests that the eastern North American continental slope, Cape Cod to southern Grand Banks, is the fifth most energetic source of internal tidal energy in the world, with the East China Sea region (relevant to BT) second, and the Biscay-UK continental slope region first (relevant to part of the present study).

BT make two different uses of their ADCP data: (i) to provide a reference for their geostrophic profiles, both *per se* and as initialisations for their inversion, and (ii) as additional constraints in an inversion initialised by geostrophic profiles referenced to zero velocity at the bottom. Appealing to transport requirements, they found the ADCP-referenced geostrophy better than bottom referenced. For the inverse calculations, they preferred initialising geostrophy with ADCP data to using the ADCP data as extra constraints, since there is ambiguity introduced into the latter by the (relatively arbitrary) weight chosen for the ADCP data compared with the hydrographic transport constraints. Indeed their changes of weighting showed (their figure 13) that two distinct weighting-dependent regimes were present in the solution: a hydrographic-dominated one and an ADCP-dominated one, suggesting a degree of incompatibility between the two.

JWP use their ADCP data solely as constraints in their inversions. They run three inversions: (i) a 'combined' model incorporating hydrographic transport and ADCP constraints, (ii) a hydrography-only model and (iii) a model using ADCP constraints with total mass conservation. The latter two are intended as comparisons with the first. They prefer the first, giving as reasons for their preference that the solution is more nearly fully-determined (nearly as many constraints as equations), and that the mass transport residuals are left without perceived 'structure', indicating that no information remains in the system. Models (ii) and (iii) agree 'qualitatively' with the first.

In JWP it is stated that "a general rule of oceanic model making is that one should use everything one knows". This is true, but if it is read in context to mean that all available information should be included as inversion constraints, then I disagree. I show below that there is merit in withholding the ADCP data entirely from the inversion process so that it may be used as an independent test of the quality of the inversion solution.

2.1.6 Eigenvector structure

W78 noted that the eigenvectors produced by SVD progressed from representation of large spatial scales at low solution degrees to small scales at high degrees, and the observation has often been repeated. I offer a simple explanation for this: the spectrum of the ocean is red. SVD is an axis-rotation process in which the eigenvectors are the axes and the axial directions which are sought are those of maximum variance, so the projection of the data onto the first eigenvector removes the largest variance component (ie, the highest eigenvalue), the second eigenvector projection removes the largest remaining variance (the second highest eigenvalue), and so on. That the spectrum of the ocean is red means that as one looks at longer spatial and temporal scales, one sees progressively greater amounts of energy (variance). Wunsch (1972) shows quantitative time-spectrum results of periods from two minutes to two years of temperature variations in the main thermocline at Bermuda, in which energy increases with period. Similarly, Wells (1986) shows a qualitative spatial spectrum illustrating the energy possessed by various oceanic phenomena, in which energy increases with scale. So SVD of eddy-resolving large-scale ocean sections will put long-wavelength, high variance information into low degrees and short-wavelength, low variance information into high degrees. Eigenvector structure is thus determined by the design of the SVD itself as applied to the structure of the ocean, as one would expect.

2.1.7 Assumptions

The box inverse method has been set out and instances of its application described. We now step back to examine the assumptions behind the method in a little more detail, and we start from the discussion of scientific assumptions as set out in Wunsch and Grant (1982), who divide them into three categories:

(1) A. The ocean is in geostrophic balance

B. Mass and salt are conserved

(2) C. There is no major cross-isopycnal mixing except where water masses are in contact with the atmosphere.

(3) D. 'Instantaneous' hydrographic sections represent long-term average flows (no temporal aliasing).

and as a weaker alternative to D, they add

D′. Long spatial scales are more nearly time-independent than short scales.

They assert that the three categories represent some measure of increasing uncertainty, where none of the assumptions is strictly correct, but that in category 1 there is good theoretical and observational understanding of where and how they break down. There is general agreement that the geostrophic balance is adequate on the large scale; sea level does not fluctuate enough to represent any large change in water storage; and there is no significant atmospheric pathway for salt.

With regard to the category 2 assumption of no cross-isopycnal mixing, they say 'until one gets into positive trouble with assumption C it is a reasonable working hypothesis'. Many subsequent authors have chosen to include a measure of vertical exchange between layers in their calculations; for example, Wunsch and Grant (1982), who derive their estimates from integration of horizontal mass flux residuals; and Wunsch, Hu and Grant (1983), who include a measure of vertical exchange in their models. We have decided to keep to the simplest model in this thesis (no vertical exchange) while gaining experience with the method, in part because we are interested in developing means of verifying the inverse solution estimate, which we can do for horizontal (or near-horizontal, 'along-layer') flows with the aid of ADCP data (chapter 4), but which we have no way of doing for vertical (diapycnal, or cross-layer) flows, other than by indirect means. We are interested, however, in a project for the future involving attempting an inversion bracketing the Labrador Sea with its large convection signal, to see if a model including vertical fluxes can 'see' the net effects of the convection.

The category 3 assumption is the weakest. To show that time-dependence is important over much shorter scales than years (which confounded W78's first West Atlantic model, based as it was on sections collected over decades), Thompson and Veronis (1980) computed directly the sensitivity to non-synopticity in data from a highly variable region by replacing three stations in one of their sections by three others taken just three weeks later and found that the entire character of the deduced flow was changed.

Now consider a case, like the western end of CONVEX (see chapter 3), where an inflow to a box may be very closely matched (in topographic characteristics and orientation, and in property characteristics) by an outflow. A box inverse has no skill in determining large barotropic current components in this case. The SVD imposes the usual conditions of $\min\|\mathbf{m}\|$ and $\min\|\varepsilon\|$, where $\varepsilon = \mathbf{Gm}-\mathbf{d}$, the error vector. We detail the change in square length caused by adding an arbitrary outflow (+b) to element k of **m**, matched by the same inflow (–b) to element l of **m**; so

$$\begin{aligned} m_k' &= m_k + b \\ m_l' &= m_l - b \end{aligned} \tag{2.32}$$

Then the difference in square lengths of **m′** and **m** is:

$$\begin{aligned} \|\mathbf{m}'\|^2 - \|\mathbf{m}\|^2 &= \mathbf{m}'^{\mathrm{T}}\mathbf{m}' - \mathbf{m}^{\mathrm{T}}\mathbf{m} \\ &= (m_k + b)^2 + (m_l - b)^2 - m_k^2 - m_l^2 \\ &= 2b^2 \end{aligned} \tag{2.33}$$

if $m_k = m_l$. Plainly the solution length is increased by this action, so unless the solution is forced to hold the greater value, the minimum solution length constraint will prevent the solution from attaining the greater value. However, the solution error will *not.* prevent it, and so it should not, since it is both a valid solution and, we posit for the sake of argument, the correct solution.

Pursuing the same logic, consider layer (constraint) i, which is element i of ε:

$$\varepsilon_i = \sum_j G_{ij} m_j - d_i \tag{2.34}$$

summing over columns of G labelled j. Ignoring all elements except k and l, which are redefined as before:

$$\begin{aligned} \varepsilon_i' &= G_{ik}\left(m_k + b\right) + G_{il}\left(m_l - b\right) - d_i \\ &= G_{ik} m_k + G_{il} m_l - d_i \\ &= \varepsilon_i \end{aligned} \tag{2.35}$$

if $G_{ik} = G_{il}$ (ie, areas and property distributions are the same). So the solution error, which is unchanged by inserting the balanced inflow/outflow, accepts the alteration.

2.2 Calculation of oceanic heat flux

A brief canvassing of local colleagues led to the conclusion that many oceanographers, both observationalists and modellers, continue to use the wrong value of specific heat (C_p) to convert a potential temperature (θ) transport into a heat transport; furthermore, we believe that occasionally this is seen when reviewing oceanographic proposals and manuscripts. One problem, which we believe to be common, is the use of the freshwater value for specific heat (4187 J kg^{-1} K^{-1}) and not any value appropriate to oceanic salt water, which is about 5% less than the fresh water value (see Gill, 1982, Table A3.1). If as scientists we are trying to express facts about the world, the least we can do when quoting a heat flux in some multiple of watts is to be using the same meaning of 'watt' as other scientists.

A second starting point for this review of heat flux calculation is the simple question: which properties need to be known *in situ*, and which at the surface? The original demonstration of the feasibility of direct oceanic heat flux calculation is due to Bryan (1962), who derives the 'energy transport integral' across a zonal section as

$$\text{Total energy transport} \cong \int_{0}^{L} \int_{-H}^{0} c_p \theta \rho v \, dz \, dx \qquad (2.36)$$

by means of a Taylor series expansion about a reference state, where the integral dx is taken across the section (0 to L), the integral dz from the ocean bottom to the surface (-H to 0), θ is potential temperature referenced to the surface, ρ is density, v is velocity normal to the section, and C_p is heat capacity. Now the product ρv forms the mass flux so both must be *in situ*; and potential temperature is referenced to the surface; so what, in principle, is the correct value of C_p to use, given that $C_p = C_p(p, T, S)$, where p, T and S are pressure relative to sea surface, *in situ* temperature (temperatures throughout are in K) and salinity ? Bryan opts for the *in situ* value; however, we believe the surface value to be the appropriate one, so we provide a new derivation below to demonstrate this, and conclude with a statement of the full 'recipe' for heat flux calculation.

2.2.1 Derivation

One standard method of presenting fluxes from an ocean section is to calculate the net transport of θ across the section, giving a flux (say) in Sv °C (1 Sv = 10^6 m^3 s^{-1}). If the net volume flux across the section is zero so that there is no transport of the zero of the temperature scale, then the θ flux converts into heat flux by multiplying by ρC_p. Taking a representative in-situ density (ρ) of 1030 kg m^{-3}, a surface value for C_p of 3987 J kg^{-1} K^{-1}, and requiring that we end up with heat flux in PW (10^{15} W), means that 1 PW = 244 Sv °C is appropriate.

Should we be using volume flux in this way? Consider the process which defines θ. A parcel of water with properties (p, T, S) is raised adiabatically and isentropically to the surface, where its properties are (0, θ, S). Mass is conserved, not volume; so rather than compute volume and then θ fluxes, and converting the latter using a single density, one should compute mass flux using in-situ density in the first place. (It is our experience that this is normally done, but that the results are commonly presented in transport units of Sv). What then is the heat flux?

Before addressing this question, we turn for the fundamentals of ocean thermodynamics and fluid mechanics to Fofonoff (1962), Batchelor (1967) and Gill (1982), from which we get a statement of the first law of thermodynamics (t is time) describing the evolution of the internal energy per unit mass E:

$$\rho \frac{dE}{dt} = -P\,\mathrm{div}\mathbf{u} - \mathrm{div}\mathbf{F} + \rho\varepsilon \qquad (2.37)$$

wherein E can change through pressure work (RHS, 1st term; P is absolute pressure, **u** is 3-dimensional velocity), through the divergence of the total flux of heat by molecular processes including radiative exchange, conduction, the heat of mixing, etc. (RHS, 2nd term), and through such processes as the dissipation of mechanical energy into heat, chemical reaction, and change of phase (RHS, 3rd term).

We proceed by using the equation drawn from the second law of thermodynamics which introduces the state variable entropy, $dE = Td\eta - PdV + \mu dS$, where S is salinity, μ is the (specific) difference between the partial chemical potential of "salt"

μ_S and the partial chemical potential of water μ_W in seawater, V is specific volume and η is specific entropy. Now substituting for dE into the LHS of (2.37), we find that since $\rho P\,dV/dt = P\,\mathrm{div}\mathbf{u}$, this latter term cancels with the first term on the RHS of (2.37), so that we now have

$$\rho T\frac{d\eta}{dt} + \rho\mu\frac{dS}{dt} = -\mathrm{div}\mathbf{F} + \rho\varepsilon \tag{2.38}$$

Then we expand $d\eta$, either in (p, T, S), (2.39.1) or in (θ, S), (2.39.2):

$$d\eta = \left(\frac{\partial\eta}{\partial T}\right)_{P,S} dT + \left(\frac{\partial\eta}{\partial P}\right)_{T,S} dP + \left(\frac{\partial\eta}{\partial S}\right)_{T,P} dS \tag{2.39.1}$$

$$d\eta = \left(\frac{\partial\eta}{\partial\theta}\right)_{S} d\theta + \left(\frac{\partial\eta}{\partial S}\right)_{\theta} dS \tag{2.39.2}$$

Note that the implied constant pressure in (2.39.2) is the reference pressure of the potential temperature, ie, the sea surface pressure. We pursue the derivation substituting (2.39.2) into (2.38), since (2.39.1) merely involves one in the adiabatic lapse rate.

$$\rho T\left(\frac{\partial\eta}{\partial\theta}\right)\frac{d\theta}{dt} + \rho T\left(\frac{\partial\eta}{\partial S}\right)\frac{dS}{dt} + \rho\mu\frac{dS}{dt} = -\mathrm{div}\mathbf{F} + \rho\varepsilon \tag{2.40}$$

Next we use a Maxwell relation, $(\partial\eta/\partial S) = -(\partial\mu/\partial T)$, and the definition of specific heat, $(\partial\eta/\partial\theta) = C_p/\theta$, with C_p defined at the reference pressure of θ, consistent with (2.39.2), so that (2.40) becomes:

$$\rho C_p\frac{T}{\theta}\frac{d\theta}{dt} + \rho\left\{\mu - T\left(\frac{\partial\mu}{\partial T}\right)\right\}\frac{dS}{dt} = -\mathrm{div}\mathbf{F} + \rho\varepsilon \tag{2.41}$$

which is a complete and correct statement of the conservation of the 'non-mechanical' components of the internal energy of sea water. We return now to the question: what is the heat flux? Usually the salinity effects on the internal energy (the 2nd term on the LHS of (2.41)) are ignored, as are dissipation effects and negligible components of **F** (Bryan, 1962), so that a statement recognisable as just 'heat conservation' becomes:

$$\rho C_p \frac{T}{\theta}\frac{d\theta}{dt} = -\mathrm{div}\mathbf{F}' \qquad (2.42)$$

where we have given $\mathbf{F}$ a prime to indicate the discarding of negligible components over the $\mathbf{F}$ used previously. Obviously this expression is not ideal; it rather annoyingly contains T/θ, meaning that heat content is context-dependent, through the presence of T, although for the oceanic environment, the ratio is different from 1 by only about 0.1%.

Before proceeding, we provide a justification for the neglect of the salinity effects in (2.41). We want to compare $C_p\delta\theta$ with $(\mu - T\partial\mu/\partial T)\delta S$. We know that the former term is of order 10^4 J kg^{-1}. We turn to Feistel (1993) for estimates of chemical potential and find $\mu \sim 100$ J kg^{-1}, and $T\partial\mu/\partial T$ of similar magnitude and variable sign. Since $\delta S \sim 1$, we estimate the salinity term to be two orders of magnitude less than the temperature term. The salinity term is scrutinised in more detail (as a case study) in the Appendix to Macdonald, Candela and Bryden (1994).

A way around this is to use 'surface-equivalent' heat rate. For the ocean, most of the heat is added or removed at the surface; exceptions, such as kinetic energy dissipation and internal sources like black smokers, are negligible. Now regardless of how internal energy is transported internally, the quantity of interest is the amount of heat that can cross the surface of the ocean. At the surface, $T=\theta$ and so, defining the LHS of (2.42) as dQ/dt, the change in heat content following a fluid parcel, we now have $dQ/dt = \rho C_p d\theta/dt = -\mathrm{div}\,\mathbf{F}'$; this we now expand, integrating over the control volume, as:

$$\int \rho C_p \frac{\partial\theta}{\partial t}\, dV + \int \rho C_p \theta\, v\, dA = -\int F'\, dA \qquad (2.43)$$

where the first term on the LHS is the change in heat content of a fixed volume, the second term on the LHS is the advective heat flux across the boundaries of the volume (velocity v is the component normal to the surface element dA), and the RHS is the boundary flux (F' is the flux normal to dA). Treating the state of the control volume as (near-) stationary allows us to regard the first term in (2.43) as negligible.

It is as though in one's imagined control volume all mass elements are raised adiabatically and isentropically to the surface, then allowed to enter or exit the volume. Then the heat flux comprises θ and the surface value of C_p, and in-situ values of (p, T, S) provide the in-situ density.

We briefly consider errors resulting from the use of constants for ρ and C_p, instead of holding them as variables. Plainly the use of freshwater C_p involves a 5% bias. Use of a single representative value of ρ for a 'Sv°C–to–PW' conversion factor has an associated uncertainty of the range of in-situ values of oceanic density, 1020–1070 kg m^{-3}, or ±2%. Using a constant *surface* value of C_p ignores its (θ, S) dependences, which contribute a combined uncertainty of ±0.3% within reasonable oceanic values of (θ, S); this is compared with a range of over 4% due to its pressure dependence (and the extent to which θ is not a conservative variable).

2.2.2 *Summary*

Oceanic heat fluxes should be computed as follows. Zero net mass flux across the sections enclosing the control volume should be obtained (eg, Hall and Bryden, 1982, for the Atlantic Ocean at 24°N). Mass flux itself should be calculated as the area integral across each section of in-situ density and velocity. Heat flux is then a similar integral, with dA an area element of multiples of increments of along-track coordinate (dx) and vertical coordinate (dz), and v cross-track velocity on each section. Arguments defining functionality below are pressure, temperature and salinity, and reference pressure for θ.

$$\begin{aligned} \text{Mass flux} &= \oint dA\, \rho v = 0 \\ \text{Heat flux} &= \int dA\, \rho C_p \theta v \end{aligned} \tag{2.44.1}$$

where

$$\theta = \theta(p, T, S, p_{ref} = 0)$$

$$C_p = C_p(0, \theta(p, T, S, p_{ref} = 0), S)$$

$$\rho = \rho(p, T, S)$$

An extension arises from the use of hydrostatics (W. B. Owens, pers. comm., 1995), so that dA = dx dz, and $\rho\, dz = dp/g$ where g is the acceleration due to gravity, g = g(y) where y is latitude, giving an alternative form for heat flux:

$$\text{Heat flux} = \int\int dx\, dp\ \ C_p\, \theta\, v/g \qquad (2.44.2)$$

We shall use the above expressions later when calculating heat flux across the CONVEX region.

3. THE CONVEX-91 DATA SET

The CONVEX-91 (Control Volume Experiment) cruise took place between 1 August and 4 September 1991 on the RRS Charles Darwin, the intention being to contribute to the observation of the gyre-scale circulation of the North Atlantic in accordance with the World Ocean Circulation Experiment Implementation Plan (WOCE 1988a, 1988b) Core Project 3, the Gyre Dynamics Experiment. The aim was to occupy two continuous lines of full-depth CTD/O_2 stations between the UK continental shelf and Cape Farewell at approximately eddy-resolving station separation (ca. 50 km) and with the two main lines connected by short meridional sections thereby dividing the whole cruise pattern into three separate closed boxes or Control Volumes, here named as West, Centre and East boxes. This observational strategy renders the measurements into a form amenable to inversion. The cruise program is described in Gould (1992); some cruise results relating to North Atlantic climatology are described in Read and Gould (1992). Station positions and bathymetry are shown in figure 3.1; station sequencing is indicated by highlighting selected stations. A total of 96 numbered stations were occupied, of which numbers 40 and 79-82 were repeats and are not included here; also, bad weather prevented a cast from being made at position 8. Further consequences of the (unusually) bad weather were the omission of a station to complete the western meridional line (between stations 35 and 69) and, most seriously, the prevention of both main lines from reaching the Greenland continental shelf. The northern line had to stop, and the southern line could only resume, outside the East Greenland Current, so a small but significant element of the intended survey pattern is missing.

CTD data used here were collected using an NBIS Mark 3b instrument. The processed data were placed onto grids for each box with 10 m depth increments and proceeding anti-clockwise around each box: from station 35 and back for the West box, from station 10 and back for the Centre box, and from stations 96 to 1 for the East box. Geostrophic velocity profiles were derived directly from these box grids, assigned geographical locations equal to the mid-point between each station pair and referenced to zero velocity at the bottom. Throughout the following discussion, the sign convention is: currents out of box are positive, currents into box are negative.

ADCP data were recorded continuously from stations 5 to 95. The data processing is described in Hartman (1992), and a summary of relevant information is presented here. Calibration procedures followed those of Pollard and Read (1990), with an amplitude scaling factor of 1.005 (sd 0.01) for bottom tracking and water tracking modes, and pointing angle corrections of -0.4° (sd 0.36°, bottom tracking) and 0.02° (sd 0.48°, water tracking). Navigation data were via GPS throughout; estimates of positional accuracy were made while the ship was docked before and after the cruise, resulting in standard deviations of estimates of latitude of 24 m (before) and 11 m (after), and of longitude of 13 m (before) and 11 m (after). Consequent errors in estimates of currents from the ADCP are 4 cm s^{-1} for positional error of 24 m and 2 cm s^{-1} for 12 m, over 15 minutes. Only on-station data are used here averaged into one profile per station so that the error of the mean profile reduces according to the station duration. A 500 m cast taking about 15 minutes has ADCP errors as above. A 3000 m cast lasting 2.5 hours has errors of about 1.3 cm s^{-1} (24 m positional error) or 0.6 cm s^{-1} (12 m positional error).

Each ADCP profile comprises north and east absolute current components at 10 m depth intervals starting at 20 m depth, regridded from the output format of 8 m depth intervals starting at 13 m depth. A single profile was then created for each station pair for comparison with geostrophic calculations by averaging each component at each depth for the two stations, then computing the component of the resulting profile normal to the line between the pair. Removal of deterministic ageostrophic currents is desirable, so since the ADCP records are too short to permit removal of barotropic tides by fitting, instead the M2 component was removed by estimating its contribution to each ADCP profile from the Schwiderski model (Schwiderski, 1979; Luyten and Stommel, 1991); see figure 3.2, which shows its contribution to each station-pair profile. The complete set of de-tided ADCP profiles are shown later, in figure 6.6. In this figure, the geostrophic profiles down to 500 m are also plotted, but they are referenced to zero at σ_2=36.93, not the bottom. This is explained in context. All reference to ADCP data below means de-tided ADCP.

The offset (ADCP velocity minus geostrophic velocity) was computed for each station pair as the difference between the two current measures averaged from 100 m down in 10 m steps to a lower cutoff, which was chosen on the basis of an ADCP data quality criterion, percent good (%good). This criterion typically has a value about 100 near the surface, and its rapid drop-off at depth is indicative of the measurement range (depth) at the time, which is typically 300-400 m for on-station data. The lower cutoff was taken at 75 %good. There was a choice between using a matching range and using a single matching depth; the former was used because an average offset is obtained which provides a statistic enabling comparison of ADCP and geostrophic shears. That the shears matched well (see below) implies that offsets were generally constant with depth over the duration of each station in the ADCP depth range. The next choice was for upper cutoff depth, and 100 m was used because it appears to avoid most of the near-surface inertial motions. This is illustrated in figure 3.3 which shows currents, between 200 m and the surface, referenced to 100 m, together with the absolute current at 100 m, for about 20 hours of underway data from between stations 47 - 48. Station 47 had just been completed in light airs (wind speed < 2 m/s) when in 20 minutes the wind speed rose to an average 20 m/s. This shock set off a rather dramatic inertial oscillation whose current magnitude was about 50 cm/s, compared with a 'background' current (at 100 m) of the same magnitude. The rotation in the inertial current is plain; there is no discernible rotation at 100 m. The maximum shear on this (and a subsequent event) reached 60 - 70 m, and the near-surface mixed layer deepened from 30 m to 60 m, as evidenced by CTD profiles from before and after the event. Near-surface current anomalies seen in figure 6.6 are probably due to this type of motion. Using these cutoffs, the resulting depth ranges over which geostrophic offsets from ADCP profiles are computed are shown as horizontal bars in figure 6.6.

In order to assess the quality of this procedure, the offset error, defined here as the standard deviation about the mean difference between each pair of geostrophic and ADCP velocity profiles, was computed. These are shown in figures 3.4–3.6, together with the computed offsets. The shears match well overall; the mean and standard deviations of the offset errors are 1.2 cm/s (sd 0.7, West box), 1.1 cm/s (sd 0.6, Centre box) and 1.2 cm/s (sd 0.6, East box). Eight of the profile pairs have offset errors above 2 cm/s and only one of these (station pair 31-36, the highest offset error, 3.3 cm/s) can be ascribed to a 'junction' where the westward course pursuing the northern section was resumed after doing the first (southward) part of the western meridional section. Thus the likely most significant error in the estimation of geostrophic reference velocities by this method lies not in the quality of matching between profile pairs but in unaccounted ageostrophic baroclinic currents. This will be discussed further below.

Figures 3.7–3.9 show the offsets plotted over topography; compare their rms value with that of the M2 tides: O(10 cm s^{-1}) against O(1 or 2 cm s^{-1}). Some features may be crudely distinguished in the offsets, bearing in mind that they are noisy measures of the bottom current when the geostrophic profiles are referenced to zero at the bottom. The Denmark Strait overflow is seen at the western end of the West box with a strength of 10-15 cm s^{-1}; there is coherent westward flow around the southern end of the Rockall-Hatton Plateau; and there appears to be a northward flowing eastern boundary current at the eastern ends of the East box.

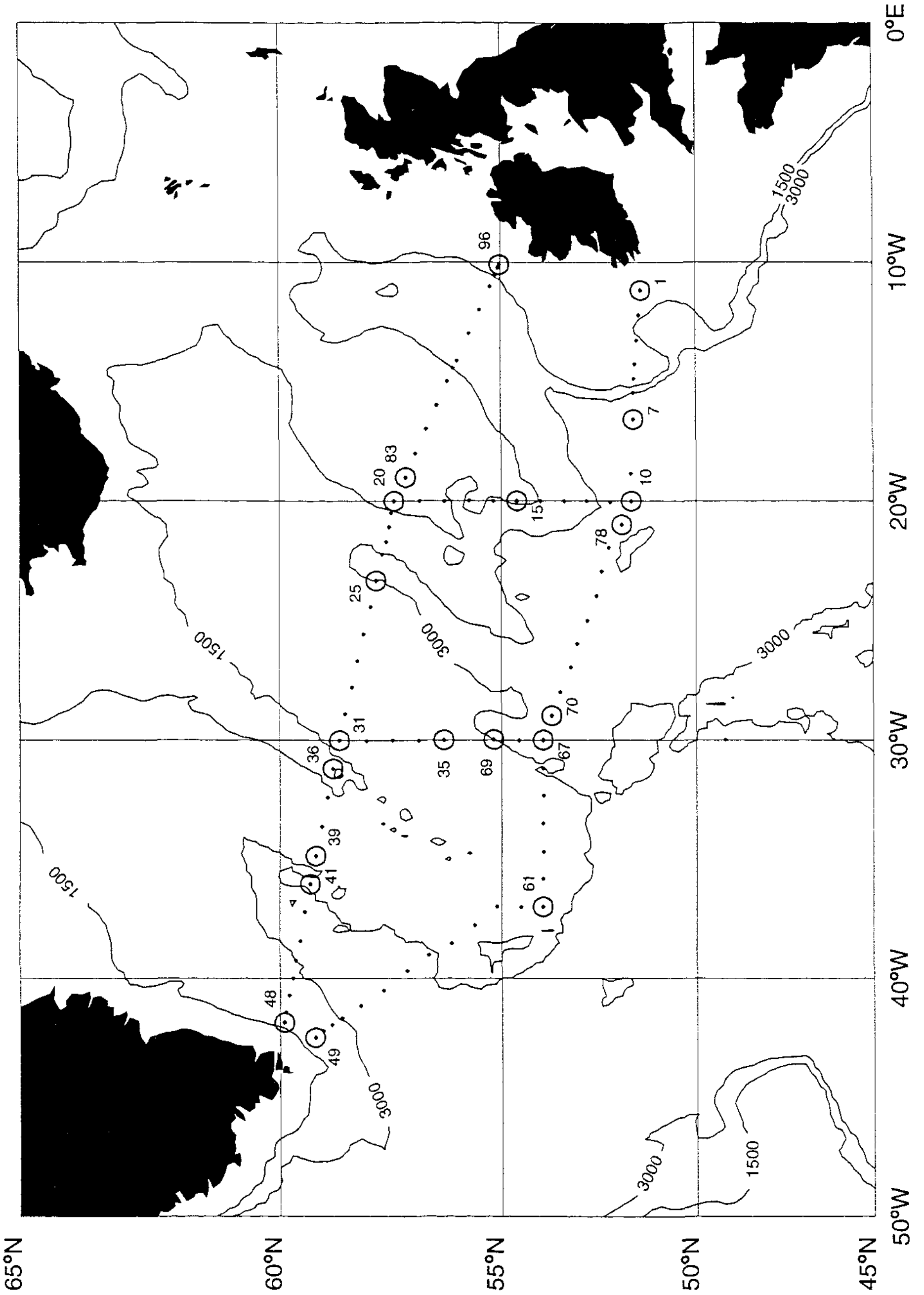

Figure 3.1: CONVEX station positions, with selected positions highlighted. Topography is illustrated with 1500 m and 3000 m depth contours. All subsequent plots using topography show the same contour levels.

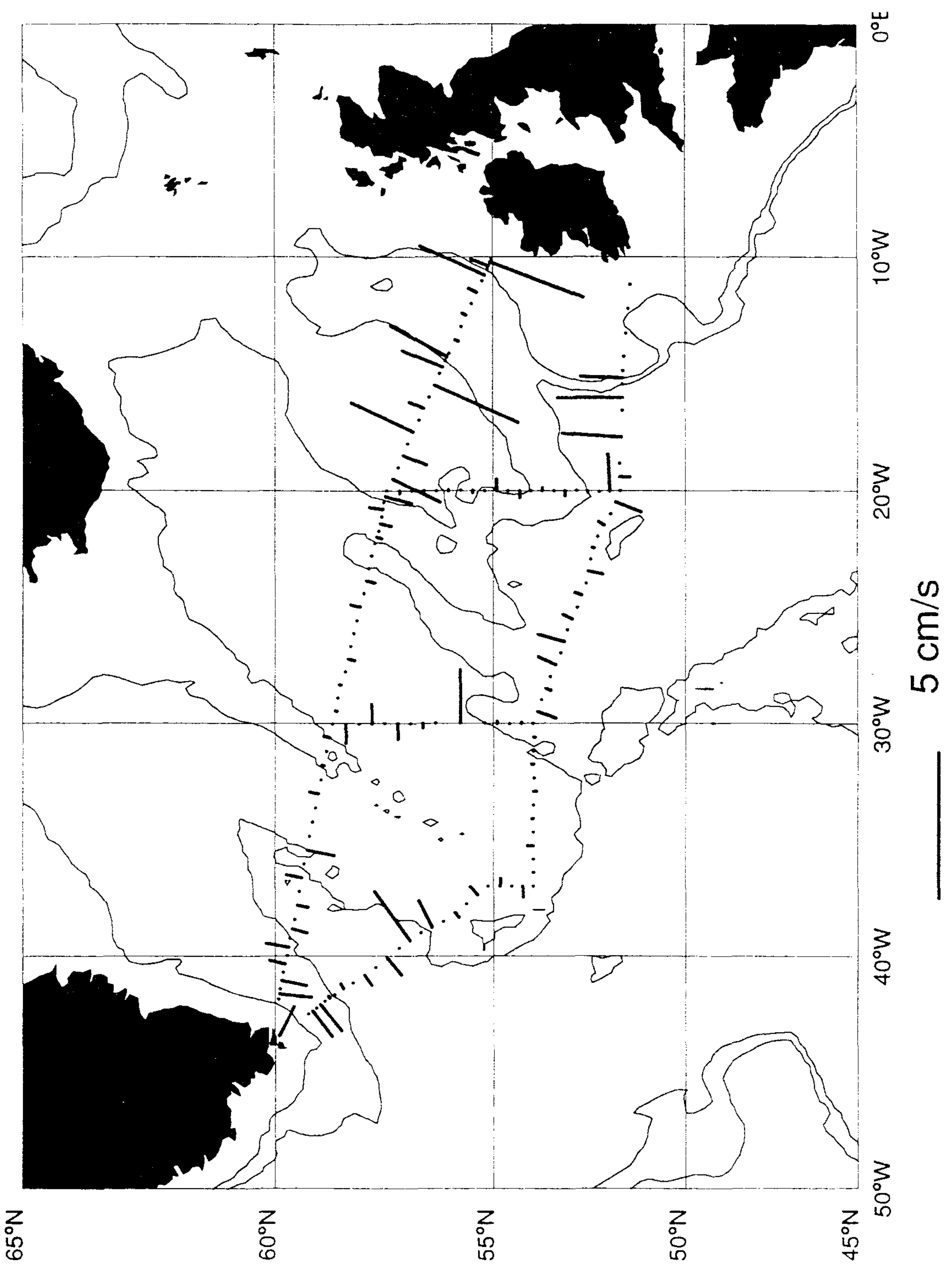

Figure 3.2: M2 tidal component of station-pair mean current.

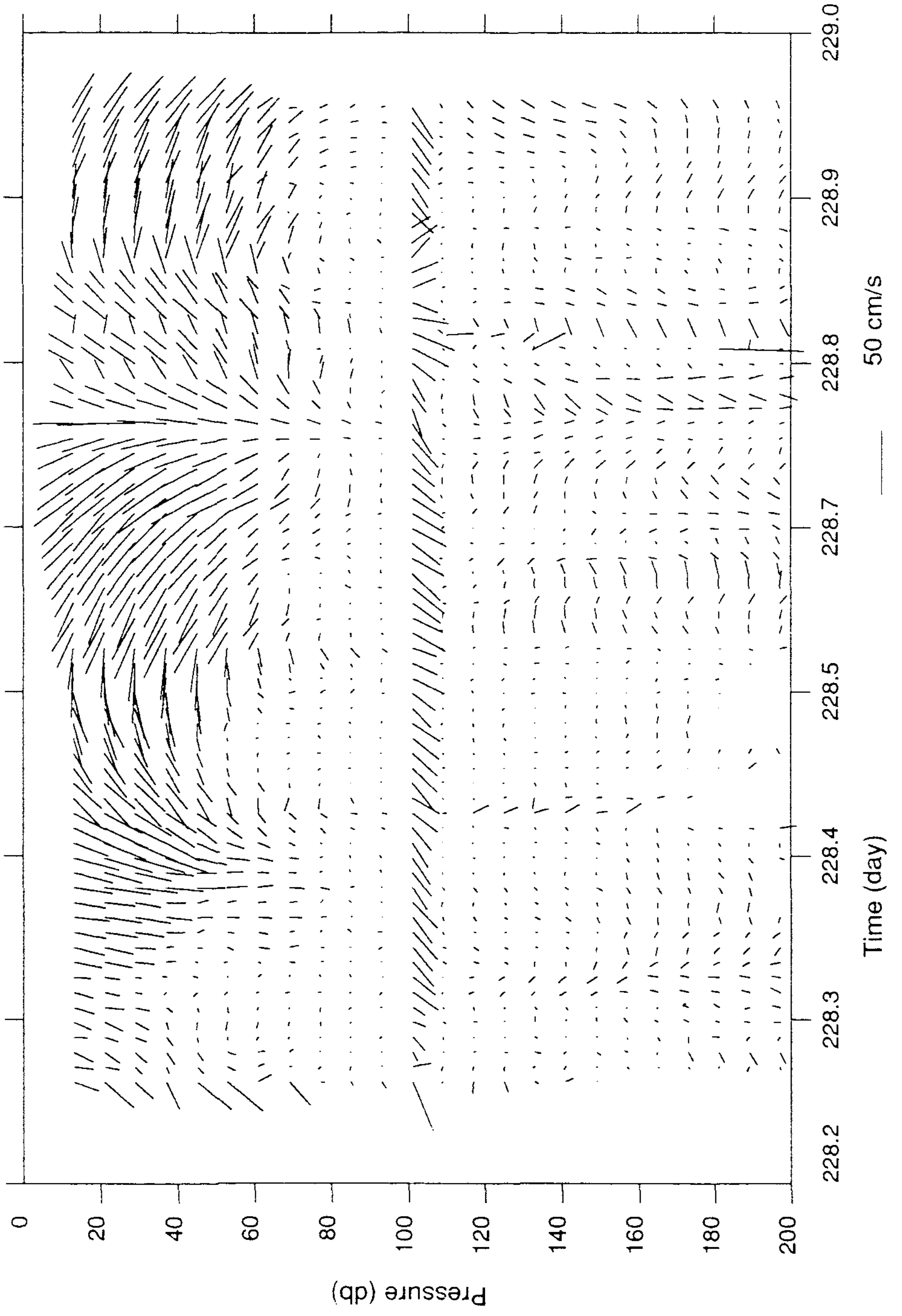

Figure 3.3: ADCP currents with geographic orientation (north - up, east - right). Current referenced to 100 m, except absolute current at shown at 100 m.

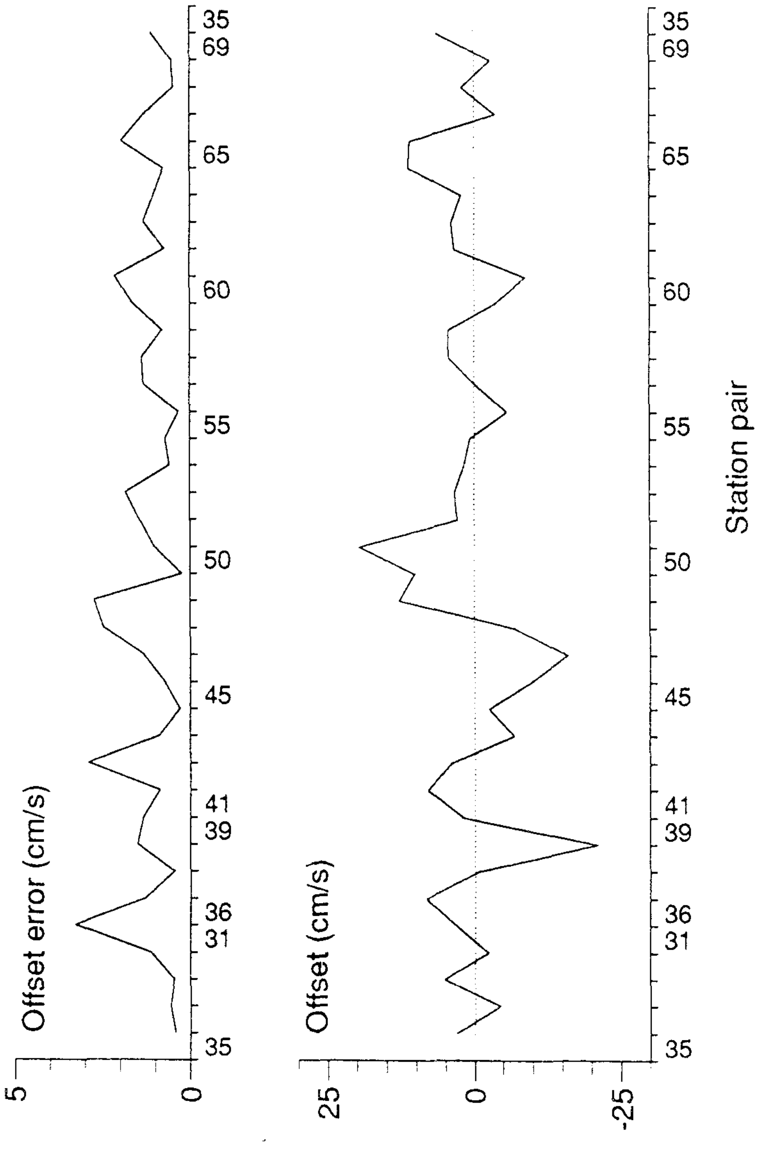

Figure 3.4: West box offset (ADCP minus geostrophic current) and offset error (standard deviation of offset about mean offset).

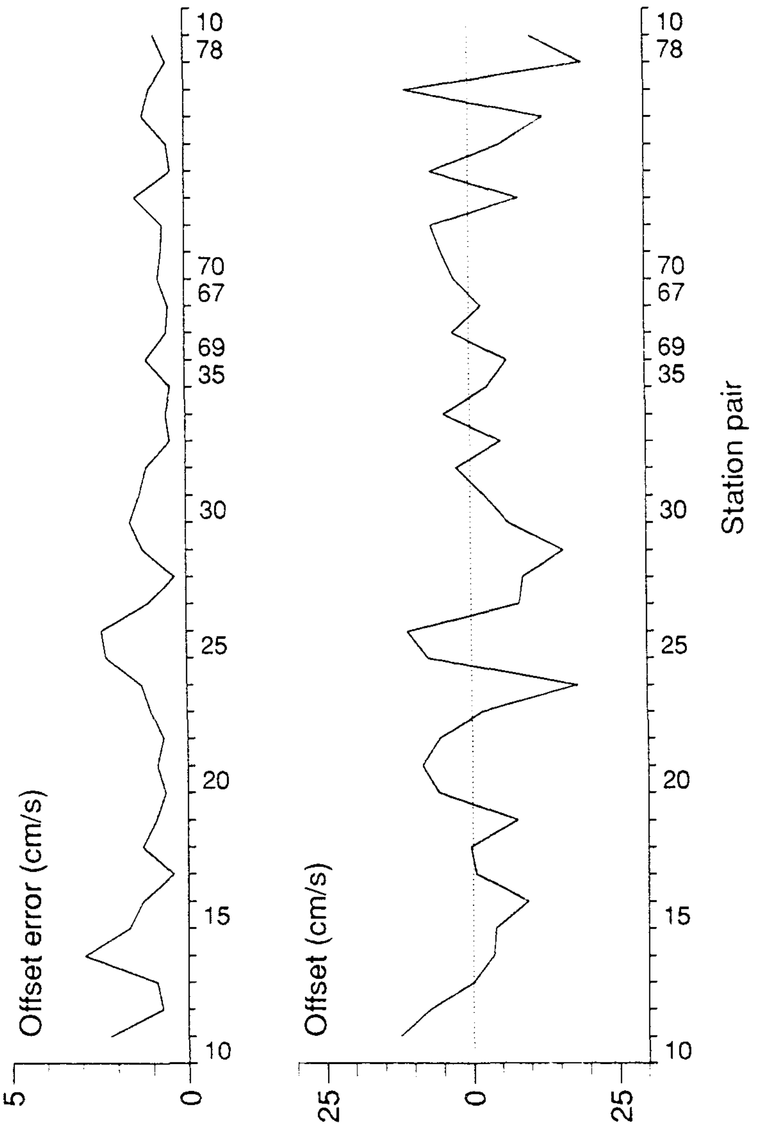

Figure 3.5: Centre box offset and offset error, as figure 3.4.

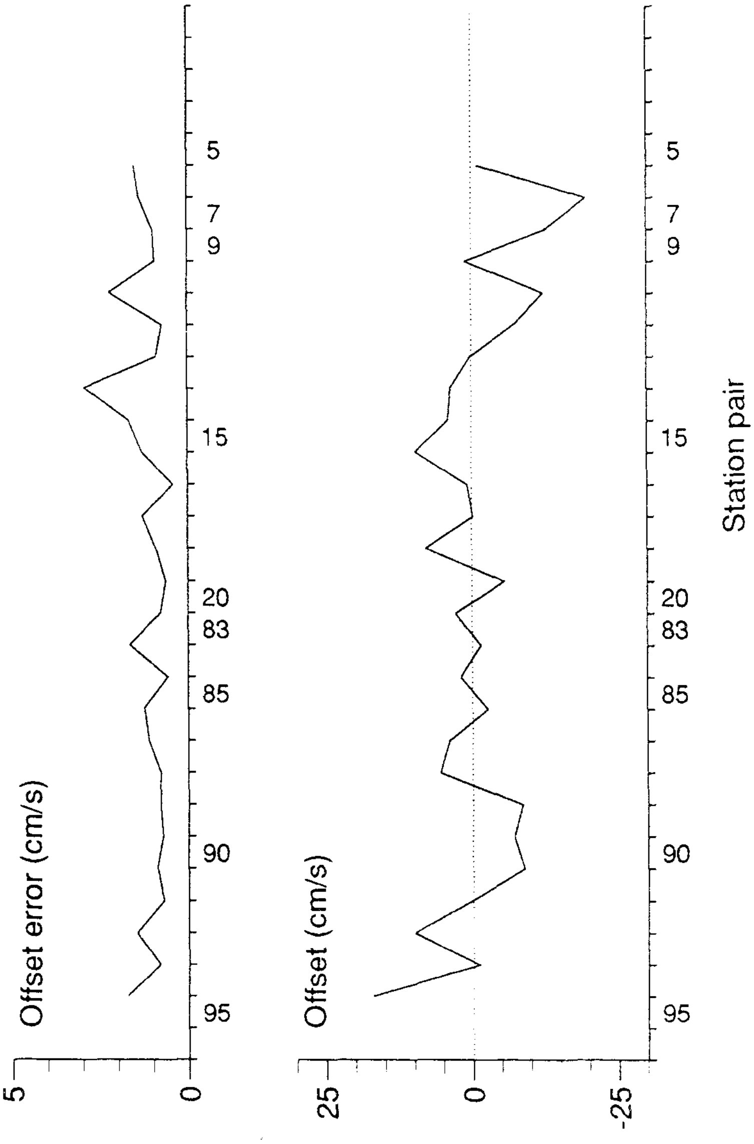

Figure 3.6: East box offset and offset error, as figure 3.4.

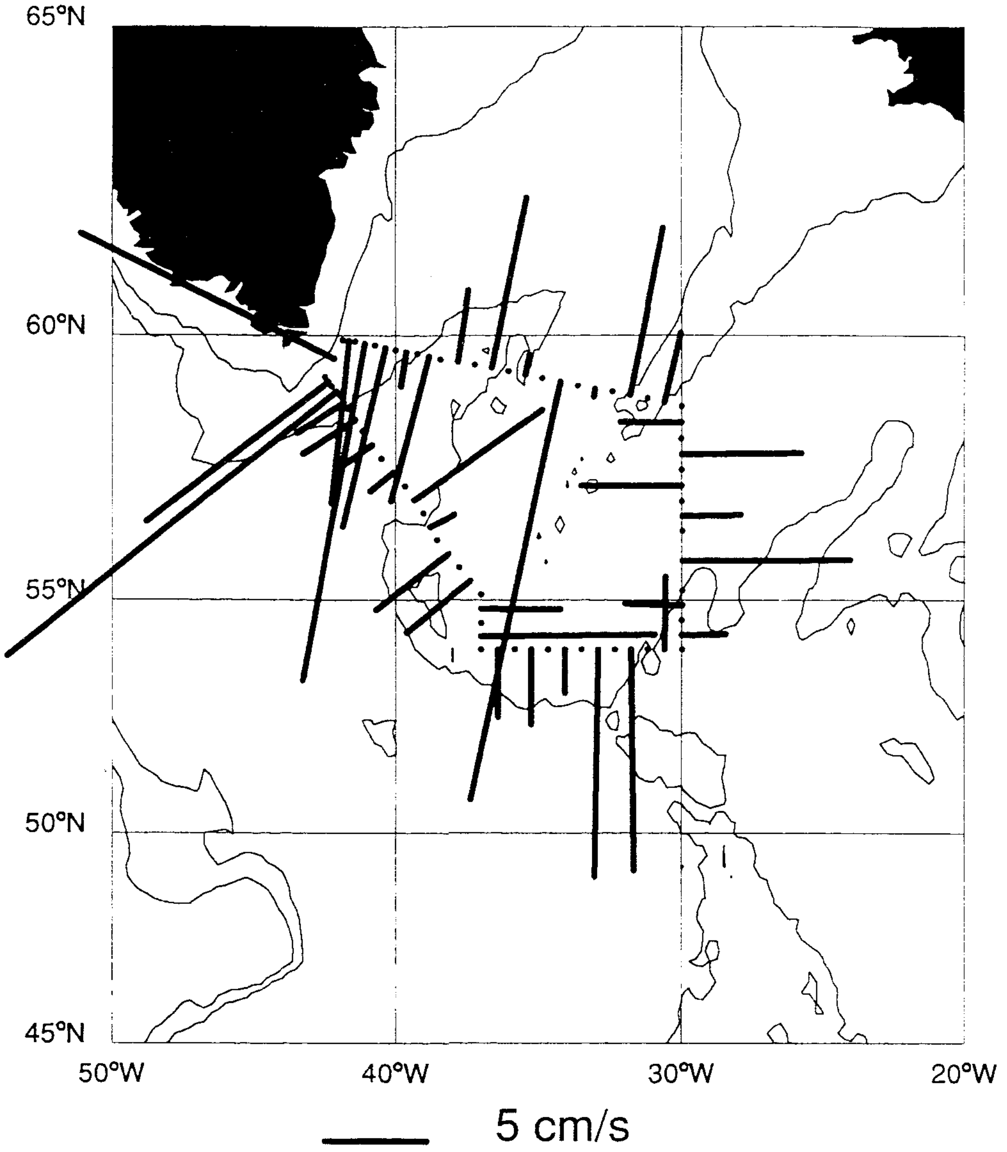

Figure 3.7: West box offsets plotted over topography.

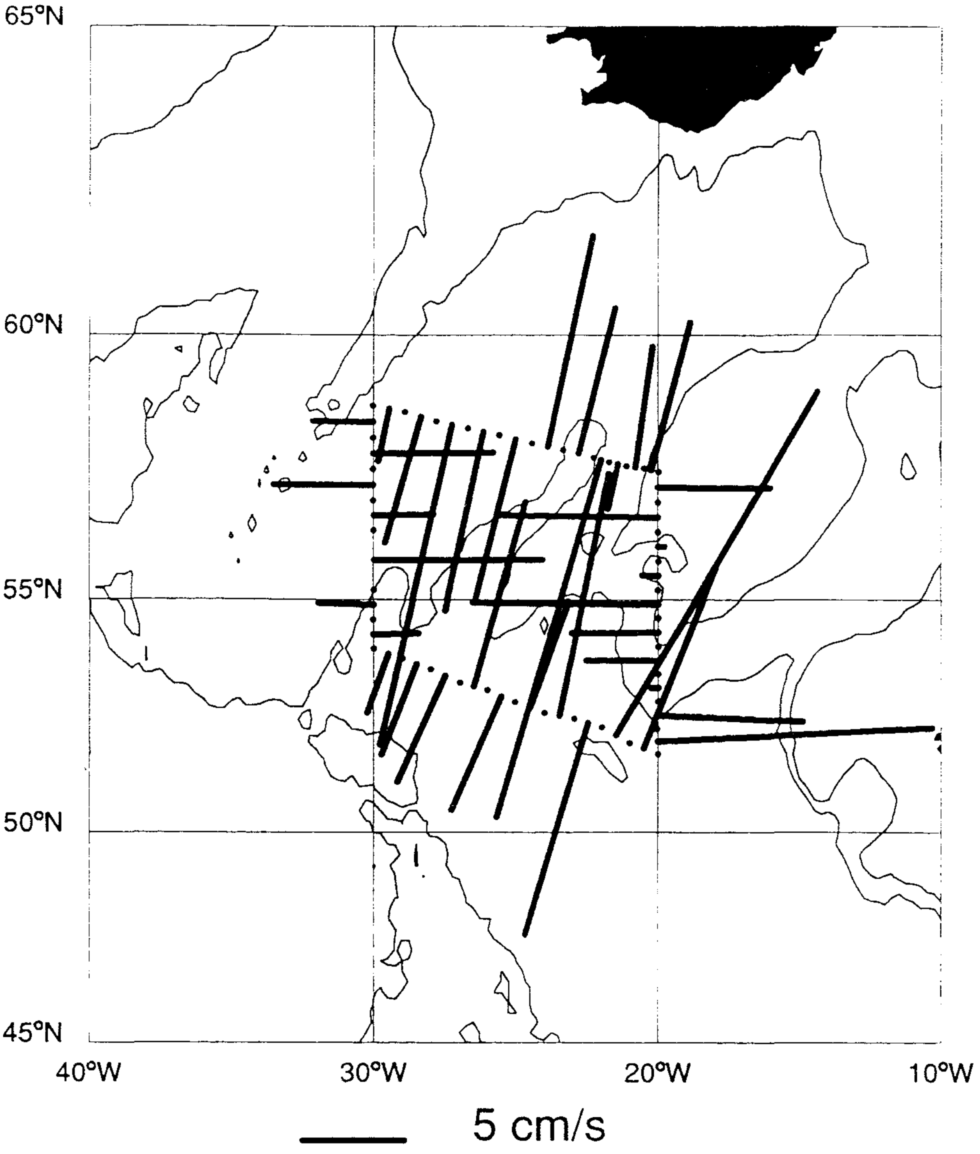

Figure 3.8: Centre box offsets plotted over topography.

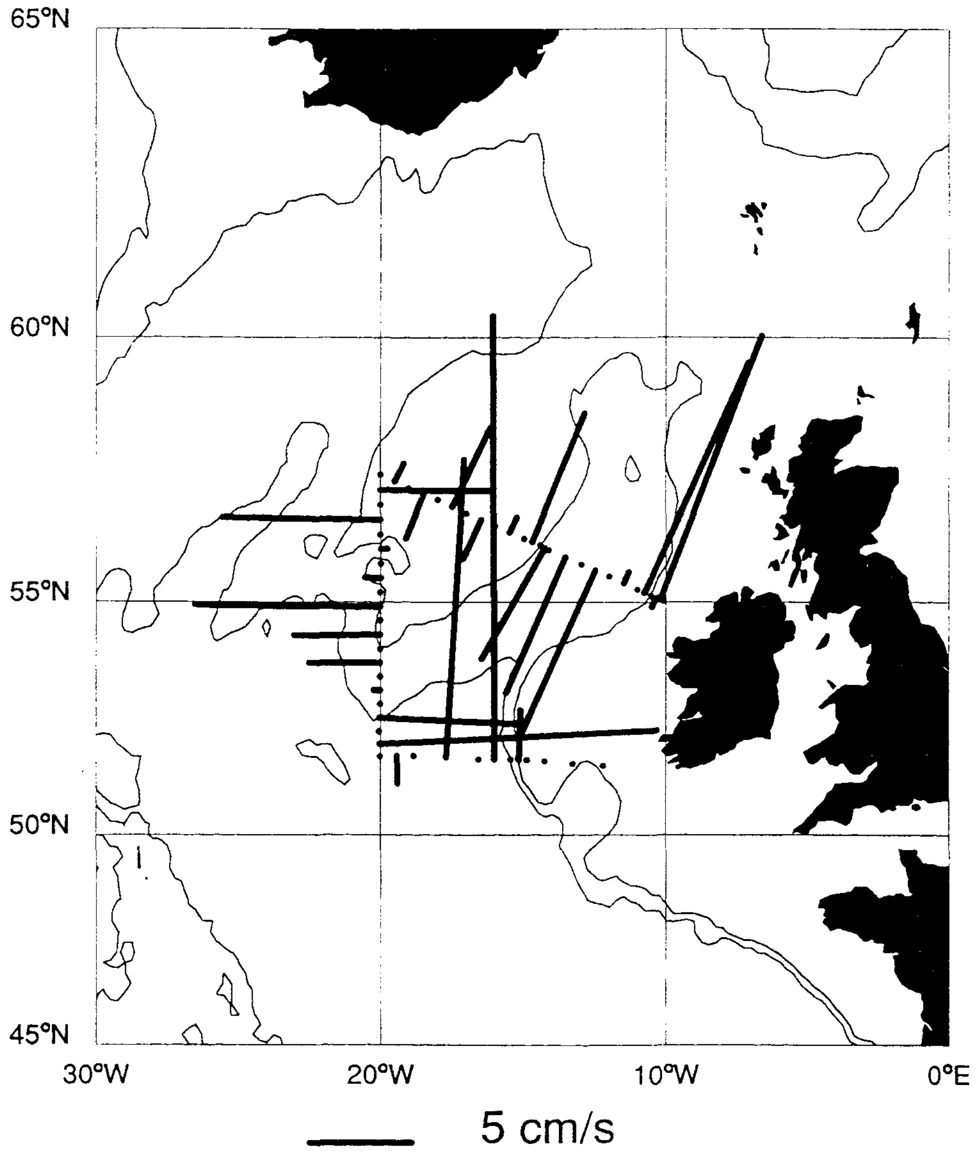

Figure 3.9: East box offsets plotted over topography.

4. SKILL IN THE INVERSION SOLUTION

4.1 Initialisation

When computing geostrophic transports, some assumptions must be made in order to allow for the 'missing triangle' at the bottom of each station pair due to the geostrophic current profile extending down only to the shallower of the two station depths; Fiadero and Veronis (1983), for example, discuss extrapolation techniques. The simplest procedure is implemented here, whereby the current at the greatest common depth is extended at a constant value to the mean pair depth from the shallower station depth using the common property and velocity values at the latter depth, and with the full station pair separation so that areas are correct. That this is simple but not simplistic is illustrated as follows. By extrapolating the deepest common shear to the bottom and using triangle geometry, the transport error due to the neglect of the shear can be estimated. This certainly over-estimates the triangle transport for each station pair, particularly where there is a large difference in station depths. Anticipating some reference currents from the inversions for comparison, gross (sum of absolute values) and net transports over the bottom triangles for each box and for reference current and shear transports are given in Table 4.1. The symmetrical arrangement of the survey pattern with respect to topography and currents means that inflow to a box is largely balanced by corresponding outflow so that net bottom triangle transports are much less than gross transports both for reference currents and shears. Now reference current transport varies between different inversion solutions and the inversion mechanism 'sees' the gross value (the solution length). Shear transport in contrast is fixed, and the net transports (less than gross) are relevant to the inversions, for which they are conservation statement errors. For the West and Centre boxes these net transports are about 0.6 Sv (1 Sv = 10^6 $m^3 s^{-1}$), which translates into 0.1 mm s^{-1} reference currents over the whole of the relevant boxes. This is believed negligible. There is one instance of inadequate topographic resolution by the survey in the East box, where the apparently enormous shear transport results mainly from one station pair on the west side of the Porcupine

Bank where the difference in bottom depths is over 2400 m and the extrapolated bottom current ridiculous; the result of removing this station pair from the sum is given by the values in parentheses in Table 4.1. This is similar to the example in Fiadero and Veronis (1983), who recommend the projection of the deepest common velocity in such cases.

It is worth noting that as the present implementation uses zero velocity at the bottom as the geostrophic reference, the solution vector is then the vector of bottom velocities.

The selection of layer divisions was based on water mass analysis (J. F. Read, pers. comm., 1992) such that $\sigma_2>36.95$ is identified as overflow water, $36.95>\sigma_2>36.8$ as Labrador Sea Water, $\sigma_2<36.8$ and $\sigma_0>27.7$ as North Atlantic Central Water, and surface waters $\sigma_0<27.7$. The two strategies (few thick layers, many thin layers) discussed above are applied separately to each box (West, Centre, East) based on the above considerations, so that in each box the few-layer strategy is realised in the same way: surface, $\sigma_2=36.8$, $\sigma_2=36.95$ and bottom. These levels give three layers so that the requirements of volume and salt transport conservation in each gives six constraints in all. The many-layer strategy is realised by a quasi-arbitrary subdivision of the water column set out for each box in Table 4.2; the density surfaces are plotted for each box in Figures 4.1–4.3. Volume transport conservation and salt transport conservation were required in all layers, and heat conservation was required in all layers but the surface; a total of 23 (East), 23 (Centre) and 29 (West) constraints resulted.

4.2 Correlation

In what way are the inverse solutions to be correlated with the ADCP data? The ADCP offsets are used as a measured representation of the geostrophic reference currents and are denoted by $\mathbf{m}^{\mathrm{adcp}}$. Now the inverse solution $\mathbf{m}^{\mathrm{est}}$, by virtue of being produced from an underdetermined system, is a partial solution; the cutoff value of q in (2.31) is less than the number of unknowns N, so correlating $\mathbf{m}^{\mathrm{adcp}}$ with $\mathbf{m}^{\mathrm{est}}$ is not to compare 'like with like'. Now the SVD process enables the creation of a filter (the model resolution matrix **R**) whereby the 'real world' solution $\mathbf{m}^{\mathrm{true}}$ can be projected on to the available elements of the basis vector set **v**. One then assumes that $\mathbf{m}^{\mathrm{adcp}}$ may be used as an estimate of $\mathbf{m}^{\mathrm{true}}$. With basis vectors up to degree q, and including weighting explicitly, we have:

$$\begin{aligned}\mathbf{m}^{\mathrm{filt}} &= \mathbf{W}^{-1/2}\mathbf{R}\mathbf{W}^{1/2}\mathbf{m}^{\mathrm{adcp}} \\ &= \mathbf{W}^{-1/2}\mathbf{V}\mathbf{V}^{\mathrm{T}}\mathbf{W}^{1/2}\mathbf{m}^{\mathrm{adcp}} \\ &= \mathbf{W}^{-1/2}\sum_{i=1}^{q}\mathbf{v}_i\mathbf{v}_i^{\mathrm{T}}\mathbf{W}^{1/2}\mathbf{m}^{\mathrm{adcp}} \\ &= \mathbf{W}^{-1/2}\sum_{i=1}^{q}\beta_i\mathbf{v}_i\end{aligned} \tag{4.1}$$

where $\beta_i = \mathbf{v}_i^{\mathrm{T}}\mathbf{W}^{1/2}\mathbf{m}^{\mathrm{adcp}}$

and $\mathbf{m}^{\mathrm{filt}}$ is the ADCP solution filtered to degree q (ie, projected onto eigenvectors from degrees 1 to q).

The product-moment correlation coefficient r^2 is used to compare pairs of vectors; in (4.2) below we correlate $\mathbf{m}^{\mathrm{adcp}}$ with $\mathbf{m}^{\mathrm{est}}$:

$$r^2 = \frac{\left(\mathbf{m}^{\mathrm{est}} - \overline{\mathbf{m}^{\mathrm{est}}}\right)^{\mathrm{T}}\left(\mathbf{m}^{\mathrm{adcp}} - \overline{\mathbf{m}^{\mathrm{adcp}}}\right)}{\left\|\mathbf{m}^{\mathrm{est}} - \overline{\mathbf{m}^{\mathrm{est}}}\right\| . \left\|\mathbf{m}^{\mathrm{adcp}} - \overline{\mathbf{m}^{\mathrm{adcp}}}\right\|} \tag{4.2}$$

where $\overline{\mathbf{m}^{\mathrm{est}}}$ is the vector all of whose elements are equal to the mean of the elements of $\mathbf{m}^{\mathrm{est}}$, etc; ie,

$$\left\{\overline{m_i^{\mathrm{est}}}\right\} = \frac{\sum_{j=1}^{N} m_j^{\mathrm{est}}}{N} \tag{4.3}$$

Note that for q=1, $|r^2|=1$, since $\mathbf{m}^{est} = \overline{\mathbf{m}^{est}}$, etc.

As another means of comparison, we also generate a statistic which we refer to below as 'sd(diff)', which is the standard deviation of the difference between each vector pair about the mean difference, and is calculated thus:

$$\mathrm{sd(diff)} = \left\{ \frac{1}{N} \cdot \sum_{i=1}^{N} \left(\left[m_i^{est} - m_i^{adcp} \right] - \frac{1}{N} \sum_{j=1}^{N} \left[m_j^{est} - m_j^{adcp} \right] \right)^2 \right\}^{1/2} \qquad (4.4)$$

4.3 Results

The inversions were performed in accordance with the conditions set out above. The presentation of the results is described in this section, and is discussed in the next section.

Tables 4.3–4.6 give the results of correlating $\mathbf{m}^{adcp}$ with $\mathbf{m}^{est}$, $\mathbf{m}^{est}$ with $\mathbf{m}^{filt}$ and $\mathbf{m}^{filt}$ with $\mathbf{m}^{adcp}$, for each strategy, for each box and for each solution degree, together with the standard deviation of the difference between each vector pair about the mean difference; this statistic is referred to as sd(diff). The mean differences, which are not shown, are very small (<1 mm/s). The correlations are between equal valued inverse solution degree (for $\mathbf{m}^{est}$) and filter degree (for $\mathbf{m}^{filt}$).

Each of figures 4.4–4.9 show solution vectors ($\mathbf{m}^{est}$; lower panel) and ADCP projections ($\mathbf{m}^{filt}$; upper panel). Each panel shows the relevant vectors plotted as a 'net' in three dimensions, so that the x-axis (left-right) shows vector element (ie, station pair); the y-axis (in-out) shows solution or filter degree; and the z-axis (up-down) shows vector element magnitude; these nets are drawn without perspective. Figures 4.4–4.6 show, for each box for the few-layer strategy, the complete sequence of solution and filter vectors (all degrees). Figures 4.7–4.9 show, for each box for the many-layer strategy, reduced sequences of solution and filter vectors, for clarity. Noise in the higher solution degrees (not shown) make the plots very unclear. Figure 4.10 shows all eigenvalues for all solutions.

4.4 Correlations: discussion

The first point to note about the computed correlations is that highly significant positive correlations are obtained between the inversion solution estimates $\mathbf{m}^{est}$ and both independent ADCP-derived solution estimates $\mathbf{m}^{adcp}$ and $\mathbf{m}^{filt}$, for all three boxes using the many-layer strategy (Tables 4.4–4.6), but more irregularly over the boxes for the few-layer strategy (Table 4.3). For the few-layer strategy (Table 4.3), we see in the West box a correlation maximum of $r^2=0.64$ for degree 6 between $\mathbf{m}^{est}$ and $\mathbf{m}^{filt}$, but there is only one positive $\mathbf{m}^{est}$-$\mathbf{m}^{filt}$ correlation for the East box, and weak indications of $\mathbf{m}^{adcp}$-$\mathbf{m}^{est}$ correlation. The consistency of the many-layer results compared with the few-layer ones is not a reason to discard the latter, but is suggestive of greater 'information-extraction' ability in the former, so the remainder of the discussion will be confined to the many-layer results, although few-layer solutions might be more useful if more information could be extracted from each layer, such as by the inclusion of constraints using more and different tracers from those employed here. This presents different problems which are not within the scope of the present discussion, such as how to employ potential vorticity, which is not conservative in western boundary currents (dissipative / frictional regimes), or how to employ oxygen, which is injected at the sea surface and is (to a small extent) consumed in the water column.

The $\mathbf{m}^{filt}$-$\mathbf{m}^{adcp}$ statistics are included in order to demonstrate that, for all boxes, as the number of filter degrees approaches the number of station pairs, r^2 increases and the standard deviation of the difference between the vectors decreases, as would be expected.

For the West box, there is no correlation between either $\mathbf{m}^{est}$-$\mathbf{m}^{filt}$ or $\mathbf{m}^{adcp}$-$\mathbf{m}^{est}$ for the first and last few solution and filter degrees; there are good positive correlations between degrees 7 and 21. The $\mathbf{m}^{est}$-$\mathbf{m}^{filt}$ and $\mathbf{m}^{adcp}$-$\mathbf{m}^{est}$ correlation maxima occur at the same degree (10); the former is nearly double ($r^2=0.60$) the latter ($r^2=0.34$). The variation of r^2 with degree is quite smooth; there is a secondary correlation maximum for $\mathbf{m}^{est}$-$\mathbf{m}^{filt}$ at degree 19 ($r^2=0.20$) which is not present in the correlation of $\mathbf{m}^{adcp}$-$\mathbf{m}^{est}$.

For the Centre box, the correlation structure is different from the West box; for $\mathbf{m}^{adcp}$-$\mathbf{m}^{est}$, there is a weak maximum about degrees 9-10 ($r^2 \sim 0.2$), and not much else. However, $\mathbf{m}^{est}$-$\mathbf{m}^{filt}$ correlations are all very strong up to degrees 11-12, with a maximum of $r^2=0.86$ at degree 4, and $r^2>0.5$ for degrees 7-10. The variation of correlation with degree is again quite smooth.

The East box is different again, with r^2 for $\mathbf{m}^{adcp}$-$\mathbf{m}^{est}$ negative or about zero for most solution degrees; the maximum correlation of $r^2=0.28$ occurs at degree 10. The correlation of $\mathbf{m}^{est}$-$\mathbf{m}^{filt}$ starts large and negative and turns positive after degree 8; maximum r^2 (0.34) is at degree 19; the intermediate maximum about degrees 9-10 has values of r^2 slightly less than those for $\mathbf{m}^{adcp}$-$\mathbf{m}^{est}$.

4.5 Hydrography: discussion

All solution vectors developed here represent bottom currents. Do the solutions reproduce features of the deep flow which might be expected on the basis of previous studies? Using the schematic of deep circulation in Dickson *et al.* (1990), one looks for the overflows from the Iceland-Scotland ridge flowing south down the eastern flank of the Mid-Atlantic Ridge, then north up its western flank, then in some way joining the Denmark Strait overflow, which runs south down the west side of the Irminger Basin. Two examples of West box solutions, degrees 10 and 19, are selected as examples based on correlations as above, and are inspected for such features; see figures 4.11–4.12. It can firstly be seen that the Denmark Strait overflow is put in place by the inversion mechanism, and secondly that flows in the appropriate senses can be seen on each flank of the Mid-Atlantic Ridge. The eastern ridge flows are reproduced as stronger (3-5 cm s^{-1}) and more coherent than the western flows (<2 cm s^{-1}) and are similar in both solution examples, which is reasonable given the effect of the Charlie-Gibbs Fracture Zone (Saunders, 1994) on the deep current through-flows. The major difference between the examples is the difference in strength of the Denmark Strait overflow. In the solution of degree 10, the current is 5-7 cm s^{-1}; in that of degree 19, it is a more sensible 12-18 cm s^{-1}.

Referring to the West box many-layer solution and filter nets of figure 4.7, the development of the Denmark Strait overflow in the solution and of its analogue in the filtered ADCP can be seen on the north side of the box as negative (into box) currents between stations 42-46; and positive (out of box) currents between stations 50 and 54/5. The southgoing flows over the east side of the Mid-Atlantic Ridge appear similarly between stations 31-35 and 61-64. The 'cosmetic' effect of the increase of solution structure on the appearance of geostrophic velocity sections referenced to the solution vectors is seen in the sections of figures 4.11–4.12.

The Centre box solution of degree 10 (see figure 4.13) appears to have as its only 'success' the flow around the south-west end of the Rockall-Hatton Plateau; most of the remainder of the solution is weak and, for the west side of the box, in the opposite direction to the flow determined in the West box. However, solution degree 13 does put a flow of 2-3 cm s^{-1} down the east side of the Mid-Atlantic Ridge, between stations 67 and 35. The influence of the large eddy-like feature beween stations 76-78 appears not to penetrate to the bottom. The filter net of figure 4.7 is much noisier than (has much larger amplitude vectors than) the solution net.

The East box provides an apparently successful representation of the sense of the deep flow, but the solution degree chosen for illustration is uncorrelated with the relevant $\mathbf{m}^{\text{filt}}$ (degree 8). There is a north-going current of a few (2-3) cm s^{-1} at the shelf edge in both north and south sides; there is flow of consistent sense (anti-cyclonic) around the Rockall-Hatton Plateau, with south-trending flow on the east side of the Plateau, west-trending flow at its south end, and some east (actually north-east?) trending flow at the north end of the west side of the box. Solution degree 8 is the first of the East box many-layer solution vectors which imposes distinct structure (see figure 4.14).

4.6 Implications

Let's try to proceed by unpacking the offset. Here's one way to do so:

$$\mathbf{m}^{\mathrm{adcp}} = \mathbf{m}^{\mathrm{est}} + \mathbf{m}^{\mathrm{null}} + \mathbf{n}^{\mathrm{inst}} + \mathbf{n}^{\mathrm{ag}} \qquad (4.4)$$

which says that the offset is the sum of four elements:

(i) the inversion solution ($\mathbf{m}^{\mathrm{est}}$), which is the (presumed correct) geostrophic reference current vector, but as derived from the information-poor hydrographic constraints, etc;

(ii) the rest of the geostrophic reference current vector ($\mathbf{m}^{\mathrm{null}}$), ie, the extra components of the solution which would be obtained were the inversion fully determined and the ocean stationary in geostrophic balance (more generally, if the inverse model dynamics were the true ocean dynamics) so $\mathbf{m}^{\mathrm{est}} + \mathbf{m}^{\mathrm{null}} = \mathbf{m}^{\mathrm{true}}$;

(iii) instrumental and measurement noise, $\mathbf{n}^{\mathrm{inst}}$, which contains the effect of navigation errors and also the error due to taking mean on-station ADCP profiles to estimate the offset rather than the mean cross-track ADCP velocity between the stations (underway data), which is appropriate by reason of the integrating nature of geostrophy; and

(iv) ageostrophic noise, $\mathbf{n}^{\mathrm{ag}}$, or everything else. This last component requires further expansion. In the present case, M2 tides have been (mainly) removed, so all remaining barotropic tides are left. All departures from the model dynamics of the general circulation are left, so here that means time-variation, diffusion, vertical motions etc; and finally, $\mathbf{n}^{\mathrm{ag}}$ contains transient ageostrophic currents.

What then can be said about each of these elements? Results from the West box will be used as examples: as the most synoptic box, one expects a quasi-stationary geostrophic balance to be most nearly applicable, so that departures from dynamics in $\mathbf{n}^{\mathrm{ag}}$ are deemed small, as are residual barotropic tides (say <0.3 cm s^{-1}, since the rms length of the M2 tides in the West box is 0.7 cm s^{-1}). Then $\mathbf{n}^{\mathrm{inst}}$ + all of $\mathbf{n}^{\mathrm{ag}}$ except transients may be 1 - 2 cm s^{-1}. The rms offset length is 7.8 cm s^{-1}; using subscript to indicate solution degree, the rms length of $\mathbf{m}_{10}^{\mathrm{est}}$ is 2.4 cm s^{-1}, that of $\mathbf{m}_{19}^{\mathrm{est}}$ is

5.0 cm s^{-1}. Now *guess* that $\mathbf{m}_{19}^{\text{est}}$ is correct; based on the hydrographic evidence, it is at least not far off. Accepting that guess, we can then say that $\mathbf{m}_{19}^{\text{null}} = 0$ (meaning the contribution from eigenvectors 20 onwards), we are left with an estimate of the rms transient ageostrophic element of $\mathbf{n}^{\text{ag}}$ of 1.8 - 2.8 cm s^{-1} (2 - 3 cm s^{-1}, rounded), which is speculative but plausible. Saunders' (1994) estimate of transient ageostrophic noise in mid-latitudes in the South Atlantic, for example, is of up to 5 cm s^{-1}. We also get $\mathbf{m}_{10}^{\text{null}} = 2.6$ cm s^{-1}, attributable to the apparent under-estimate at degree 10 of the strength of the Denmark Strait Overflow.

Pursuing the same argument for the East box is more problematic because one is less willing to assert the synopticity of the stations. However, $\mathbf{m}_{8}^{\text{est}}$ *looks* plausible, and Saunders (1982) suggests that flows (using a section at 48°N) are weak and <1 cm s^{-1} throughout the water column. The rms length of $\mathbf{m}_{8}^{\text{est}}$ here is 1.1 cm s^{-1}, so if the weaker flow allows the extension of synopticity to this box also, and setting other lengths as for the West box ($\mathbf{m}_{8}^{\text{null}} = 0$, other noise = 1 - 2 cm s^{-1}), then with the rms offset length also 7.8 cm s^{-1}, we are left with an rms ageostrophic transient length of 4.8 - 5.8 cm s^{-1} (5 - 6 cm s^{-1}).

If the magnitudes (but not all the directions) of $\mathbf{m}_{10}^{\text{est}}$ for the Centre box are taken as about right at 1.3 cm s^{-1}, then with an rms offset length 8.2 cm s^{-1}, we find an rms ageostrophic transient length of 4.9 - 5.9 cm s^{-1}, similar to the East box values but even harder to justify.

Why does the correlation technique work at low to intermediate solution degrees in some cases, and why does it work at all, given the apparent domination of $\mathbf{m}^{\text{adcp}}$ by noise? The spatial variance spectrum of the ocean is red (eg. Le Traon *et al.*, 1990). SVD is an axis-rotation process in which the eigenvectors are the axes and the axial directions which are sought are those of maximum variance. So SVD of eddy-resolving large-scale ocean sections will put long-wavelength, high-variance information into low degrees, and short-wavelength, low-variance information into high degrees. Thus there will be an approximate correspondance between solution degree and and solution spatial scale around the box: high solution degrees correspond to high wavenumber (short wavelength) solution vectors, and vice-versa. See figures 4.11 and 4.12 (both west box with many-layer solutions, as already mentioned in section 4.5), where there is an increase in the number of current reversals in going from solution degree 10 in the former to degree 19 in the latter, illustrating the effect of increasing wavenumber with increasing solution degree.

If the coherent length scale for ageostrophic currents, suggested as the main source of ADCP noise here, is short (Pollard, 1970, suggests tens of kilometres for inertial oscillations), then the noise should be preferentially filtered out at lower degrees compared with higher degrees. A white noise spectrum has energy at all wavelengths, so $\mathbf{m}^{\mathrm{filt}}$ will remain partially noise-contaminated at low degrees, and mainly so at higher degrees; however, the partial variance separability between geostrophic circulation and ageostrophic noise allows the comparison technique a measure of success.

This work impinges on the use of ADCP measurements as constraints in inversions. Now if the inversion produces correct results and if an ADCP-derived solution estimate contains parallel information up to a degree, and the (hydrographically-constrained) inversion solution has skill beyond the degree where ADCP noise sets in, then the orthogonal information in the ADCP data is not 'good' information but noise. This may explain the 'two-state' solution of BT. However, the presence of good information in ADCP data may make that data useful in most severely underdetermined problems: for example, a section across an ocean basin where one might be reasonably confident of imposing one hydrographic constraint only - that of total volume flux conservation, say - might be usefully additionally constrained by ADCP data.

4.7 Summary

A new technique enabling objective comparison between box-type inversion results and an independent solution measure has been presented and shown to work. It gives a confirmation, by comparison with independent measurements, that there is skill in the inversions presented here. In so doing, a question has been asked implicitly: does the inversion work? Of course it does, algebraically, so this question is translated more specifically as: (i) are the constraints appropriate? (ii) is the model correct or realistic? and (iii) how serious is the absence of $\mathbf{m}^{\mathrm{null}}$? In reverse order, some shaky responses to (iii) are given in 6c above. In answer to (ii), simple geostrophy is fairly good in much of the world ocean, and the results of its use here appear adequate. Question (i) separates into questions about hydrographic constraints on the one hand (where conservation statements are generally reliable), and statistical constraints on the other. The underdetermined problem must be closed; of the two constraints applied to this end, minimum square error and minimum square solution length, I suggest that the latter is physically the weaker, and the results presented here are encouraging in that they suggest that it performs well.

This confirmation of skill is crucially dependent on the availability of good ADCP data, and future improvements in ADCP data should improve the technique. Navigational advances such as 3D differential GPS, which enables measurement of ship heading with greater accuracy than by gyro compass, (see King and Cooper, 1993) and differential GPS (which increases ship position measurement accuracy) may permit the generation of cross-track currents from ADCP underway data. Devices which measure currents to greater depth (lowered ADCP, acoustic correlation current profiler) may enable matching to extend further down the water column away from surface effects.

It is more difficult to provide an answer to the question of how the correlation technique helps one to select the best solution. The correlation structure can provide a guide to the selection of solution degree (q), but only if the analyst believes the results of the inversion. For example, in the case of the centre box inversions above, one finds the bottom currents over the Reykjanes Ridge on the west side of the box flowing in the opposite direction to that believed to obtain: while knowing the water's source to lie to the north, the solution still places a northwards velocity there. If one does believe the results qualitatively, such as in the case here of the west box, where bottom flow *directions* largely conform with prejudice, one then proceeds to select the solution degree to determine the solution *magnitude*. If one employs prior knowledge in addition to the correlation structure, one might enquire whether that knowledge might not be usefully incorporated in the inversion in the form of one or more extra constraints?

In this section, the solution is providing valuable reference velocity information. It is able to do this because we choose a highly divergent first guess (zero velocity at the bottom), therefore **d** is large and the mechanism has 'something to work on'. As solution degree increases, the flow field becomes less divergent (in accordance with the constraints which are being applied by the inversion) but at the cost of becoming increasingly noisy. This is the the trade-off noted at the beginning of the use of method – see W78, for example. However, we have deliberately chosen an unreasonable reference level for the purpose of making the inversion work hard. Later, in section 6, we see the consequences of a 'responsible' choice of reference level – so as to produce as nearly non-divergent a first guess as possible – where the solutions are small.

Table 4.1: Bottom triangle transport errors (Sv) due to extrapolated geostrophic shear. "Shear" stands for extrapolated shear transport, "Ref" stands for reference current transport; reference currents are obtained from inversion solution degree 10 (West), 10 (Centre) and 8 (East), all many-layer inversions. Values in parentheses have transport due to one station pair in the Porcupine Sea bight removed.

	West box	Centre box	East box
Ref., gross	9.4	3.7	3.9
Ref., net	-0.7	0.8	-0.1
Shear, gross	1.4	2.5	25.9 [4.7]
Shear, net	-0.6	-0.7	19.8 [-1.4]

Table 4.2: Density surfaces employed for 'many-layer' inversions for each box.

Number	Variable	West box	Centre box	East box
0	σ_0	surface	surface	surface
1	σ_0	27.30	27.20	27.20
2	σ_0	27.50	27.40	27.40
3	σ_0	27.60	27.60	27.60
4	σ_2	36.80	36.80	36.80
5	σ_2	36.86	36.87	36.87
6	σ_2	36.90	36.93	36.93
7	σ_2	36.94	37.00	37.00
8	σ_2	37.00	bottom	bottom
9	σ_2	37.08		
10	σ_2	bottom		

Table 4.3: Correlation and difference statistics for few-layer inversion solutions for each box.

	$\mathbf{m}^{adcp}-\mathbf{m}^{est}$		$\mathbf{m}^{est}-\mathbf{m}^{filt}$		$\mathbf{m}^{filt}-\mathbf{m}^{adcp}$	
Degree	r^2	sd(diff) (cm/s)	r^2	sd(diff) (cm/s)	r^2	sd(diff) (cm/s)
			West Box:			
1	-0.116	7.700	1.000	0.135	-0.116	7.717
2	-0.078	7.839	-0.991	1.731	0.064	7.685
3	-0.070	7.832	-0.513	1.910	0.096	7.674
4	-0.048	7.830	-0.437	1.947	0.101	7.668
5	0.172	7.600	0.561	2.046	0.273	7.410
6	0.258	7.448	0.639	2.129	0.334	7.254
			Centre box:			
1	0.021	8.048	1.000	1.034	0.021	8.097
2	0.017	8.048	0.980	0.261	0.029	8.048
3	0.023	8.047	0.945	0.461	0.030	8.055
4	0.023	8.047	0.542	1.156	-0.075	8.236
5	0.020	8.047	0.310	1.203	-0.052	8.209
6	0.046	8.042	0.035	1.488	-0.077	8.295
			East box:			
1	0.481	7.716	-1.000	1.127	-0.481	8.313
2	0.463	7.720	0.910	3.925	0.548	6.478
3	0.022	7.735	-0.218	4.422	0.548	6.476
4	0.009	7.761	-0.318	4.533	0.563	6.394
5	-0.014	7.776	-0.293	4.922	0.581	6.297
6	0.048	7.742	-0.170	4.908	0.583	6.288

Table 4.4: Correlation and difference statistics for many-layer inversion solutions for West box.

	$\mathbf{m}^{adcp}-\mathbf{m}^{est}$		$\mathbf{m}^{est}-\mathbf{m}^{filt}$		$\mathbf{m}^{filt}-\mathbf{m}^{adcp}$	
Degree	r^2	sd(diff) (cm/s)	r^2	sd(diff) (cm/s)	r^2	sd(diff) (cm/s)
1	-0.010	7.697	1.000	0.116	-0.010	7.699
2	-0.096	7.817	-0.991	1.788	0.101	7.661
3	-0.093	7.816	-0.702	1.884	0.109	7.660
4	-0.079	7.812	-0.650	1.892	0.114	7.654
5	0.021	7.729	-0.113	2.477	0.248	7.464
6	0.034	7.719	0.034	2.825	0.308	7.329
7	0.074	7.692	0.166	2.808	0.332	7.264
8	0.106	7.661	0.245	2.798	0.360	7.182
9	0.095	7.722	0.208	2.986	0.365	7.166
10	0.342	7.236	0.605	3.135	0.522	6.566
11	0.336	7.259	0.482	3.605	0.517	6.590
12	0.287	7.424	0.381	4.039	0.525	6.550
13	0.190	7.808	0.154	5.108	0.547	6.445
14	0.209	7.805	0.178	5.162	0.546	6.450
15	0.207	7.816	0.178	5.165	0.547	6.443
16	0.203	7.837	0.144	5.364	0.540	6.484
17	0.186	7.890	0.163	5.263	0.558	6.386
18	0.168	7.971	0.078	5.850	0.554	6.431
19	0.151	8.532	0.201	6.284	0.549	6.473
20	0.085	9.029	0.183	6.617	0.555	6.432
21	0.107	8.964	0.190	6.635	0.574	6.323
22	0.040	9.521	0.085	7.438	0.584	6.271
23	0.008	9.735	-0.015	8.075	0.713	5.402
24	-0.038	10.630	-0.038	8.951	0.711	5.417
25	-0.025	10.570	-0.023	8.977	0.744	5.152
26	0.142	10.400	0.170	9.141	0.768	4.936
27	0.063	11.780	0.036	10.910	0.779	4.827
28	0.018	12.110	-0.004	11.290	0.805	4.572
29	0.123	12.440	0.086	11.940	0.829	4.311

Table 4.5: Correlation and difference statistics for many-layer inversion solutions for Centre box.

Degree	$\mathbf{m}^{adcp}-\mathbf{m}^{est}$ r^2	$\mathbf{m}^{adcp}-\mathbf{m}^{est}$ sd(diff) (cm/s)	$\mathbf{m}^{est}-\mathbf{m}^{filt}$ r^2	$\mathbf{m}^{est}-\mathbf{m}^{filt}$ sd(diff) (cm/s)	$\mathbf{m}^{filt}-\mathbf{m}^{adcp}$ r^2	$\mathbf{m}^{filt}-\mathbf{m}^{adcp}$ sd(diff) (cm/s)
1	0.006	8.049	1.000	0.927	0.006	8.100
2	0.003	8.051	0.722	0.259	0.013	8.052
3	0.009	8.049	0.665	0.249	0.019	8.049
4	0.087	8.028	0.857	1.304	0.104	8.038
5	0.070	8.033	0.284	2.156	0.217	7.871
6	0.078	8.029	0.360	2.191	0.217	7.877
7	0.189	7.917	0.532	2.195	0.275	7.746
8	0.154	7.955	0.564	2.303	0.228	7.888
9	0.216	7.874	0.617	2.293	0.282	7.745
10	0.198	7.894	0.622	2.274	0.273	7.770
11	0.091	8.097	0.417	2.658	0.269	7.781
12	0.169	7.948	0.392	3.167	0.391	7.414
13	0.103	8.095	0.102	4.231	0.428	7.289
14	0.084	8.463	0.036	5.012	0.445	7.210
15	0.070	8.513	0.053	4.993	0.439	7.239
16	-0.114	9.376	-0.253	6.778	0.509	6.943
17	-0.105	9.702	-0.305	7.498	0.504	6.975
18	-0.279	12.070	-0.377	9.887	0.559	6.677
19	-0.266	12.020	-0.332	9.980	0.586	6.536
20	-0.242	12.120	-0.316	10.160	0.592	6.493
21	-0.239	12.260	-0.366	10.630	0.584	6.560
22	-0.187	12.460	-0.255	10.780	0.583	6.571
23	-0.190	12.500	-0.247	10.770	0.583	6.568

Table 4.6: Correlation and difference statistics for many-layer inversion solutions for East box.

	$\mathbf{m}^{adcp}-\mathbf{m}^{est}$		$\mathbf{m}^{est}-\mathbf{m}^{filt}$		$\mathbf{m}^{filt}-\mathbf{m}^{adcp}$	
Degree	r^2	sd(diff) (cm/s)	r^2	sd(diff) (cm/s)	r^2	sd(diff) (cm/s)
1	0.414	7.724	-1.000	1.367	-0.414	8.379
2	-0.418	7.749	-0.825	3.976	0.597	6.244
3	-0.562	7.751	-0.894	4.056	0.551	6.459
4	0.179	7.665	-0.004	3.963	0.623	6.116
5	0.126	7.690	-0.101	4.485	0.615	6.109
6	-0.068	7.818	-0.319	4.859	0.620	6.073
7	-0.126	7.885	-0.384	5.083	0.638	5.961
8	-0.126	7.920	-0.263	4.931	0.640	5.954
9	0.268	7.453	0.264	4.843	0.678	5.698
10	0.278	7.448	0.238	5.020	0.679	5.687
11	0.237	7.565	0.227	5.040	0.669	5.755
12	0.197	7.687	0.169	5.247	0.670	5.750
13	0.182	7.790	0.008	5.987	0.638	5.964
14	0.001	8.776	-0.149	7.201	0.660	5.813
15	0.017	8.884	0.194	6.739	0.649	5.961
16	0.012	8.916	0.203	6.739	0.642	6.021
17	0.008	8.929	0.197	6.702	0.640	6.025
18	0.110	8.682	0.300	6.702	0.682	5.746
19	0.163	8.461	0.338	6.597	0.690	5.694
20	0.137	8.676	0.300	6.850	0.708	5.527
21	-0.007	9.907	0.111	8.420	0.772	4.941
22	0.018	9.896	0.129	8.399	0.808	4.566
23	0.090	17.940	0.015	17.950	0.831	4.300

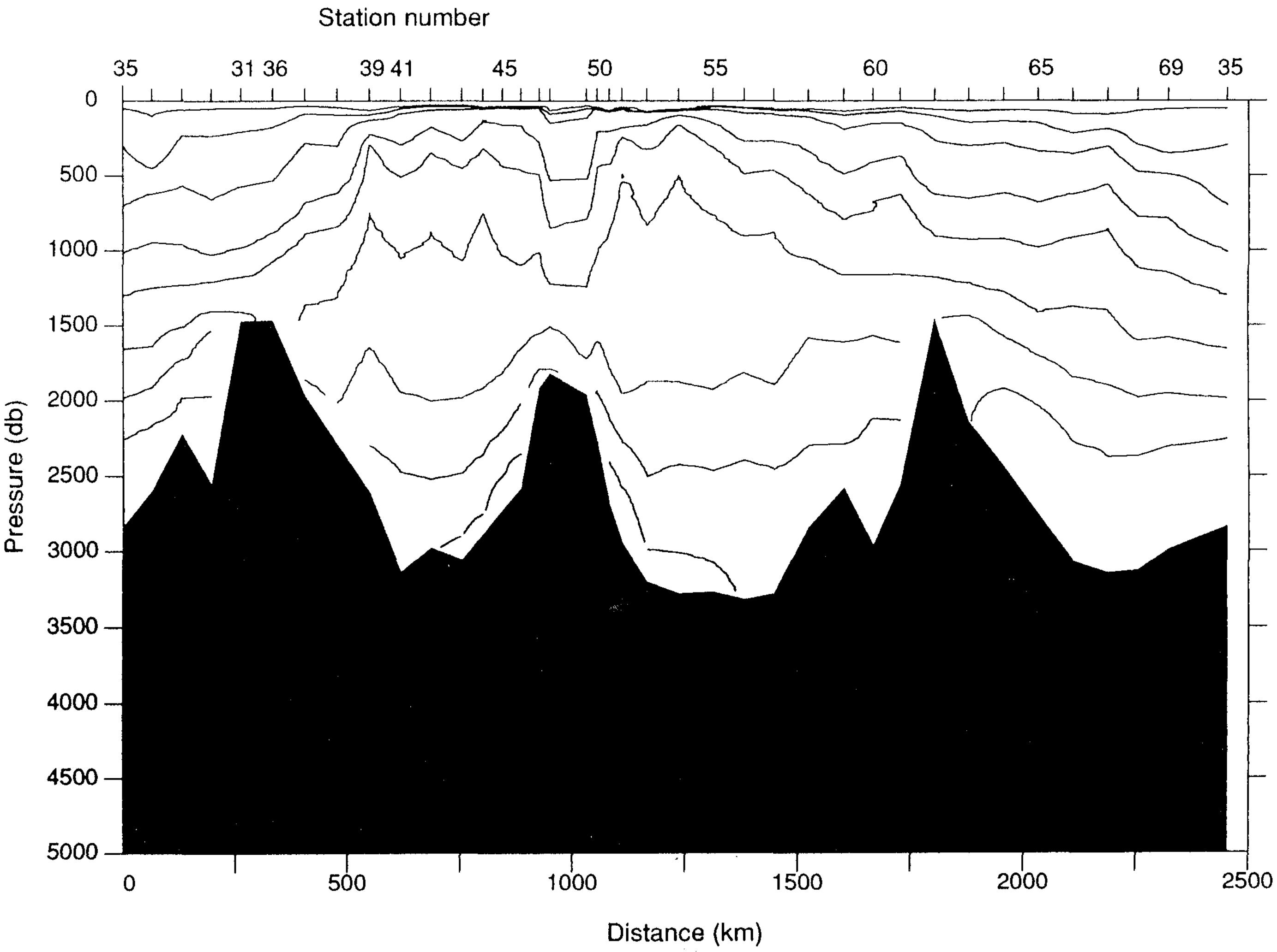

Figure 4.1: West box density structure in σ_0 and σ_2 (see Table 4.2).

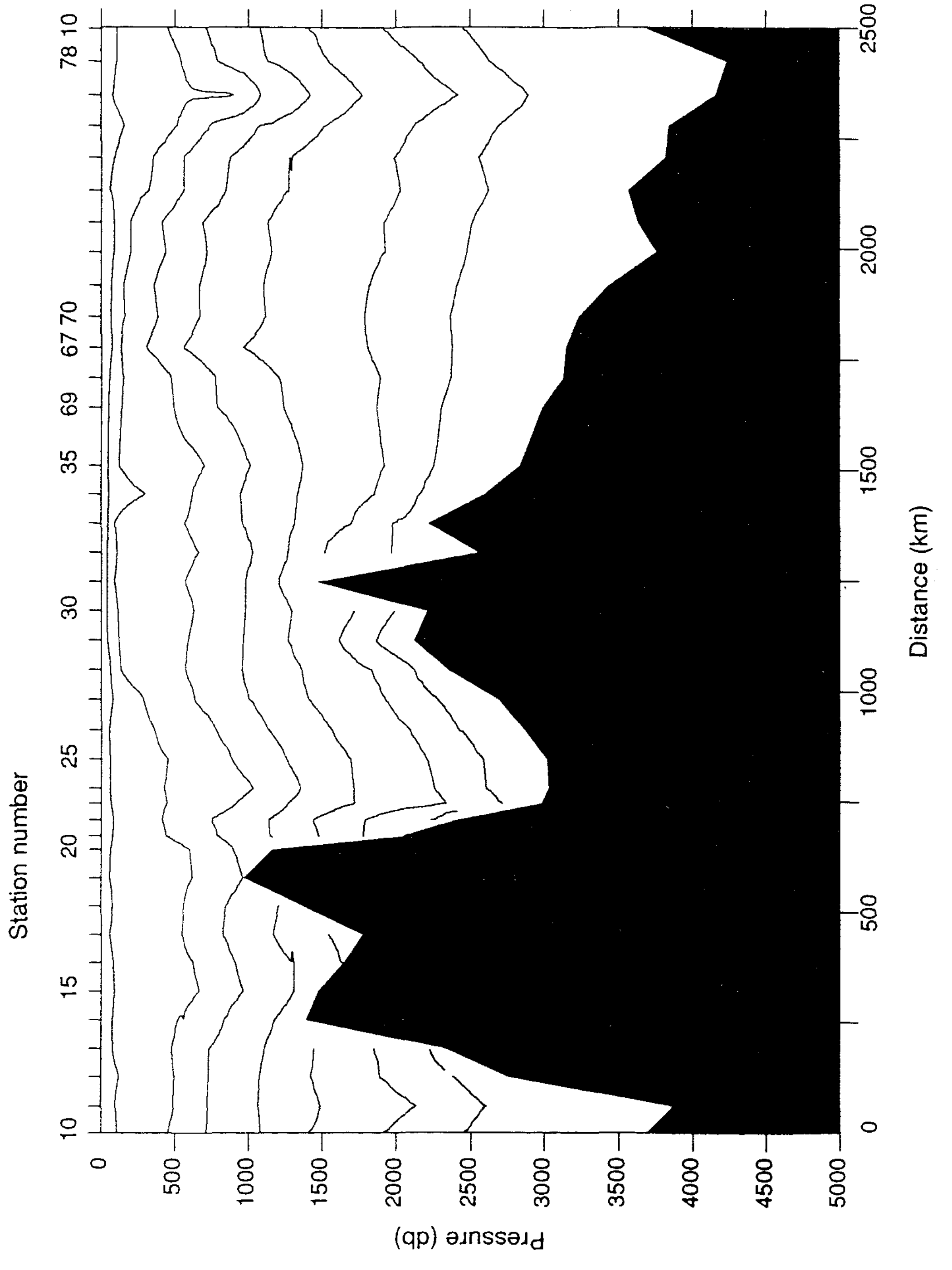

Figure 4.2: Centre box density structure in σ_0 and σ_2 (see Table 4.2).

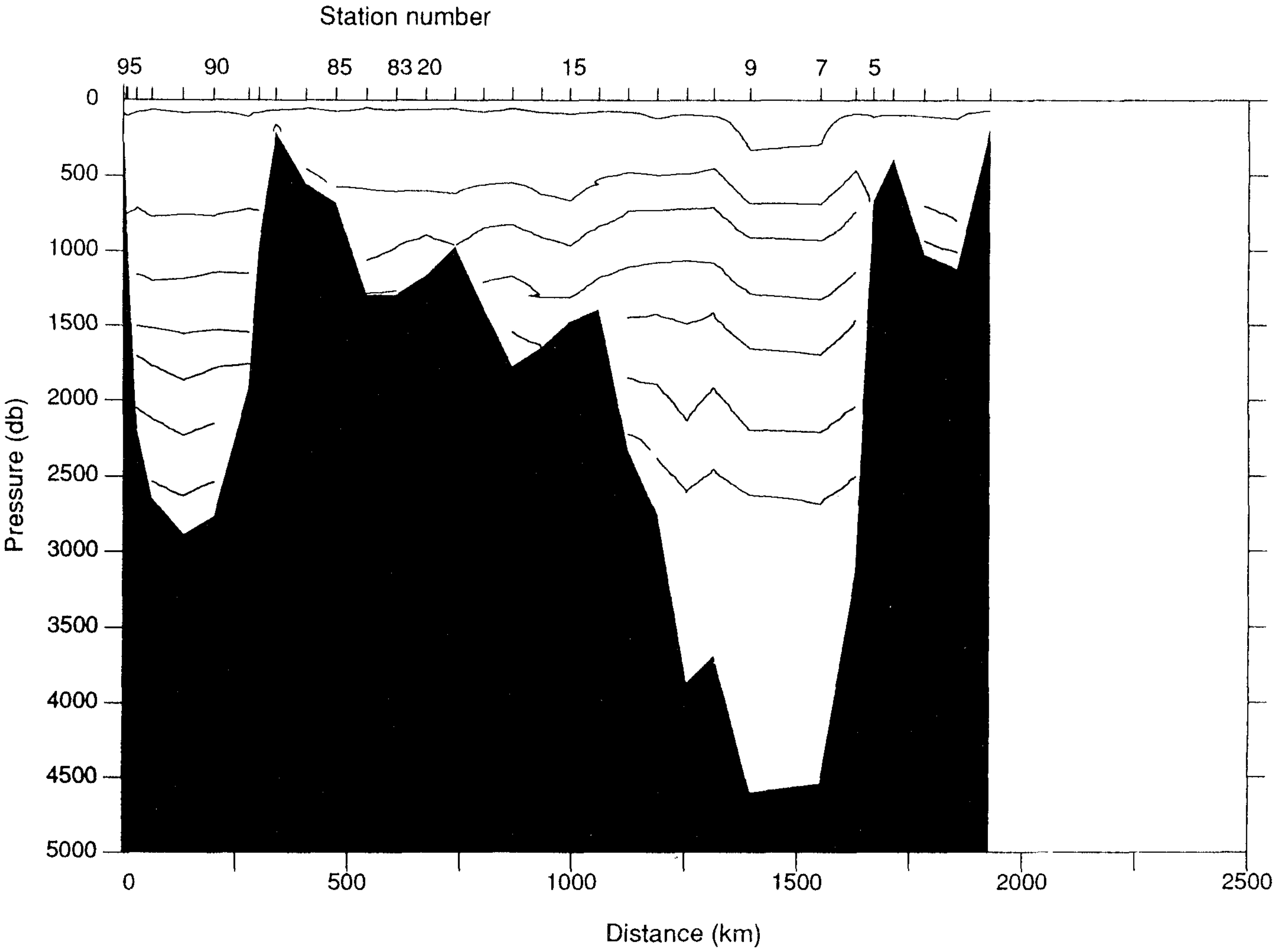

Figure 4.3: East box density structure in σ_0 and σ_2 (see Table 4.2).

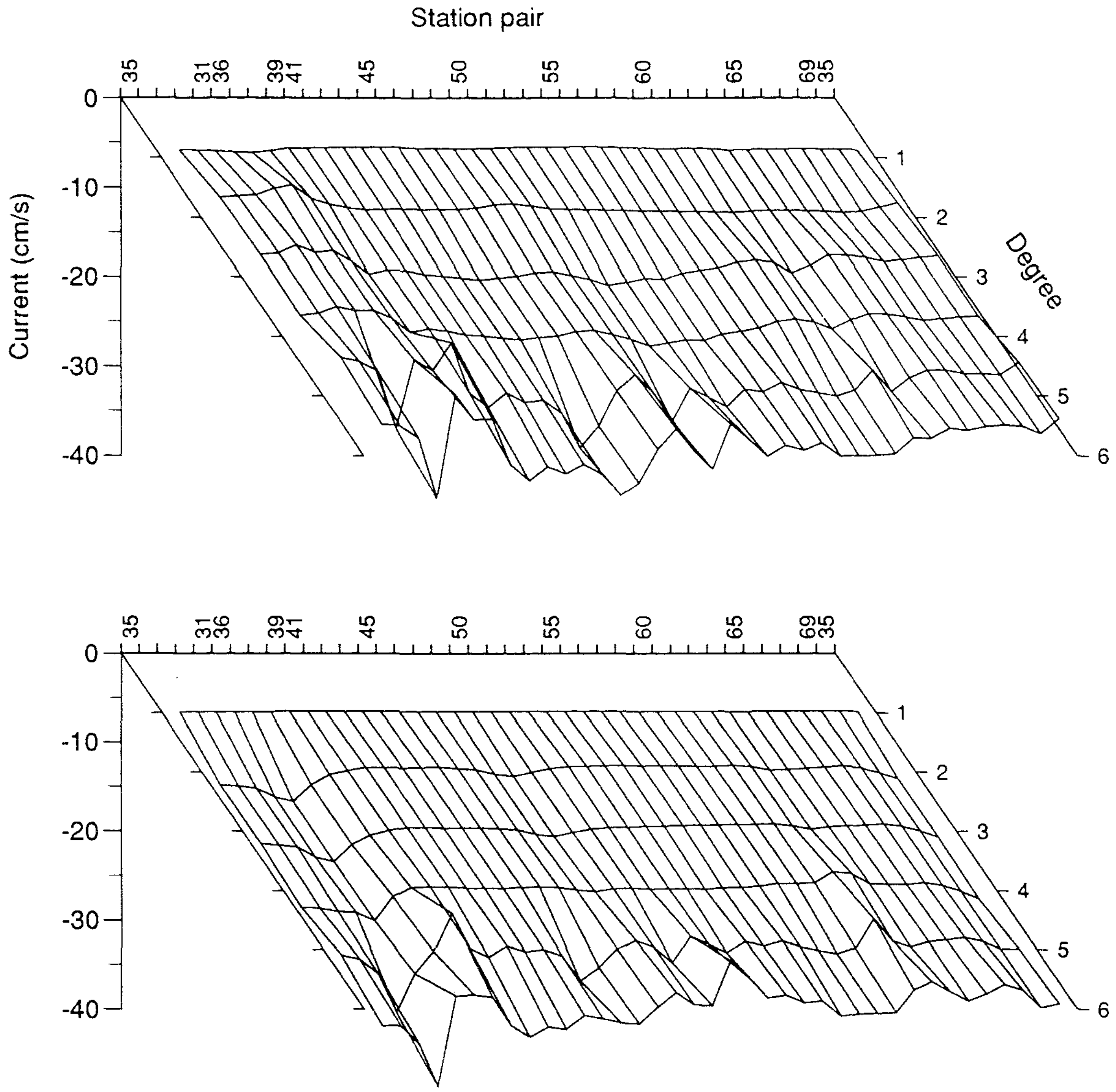

Figure 4.4: West box few-layer inversion solution by degree (lower net) and filtered ADCP solution by degree (upper net).

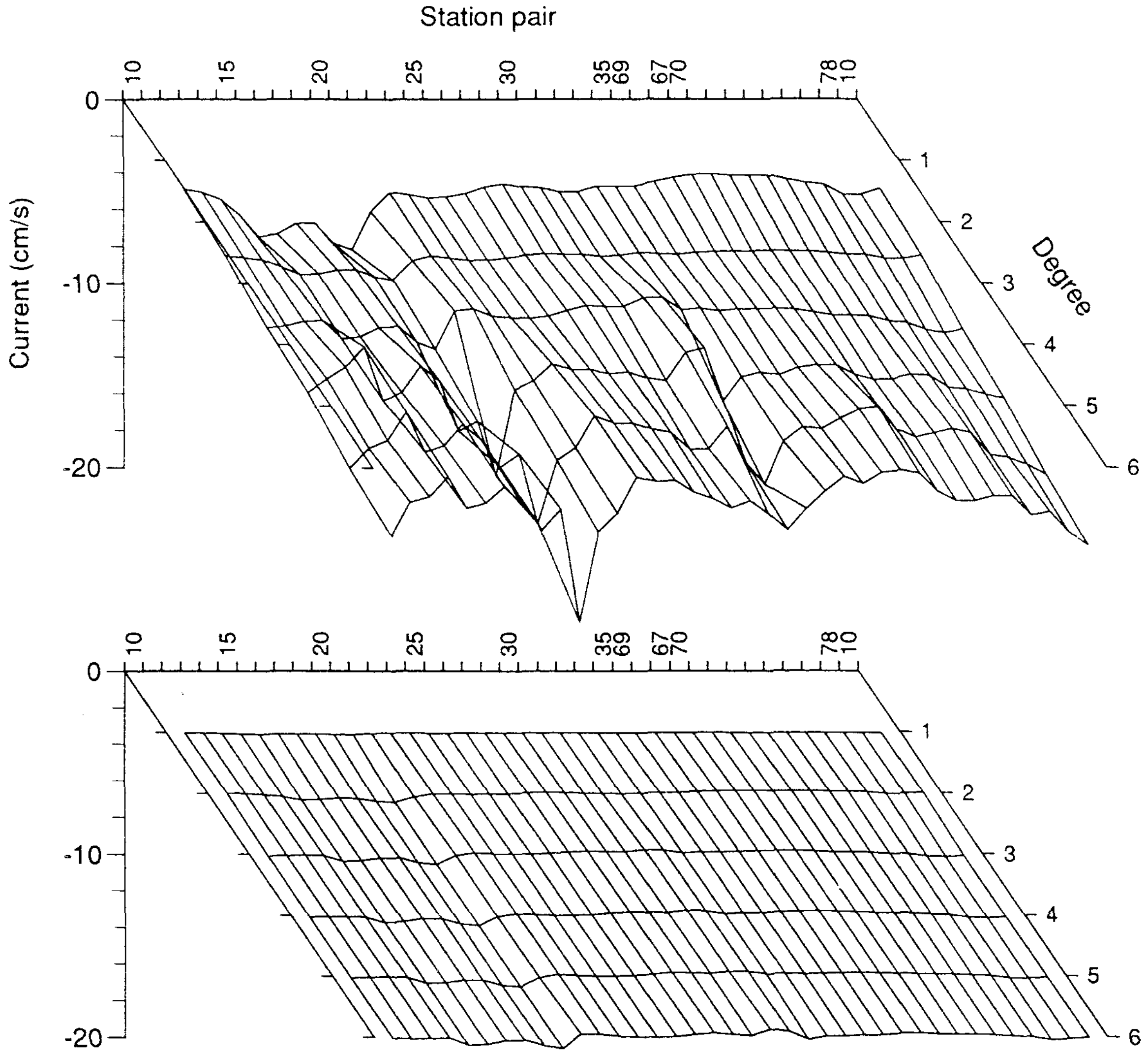

Figure 4.5: Centre box few-layer inversion solution by degree (lower net) and filtered ADCP solution by degree (upper net).

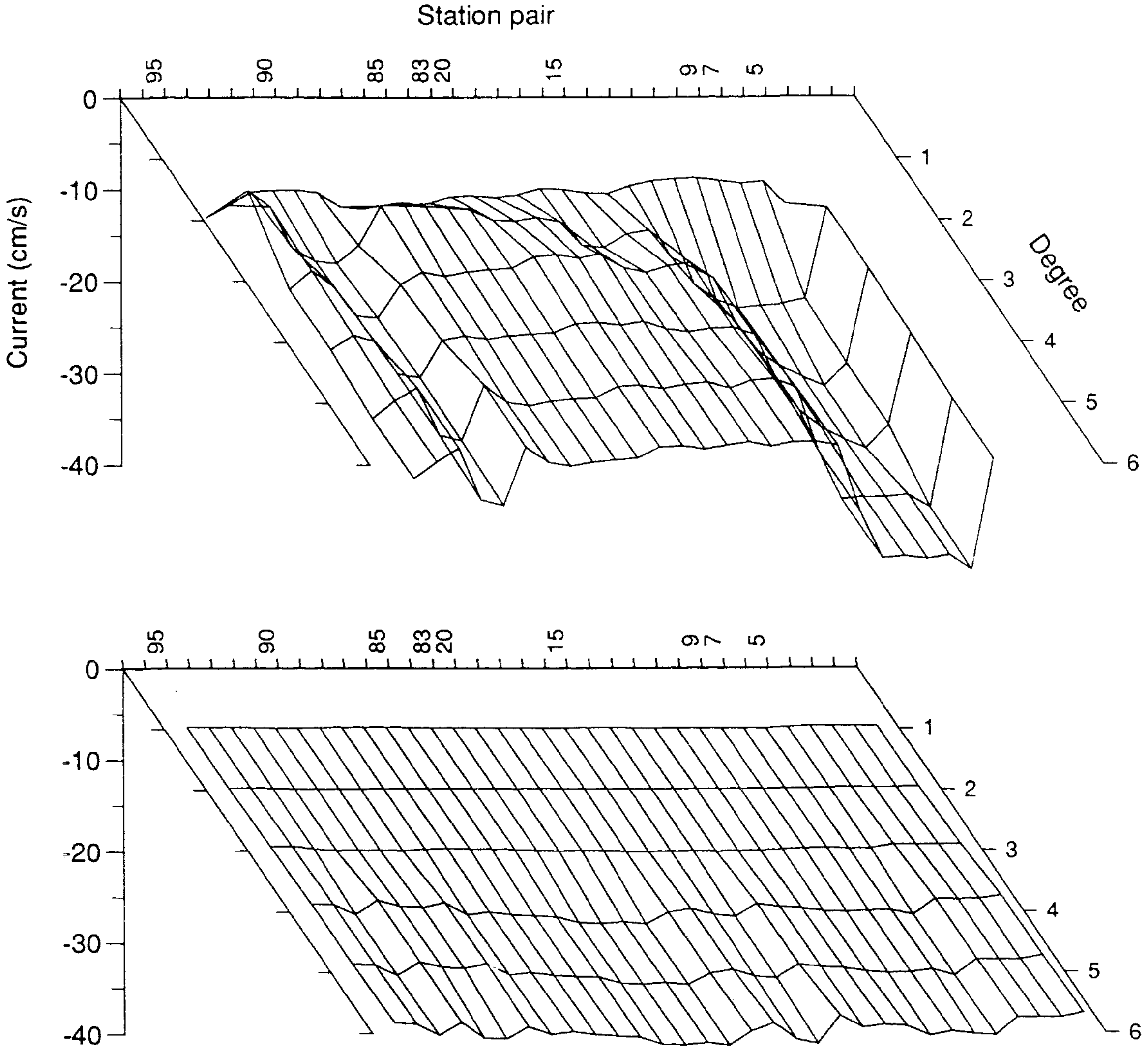

Figure 4.6: East box few-layer inversion solution by degree (lower net) and filtered ADCP solution by degree (upper net).

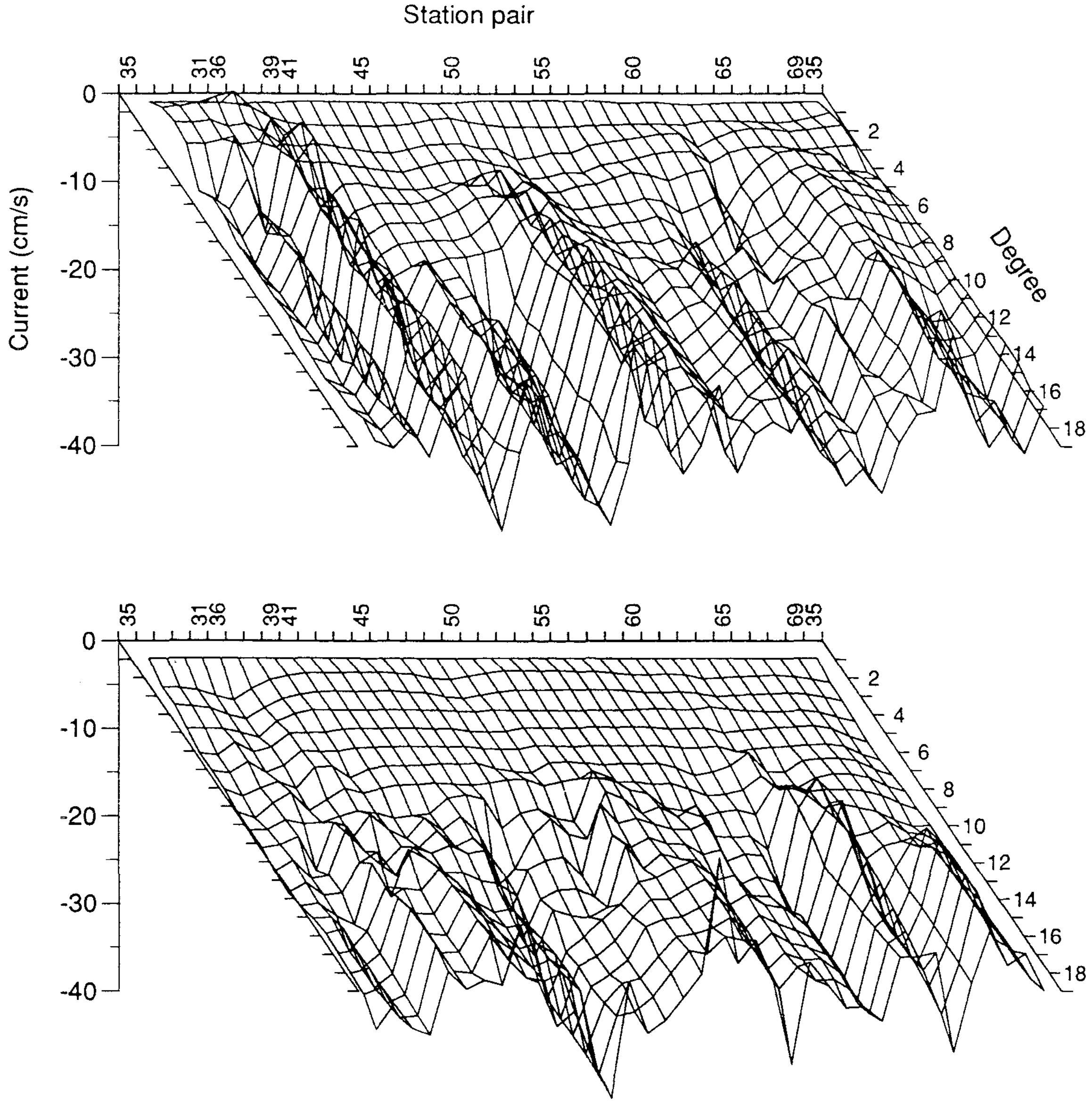

Figure 4.7: West box many-layer inversion solution by degree (lower net) and filtered ADCP solution by degree (upper net).

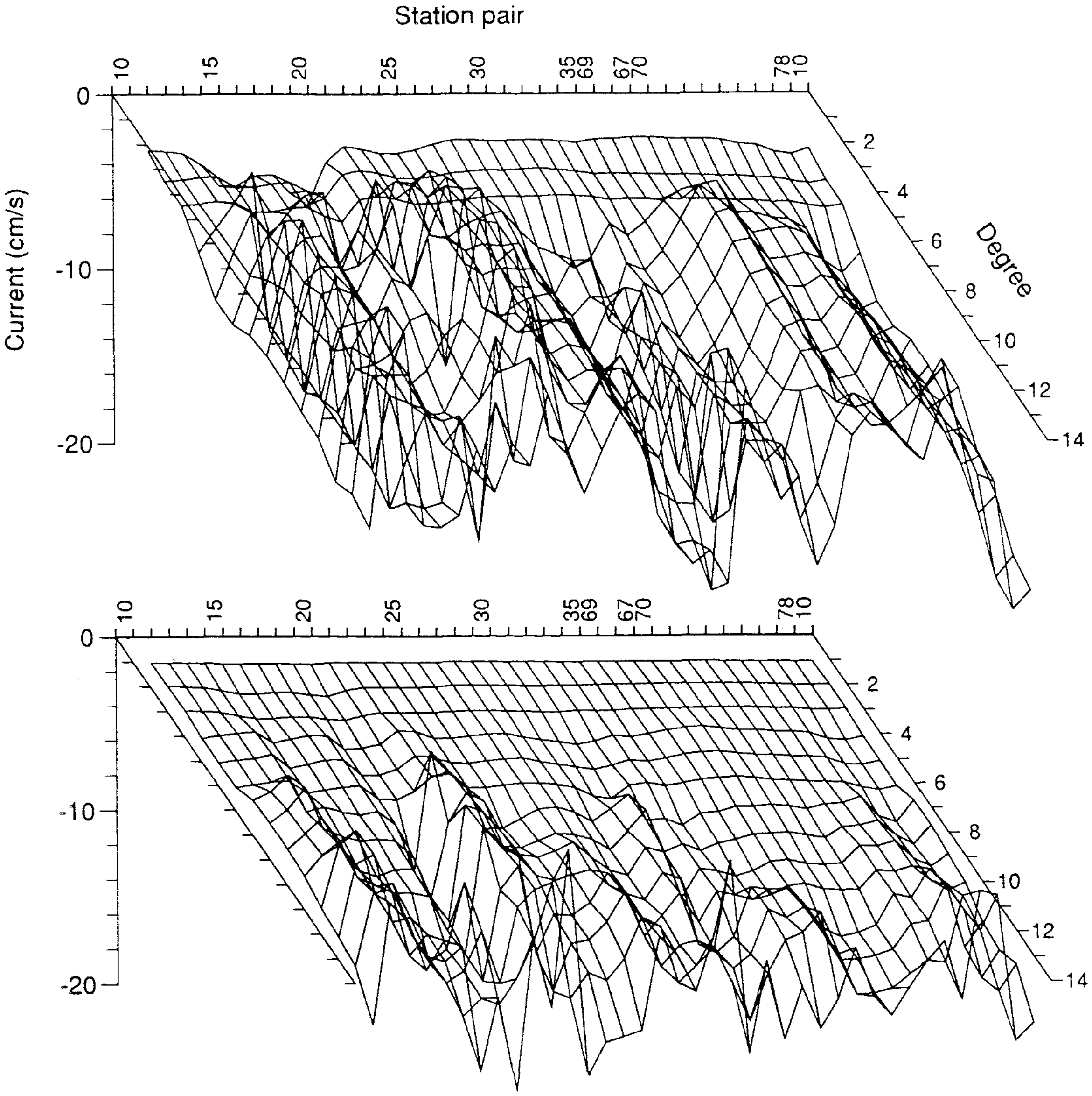

Figure 4.8: Centre box many-layer inversion solution by degree (lower net) and filtered ADCP solution by degree (upper net).

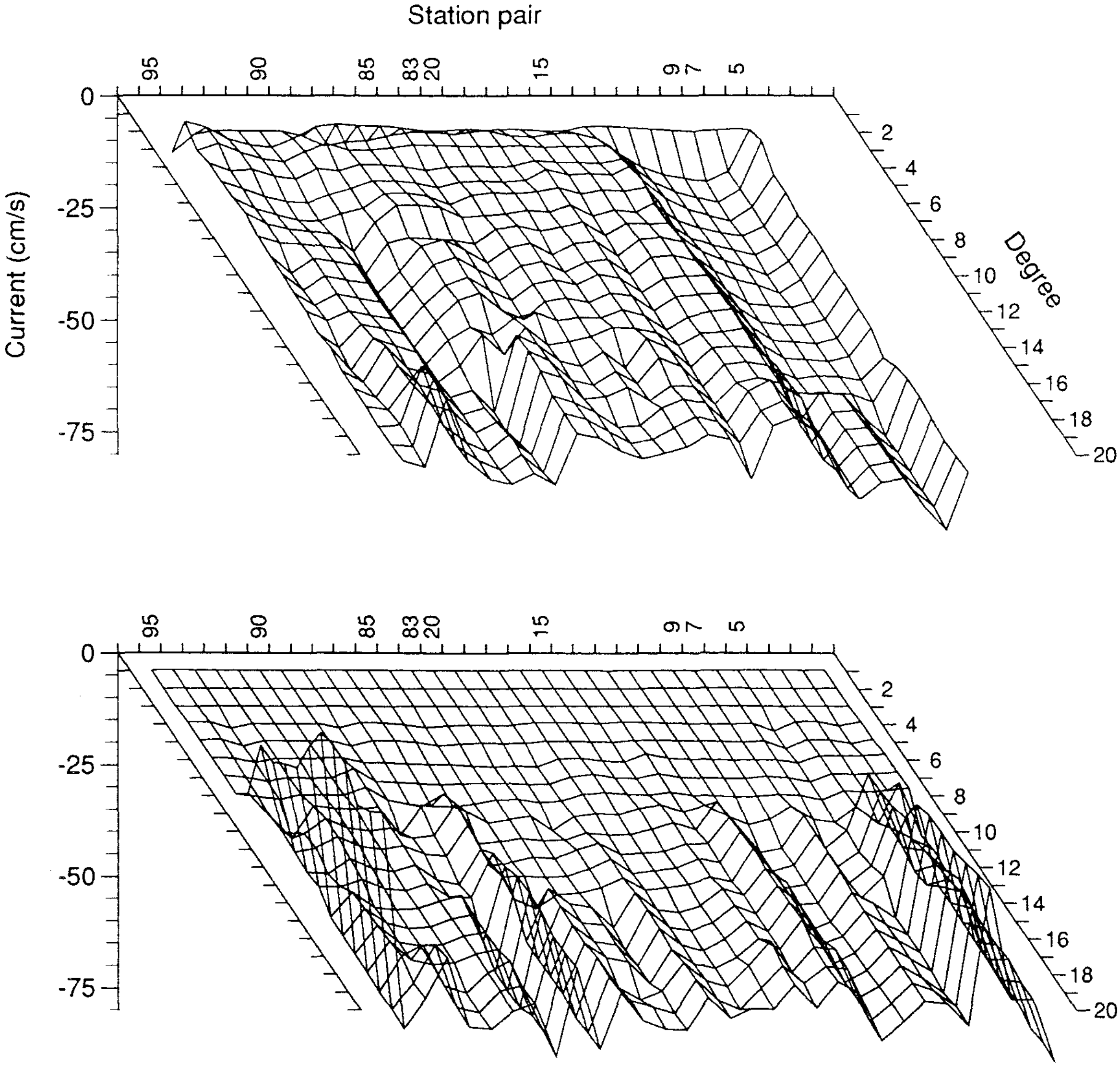

Figure 4.9: East box many-layer inversion solution by degree (lower net) and filtered ADCP solution by degree (upper net).

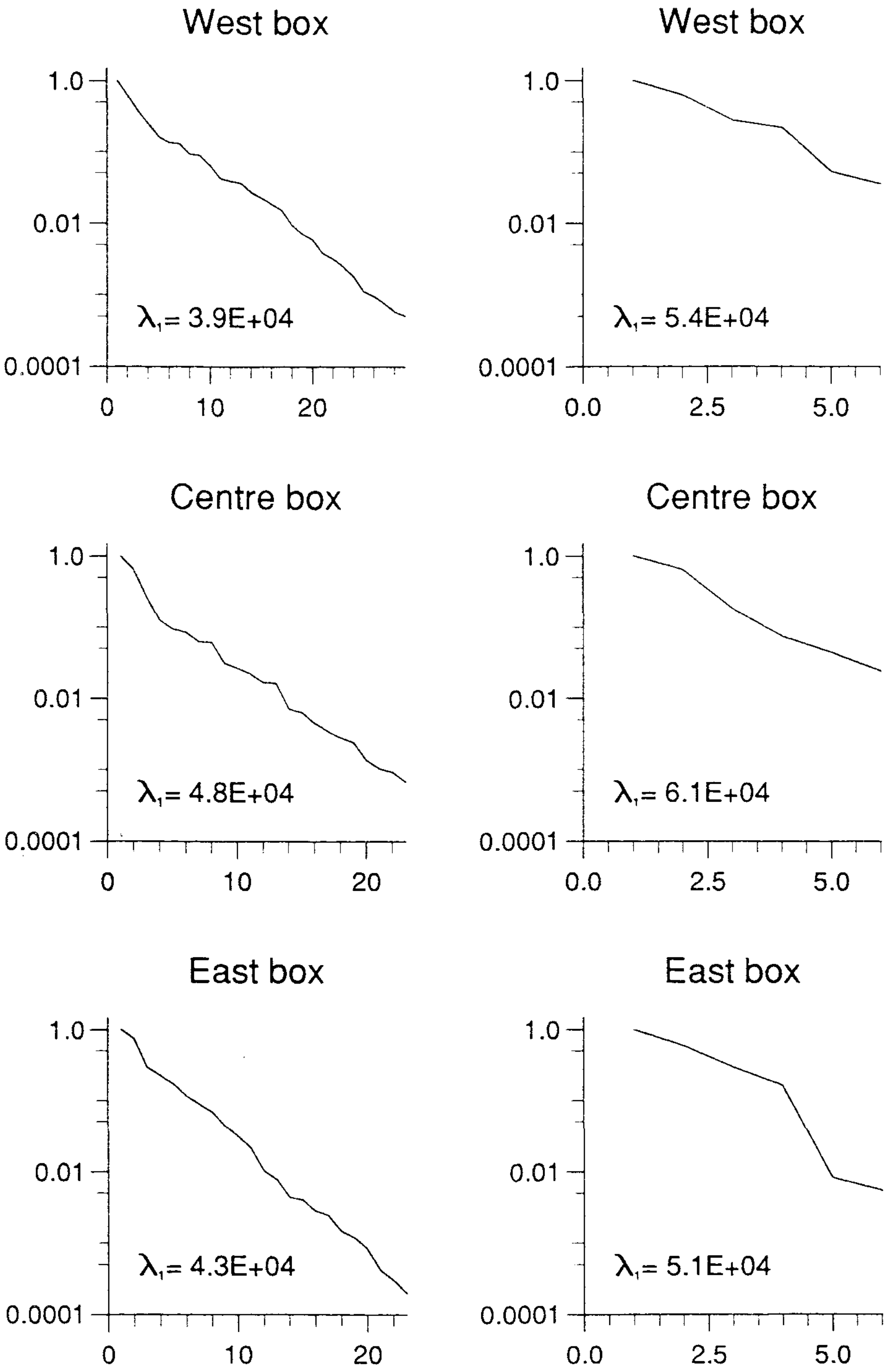

Figure 4.10: Inversion solution eigenvalues by degree, normalised on the first eigenvalue (λ_1) for each solution, and for each box. The left panel of each pair shows results for the many-layer solution, and the right panel for the few-layer solution.

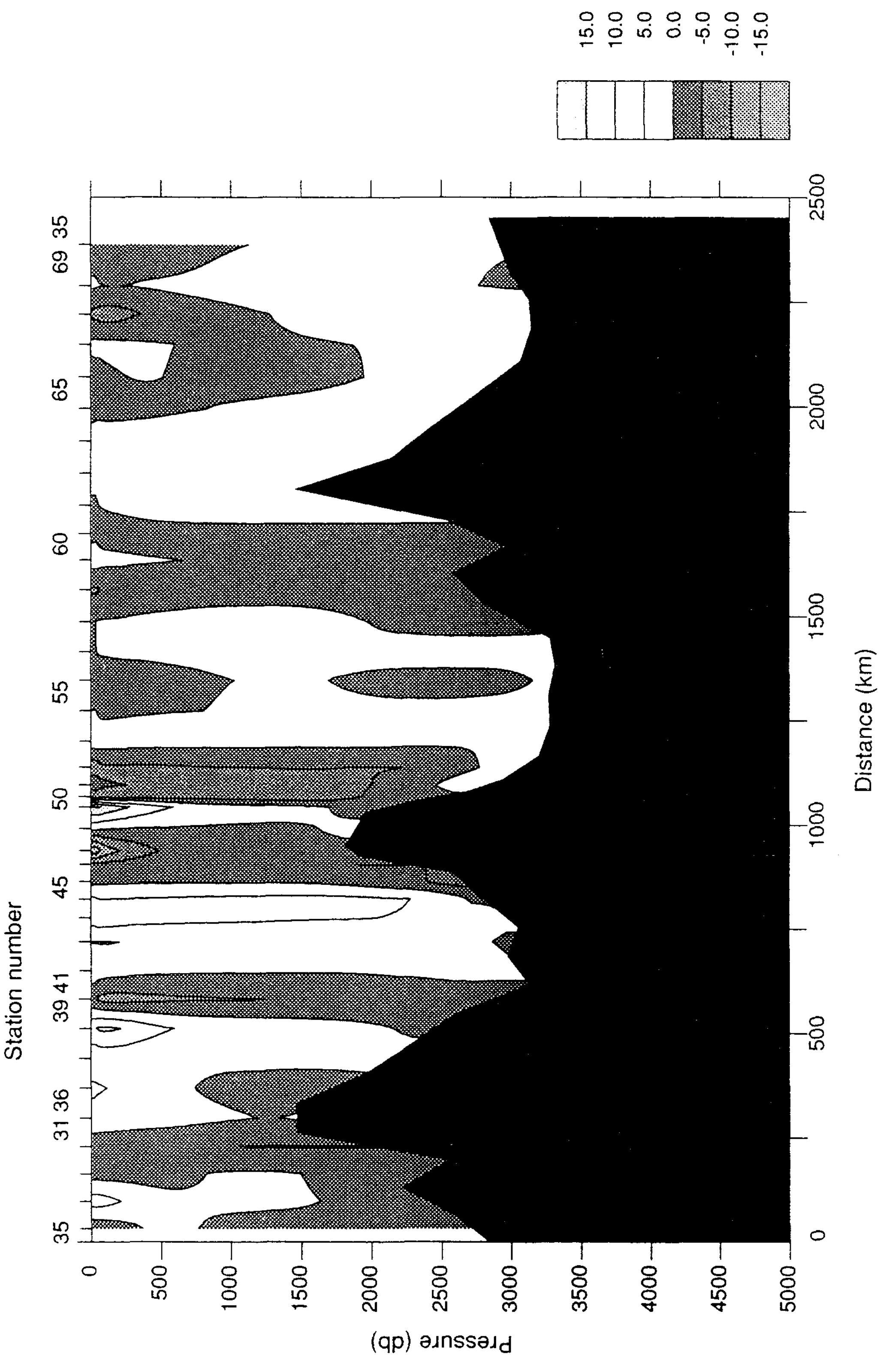

Figure 4.11 (a): Geostrophic velocity section (in cm/s) around West box referenced to many-layer solution degree 10; positive current is out of the box.

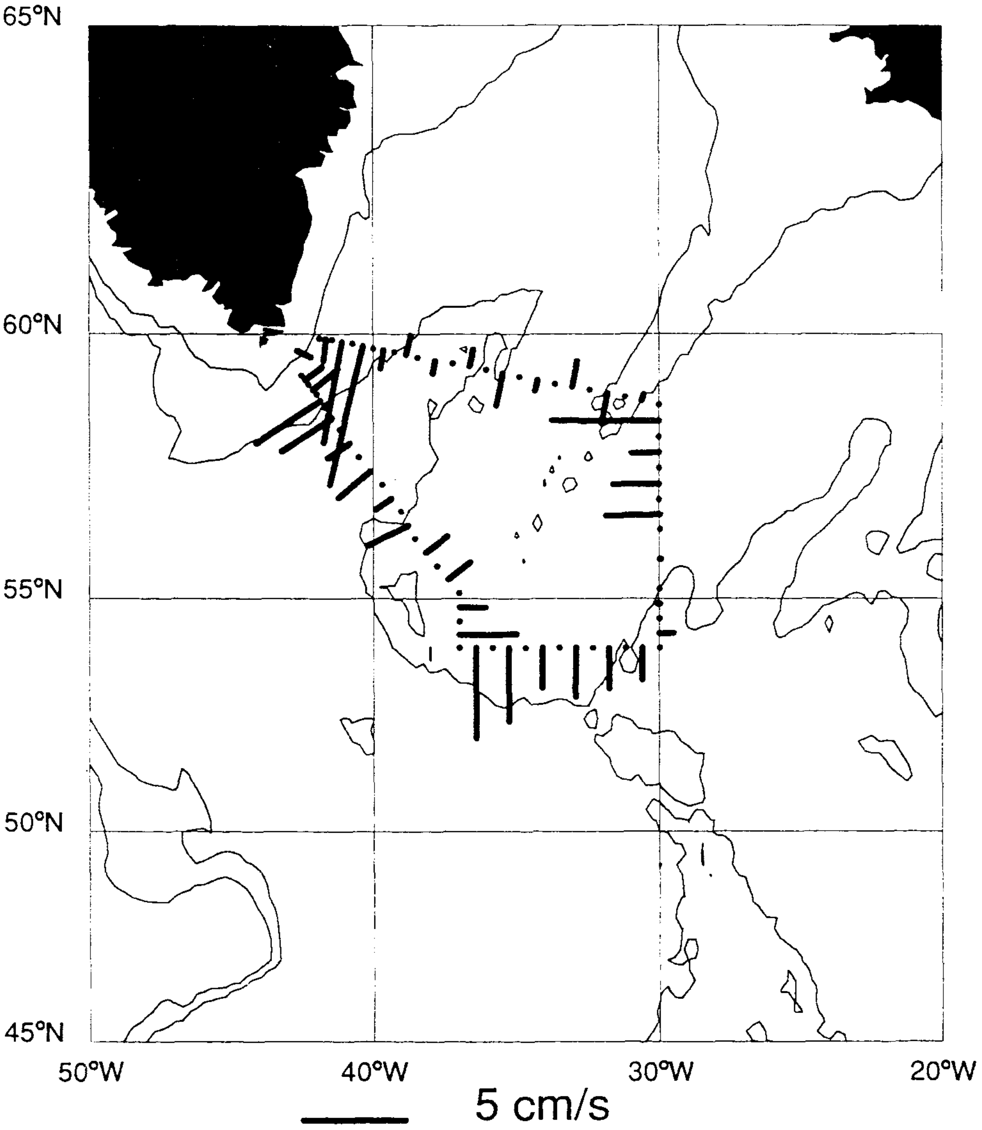

Figure 4.11 (b): West box degree 10 many-layer solution plotted over topography.

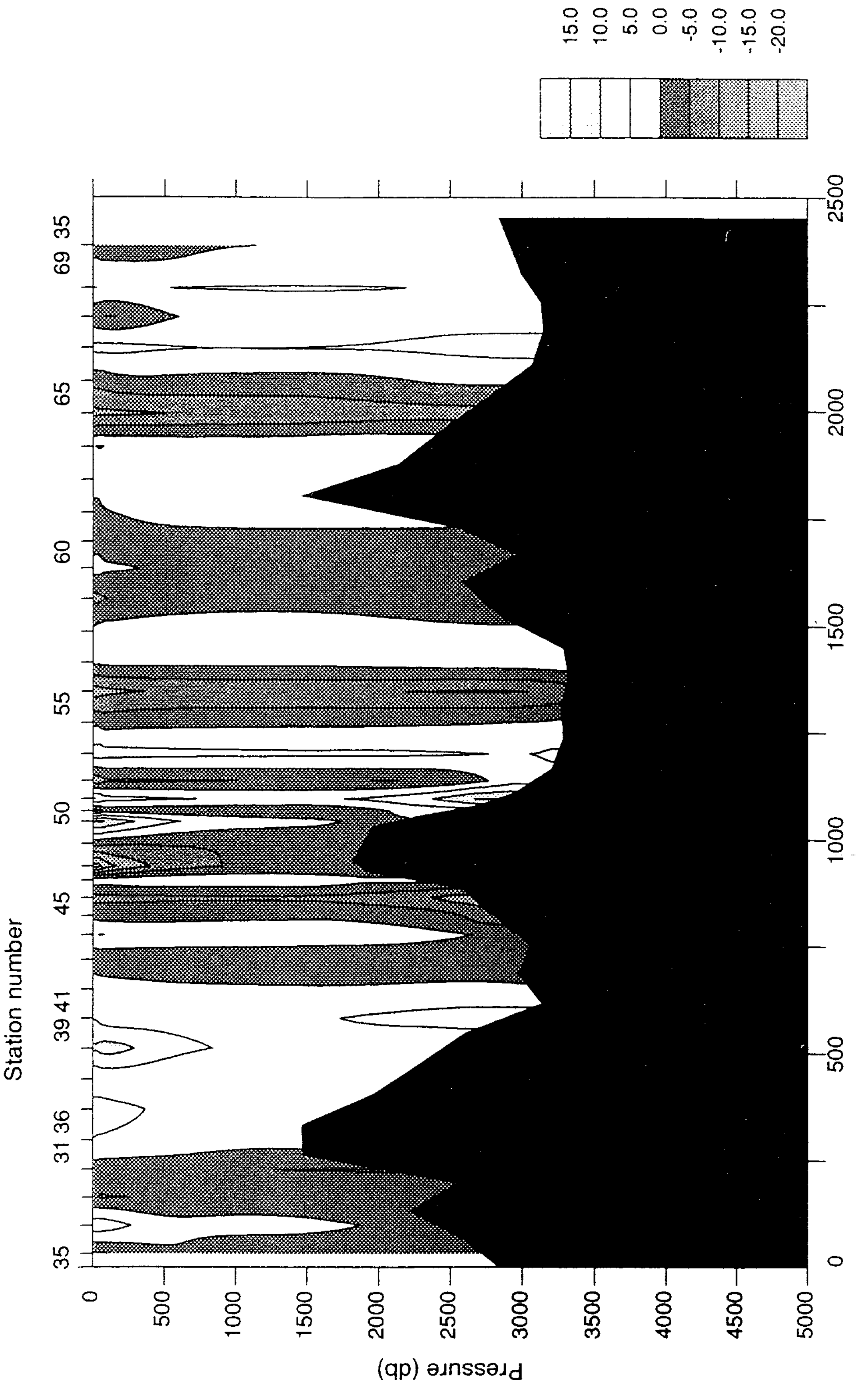

Figure 4.12 (a): Geostrophic velocity section (in cm/s) around West box referenced to many-layer solution degree 19; positive current is out of the box.

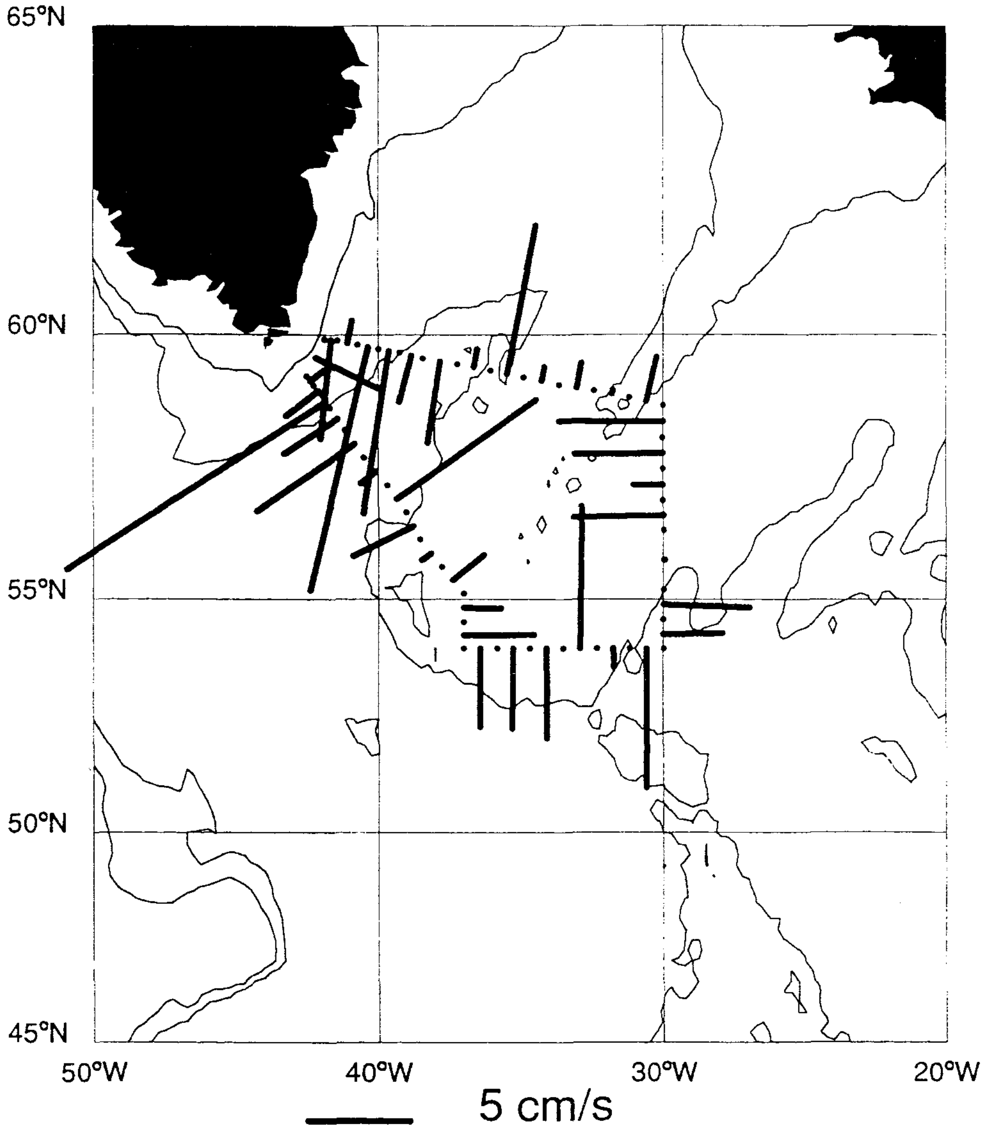

Figure 4.12 (b): West box degree 19 many-layer solution plotted over topography.

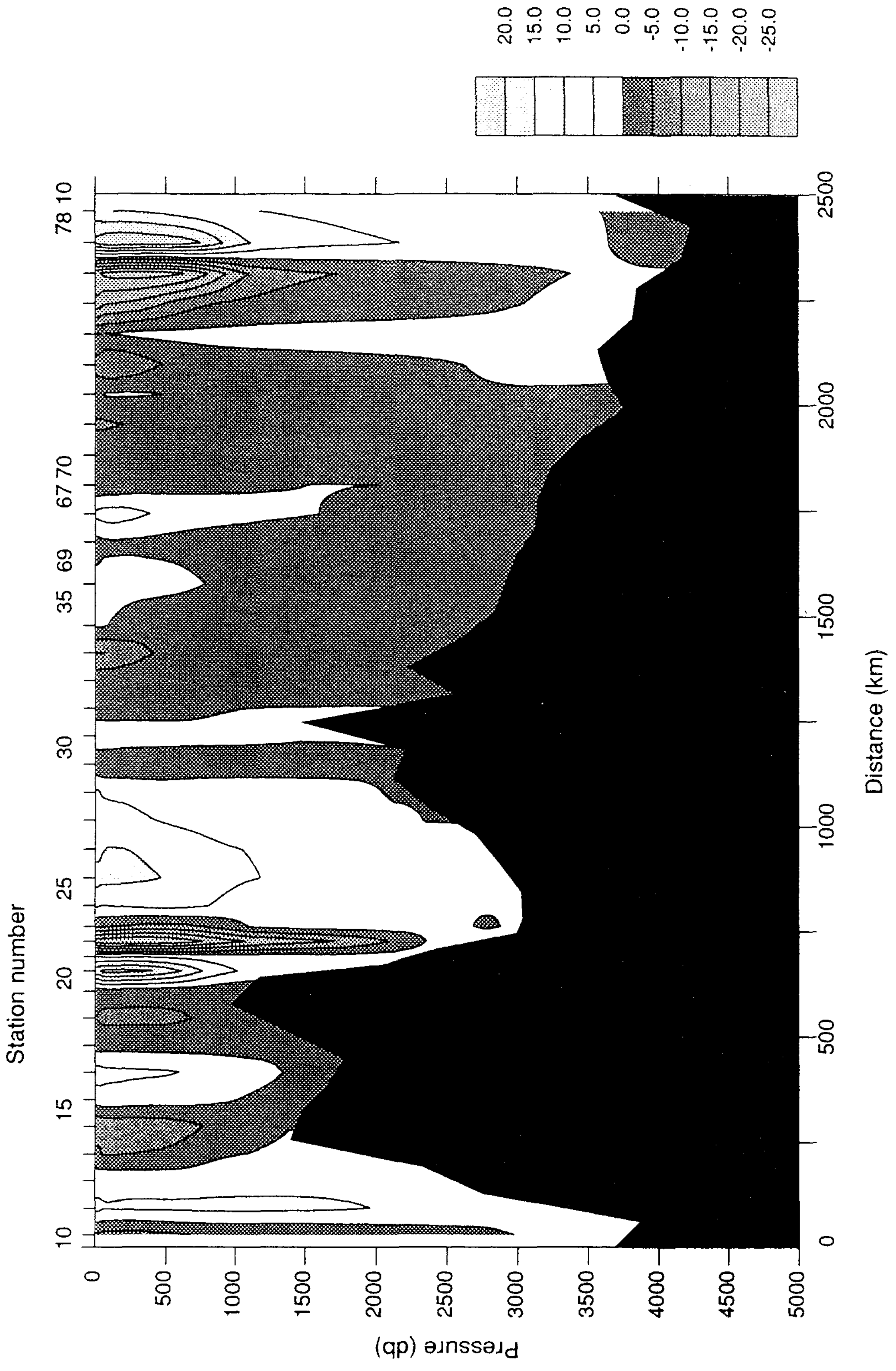

Figure 4.13 (a): Geostrophic velocity section (in cm/s) around Centre box referenced to many-layer solution degree 10; positive current is out of the box.

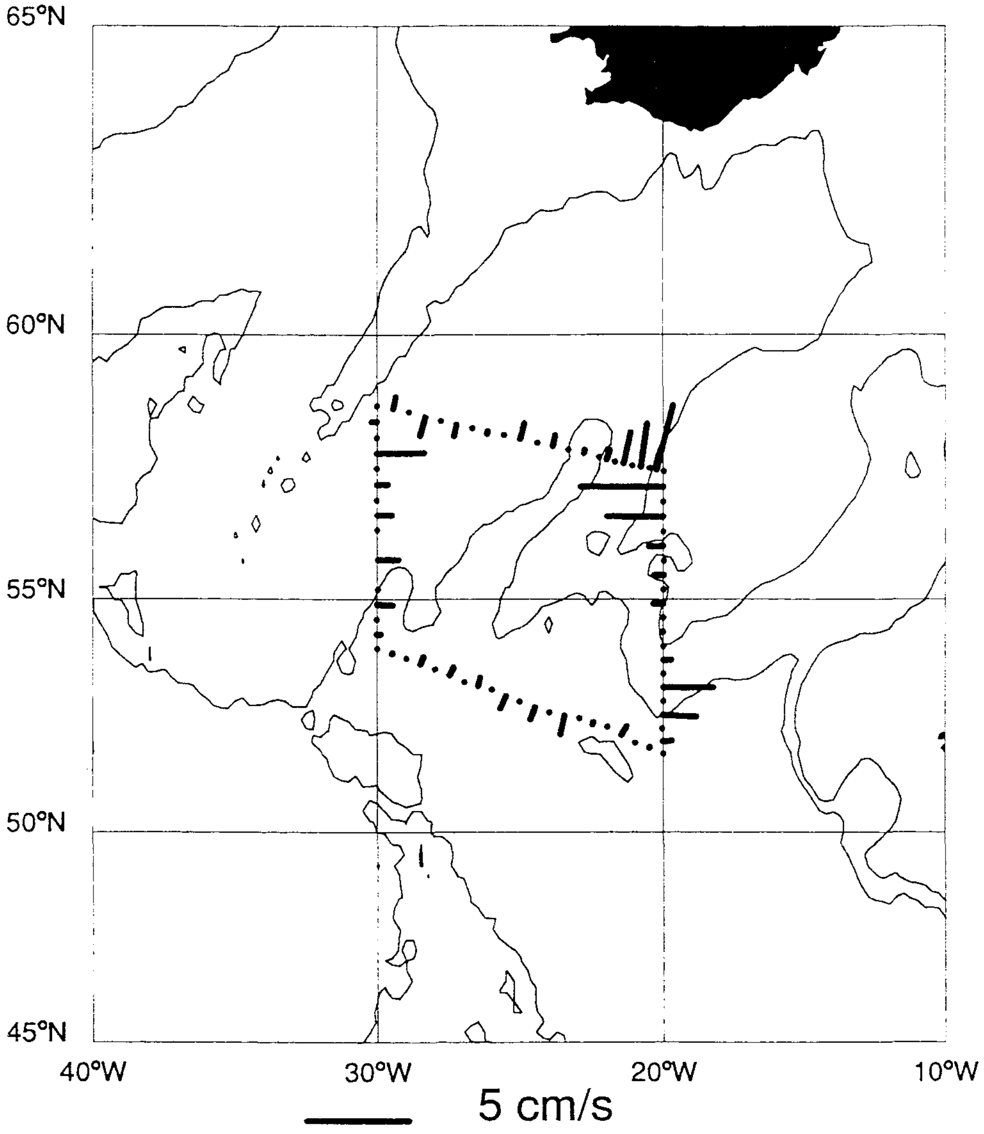

Figure 4.13 (b): Centre box degree 10 many-layer solution plotted over topography.

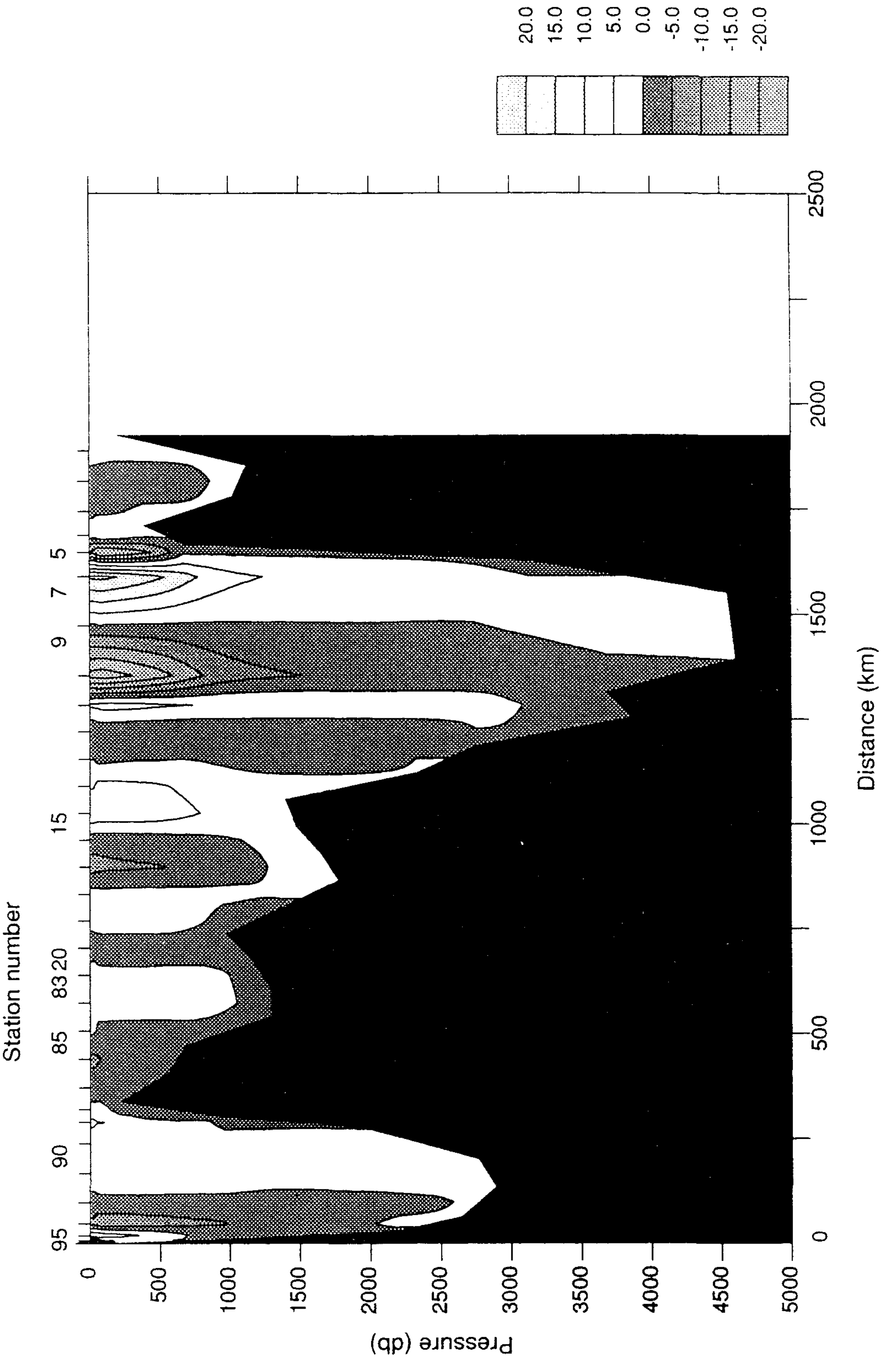

Figure 4.14 (a): Geostrophic velocity section (in cm/s) around East box referenced to many-layer solution degree 8; positive current is out of the box.

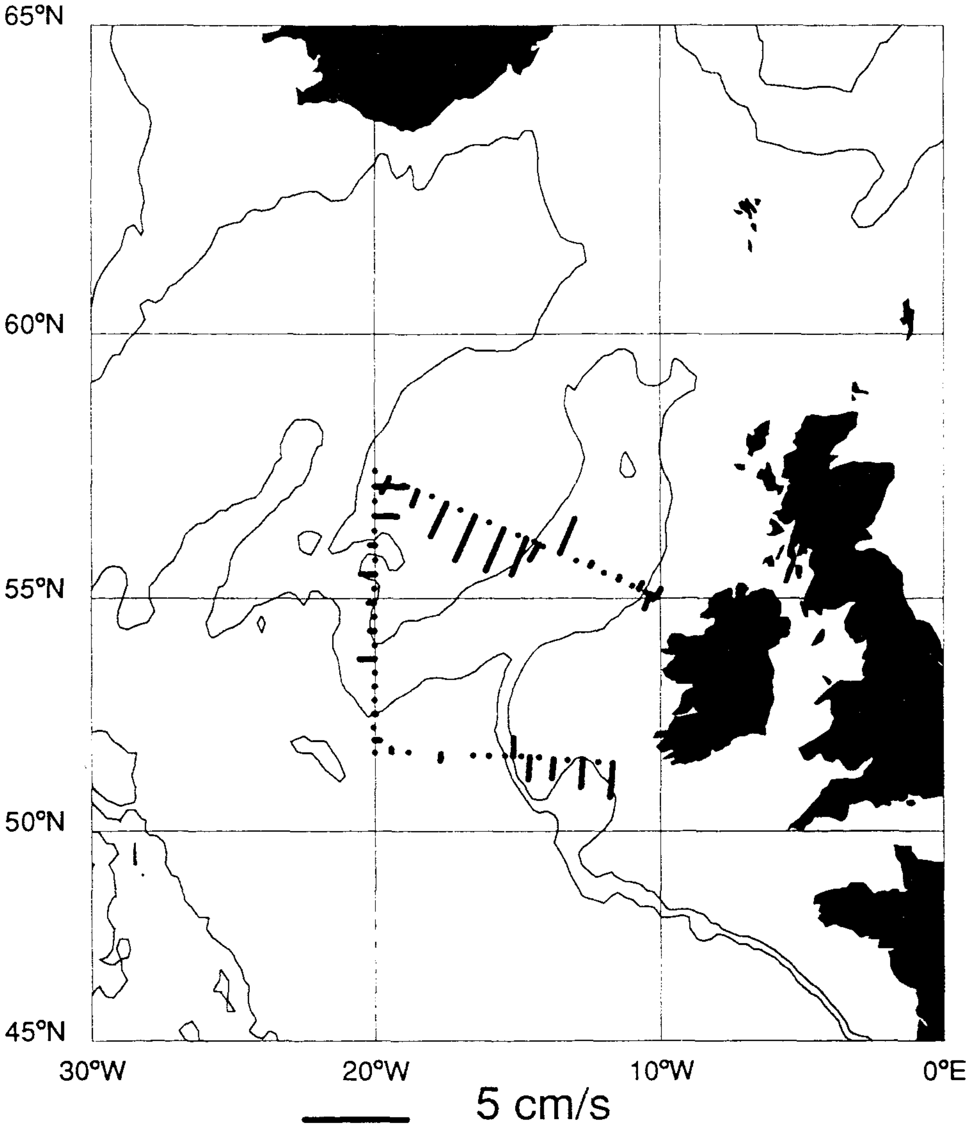

Figure 4.14 (b): East box degree 8 many-layer solution plotted over topography.

5. OPTIMISATION

5.1 Procedure

It is required, in some sense to be defined, to extract from the data the maximum information which can then be input to an inversion. The problem is posed as previously: find **m** given **G** and **d** such that $\mathbf{Gm} = \mathbf{d}$ and the inverse of **G**, $\mathbf{G}^-$, is defined through the mechanics of SVD such that $\mathbf{G} = \mathbf{U}\Lambda\mathbf{V}^\mathrm{T}$ and $\mathbf{G}^- = \mathbf{V}\Lambda^{-1}\mathbf{U}^\mathrm{T}$ where **m** is the solution vector (N station pairs × 1) of reference currents to be added to the 'first-guess' geostrophy, **d** is the vector of flux excesses (M constraints × 1), **G** (M constraints × N station pairs) the matrix of 'geometries' or (property-weighted) areas formed from station-pair separation times layer thickness; and **U**, **V** and Λ take their conventional SVD meanings. A constraint in this context is understood to be the requirement for conservation of the flux of volume or some property (heat, salt etc.) within a layer in the water column defined as existing between suitable limits (based on density, temperature etc).

The quantification of 'information' in this formalism is found in the eigenvalues Λ, so the identification of an optimal configuration will require the identification of some eigenvalue extremum. Now the eigenvalue structure is derived from **G**, which contains the section geometry (the configuration of the density levels in the data). Therefore the adjustment of the eigenvalues Λ will require the adjustment of the configuration of the layers into which the water column is divided. Criteria for optimisation are derived as in Barth and Wunsch (1990): with solution estimate **m**, the covariance of the solution estimate becomes

$$\begin{aligned}\mathrm{cov}[\mathbf{m}] &= \mathbf{mm}^\mathrm{T} \\ &= \mathbf{V}\Lambda^{-1}\mathbf{U}^\mathrm{T}\mathbf{dd}^\mathrm{T}\mathbf{U}\Lambda^{-1}\mathbf{V}^\mathrm{T} \\ &= \sigma^2\mathbf{V}\Lambda^{-2}\mathbf{V}^\mathrm{T}\end{aligned} \tag{5.1}$$

using the simplifying assumption that $\mathrm{cov}[\mathbf{d}] = \sigma^2\mathbf{I}$ (here only, σ^2 is a data variance), and eigenvector orthonormality. So with the inverse-square dependence of covariance on eigenvalue, the element of **m** with the largest error is the element with the smallest eigenvalue; the optimal solution is the **m** with least error, and since the error is dominated by the smallest eigenvalue (λ_M), the optimal configuration for **G** is the one with the largest λ_M.

We describe below how we apply this method, but we note first that no application comparable to the present one can be found in the literature. Barth and Wunsch (1990) contains a review of the most nearly related topic, that of experiment design, which is applied in such diverse contexts as measuring temperature on a heated rod, air monitoring and tomographic array design. The papers mentioned therein are generally involved with the selection of the 'best' option from a predetermined set, rather than the global optimum. Other papers which deal in the general area of optimisation are only of slight technical relevance. Barth and Wunsch (1990) deal specifically with tomographic array design using a similar criterion to the above, but they use simulated annealing to find their global optimum. We prefer, at least for this first go at the method, to use a different method, because simulated annealing is essentially a systematised form of random search which tells one little about the form of the space one is exploring.

For a given number of layers in the ocean and flux constraints on those layers, we wish to define layers such that the optimal condition of max(λ_M) is achieved. In the trivial case of one layer (from top to bottom), the only possible layer <u>is</u> the optimal configuration. Let us say that we now want to find the optimal two-layer case. The top and bottom of the ocean being fixed, we have one degree of freedom, which is the position of the level separating the two layers. We wish to scan this separation level from top to bottom and inspect the resulting distribution of λ_M versus the coordinate defining the separation level. First, the level scanning: this was done by defining a monotonic, high-resolution scale of points in the separation level coordinate, starting with the top of the ocean (the actual coordinate minimum determined from the data) and proceeding to the coordinate maximum (not the greatest depth either in the CONVEX region as a whole, or in its own immediate vicinity, the reason for which follows). Second, the separation level coordinate: since the maximum depth in the

CONVEX region is greater than 4000 m, it was decided to use potential density referenced to 2000 m (σ_2). One continuous variate was used for this coordinate, even though the format permitted the use of, say, σ_0 for the top 1000 m, etc., because the discontinuity between differently referenced potential densities interfered adversely with subsequent computations. However, when σ_0 was required, it was re-introduced. The necessary resolution was arrived at through a combination of trial-and-error, and the requirement for higher resolution in the vicinity of higher gradients of σ_2. This resulted in a scale of σ_2 levels separated by about 50 m (mean vertical difference) in the top 300 m, increasing to about 150 m for the interior of the water column, then decreasing to 50 m again for the Denmark Strait Overflow, giving a total of about 30 points on the scale. Having located the optimal configuration on the scale, the resolution was increased by application of a bisection algorithm until a resolution equivalent to ± 10 m mean in the vertical was achieved. This method of optimisation by 'brute force' is referred to below as 'full-space search'.

Referring back to the location in the water column of the coordinate maximum, the Denmark Strait Overflow has the greatest potential density in the CONVEX region, and is found some way above the greatest depth in the Irminger Basin, and on its west side. Also, the Irminger Basin is shallower than the Madeira Basin, on the east side of the CONVEX region. For this reason, mean level depth will not serve as a proxy for the vertical coordinate, although it retains its usefulness where the levels are not far apart, as for the bisection process.

Two technical points: at a later stage in the work I tried locating the optimal point using a gradient-descent algorithm; as this could only be persuaded to work on the simplest cases, this method was abandoned in favour of the sole use of the full-space search. Also, although this method can easily be used in the mode of applying constraints based on the flux of any suitable quantity, in practice only volume constraints were used. If heat conservation was included, it was necessary to omit the heat constraint in the top layer, because the constraint is invalidated by heat exchange with the atmosphere; the resulting optimising computation including the heat constraint in all other layers was difficult to interpret, because the total variance was different in each case. If salinity was included similarly, although the computation worked, the resulting optimal layer structure was compressed into the upper ocean around the North Atlantic Current where the greatest salinity variability is to be found, biasing the layer structure away from the perceived water-mass structure. This is because one is effectively including salinity twice: once explicitly, and once through the dependence of density on salinity; therefore it is over-weighted. In all that follows where numbers of layers are referred to, it will be understood that volume constraints only are applied.

The results of scanning the single separation level in a two-layer system are shown in figure 5.1, and of scanning two separation levels in a three-layer system in figure 5.2. In both cases the optimum is clear and well-determined; accordingly, we proceed next with higher-dimensioned determinations, but note that ultimately, in the limit of some large number of layers which we do not attempt to determine, we would expect the smoothness of the solution (M-dimensional) surface to deteriorate, as layers become so thin as to be devoid of information orthogonal to neighbouring layers, in which case there are many small eigenvalues, none of which are significantly different from zero. That this regime is not being approached in the determination of optimal configurations here is addressed below.

The optimal separation levels for up to 6 levels (7 layers) are shown in figure 5.3. The full-space search very quickly becomes hungry for computer time, which is the practical restriction on the number of layers to be determined; for N layers, N–1 separation levels, and a search scale of J levels, there are $\prod_{i=1}^{N-1}(J-i+1)/(N-1)!$ unique combinations of N-1 levels to search.

The most arresting aspect of figure 5.3 is the consistency of the identification of layer boundaries (separation levels) by this optimal technique. The first level identified in the two-layer search is about $\sigma_2 = 36.87$, and this level reappears in all subsequent determinations. The next level identified is about $\sigma_2 = 36.3$, which is held until the search is extended to six layers, when the top two layers from the previous determination appear to be split into three. Two deep levels are picked out, at around $\sigma_2 = 36.94$ and 37.02. In order to proceed, we must choose a set of layers, so we settle on 5 (4 separation levels), for the rather subjective reasons that the resulting configuration looks good (see below), and that the consistent picking of levels stops here, with the next set (5 levels) apparently enforcing a splitting of the top two layers, as mentioned above.

Since it is desirable to use σ_0 for near-surface data, this was implemented by fixing the deeper σ_2 values and re-running the optimisation on a σ_0 scale, searching for one σ_0 level only, for the data above the highest σ_2 level only. By this means one finds the 'right' σ_0 level and not a value 'converted' from σ_2.

5.2 Description of levels in the context of the data

The density levels for the five-layer optimal configuration, which are $\sigma_0 = 27.425$, $\sigma_2 = 36.873$, 36.944 and 37.024, are shown for all CONVEX data in figure 5.4. The selected EGC stations (excluding 2616, which is in the same position as CONVEX 49) are also included with densities as calculated from their original properties, but with temperatures and salinities in subsequent plots adjusted by the amounts described in section 2 (the mean IGY minus CONVEX differences) to bring them up to 'modern' values. Figures 5.5–5.6 show sections of potential temperature and salinity; figure 5.7 shows θ-S diagrams, with the selected density levels superimposed. This last figure also includes East Greenland Current data, which will be described further in section 6.1.

The top layer is very thin to the west of the Mid-Atlantic Ridge (MAR), where it is mainly Sub-Arctic Intermediate Water (SAIW), and increases in thickness eastwards as a warm, saline layer of North Atlantic Central Water (NACW). The second layer is a mixture of changing proportions between the overlying distributions of SAIW and NACW, and the underlying Labrador Sea Water (LSW). The third layer is the core of the LSW, whose properties are most extreme (cold and fresh) in the west. The fourth and fifth layers are complicated confections of North Atlantic Deep Water (NADW), Denmark Strait Overflow Water (DSOW, the coldest, most dense water in the survey), Iceland-Scotland Overflow Water (ISOW), and some Antarctic Bottom Water (AABW) at depth in the east. For thorough definitions of water masses and their properties, see Harvey and Arhan (1988) and Reid (1994).

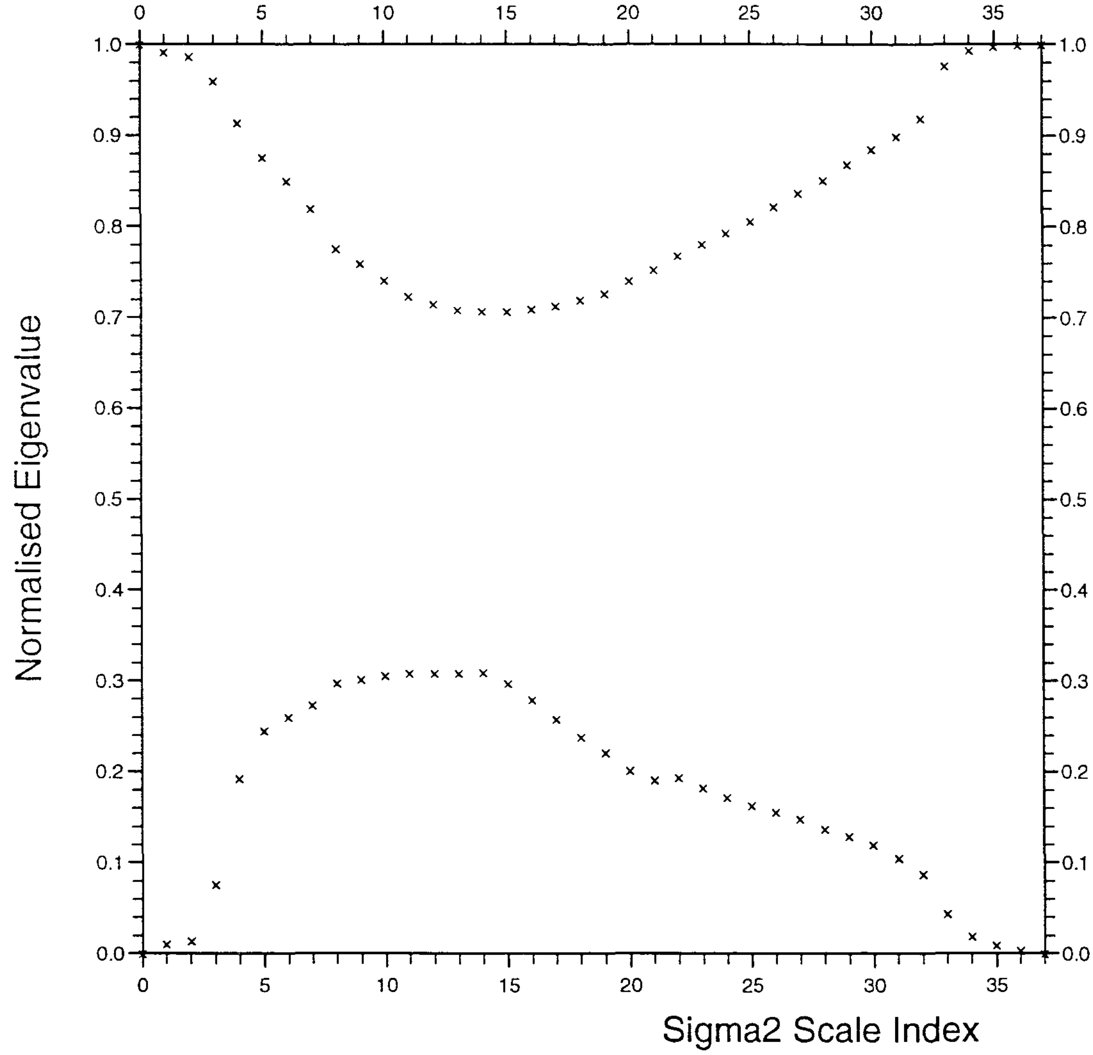

Figure 5.1: Eigenvalue structure of two-layer configuration. There is one degree of freedom (one separation level), represented by the x-axis which is σ_2 to a non-linear scale. Indices 0 (surface) and 37 (bottom) are the one-layer case, where $\lambda_2 = 0$. Indices 1 to 36 are the steps on the σ_2 scale down which the single separation level is scanned, where the steps occur at approximate depth increments of 100 m. The development of both eigenvalues (upper: λ_1 and lower: λ_2) is shown.

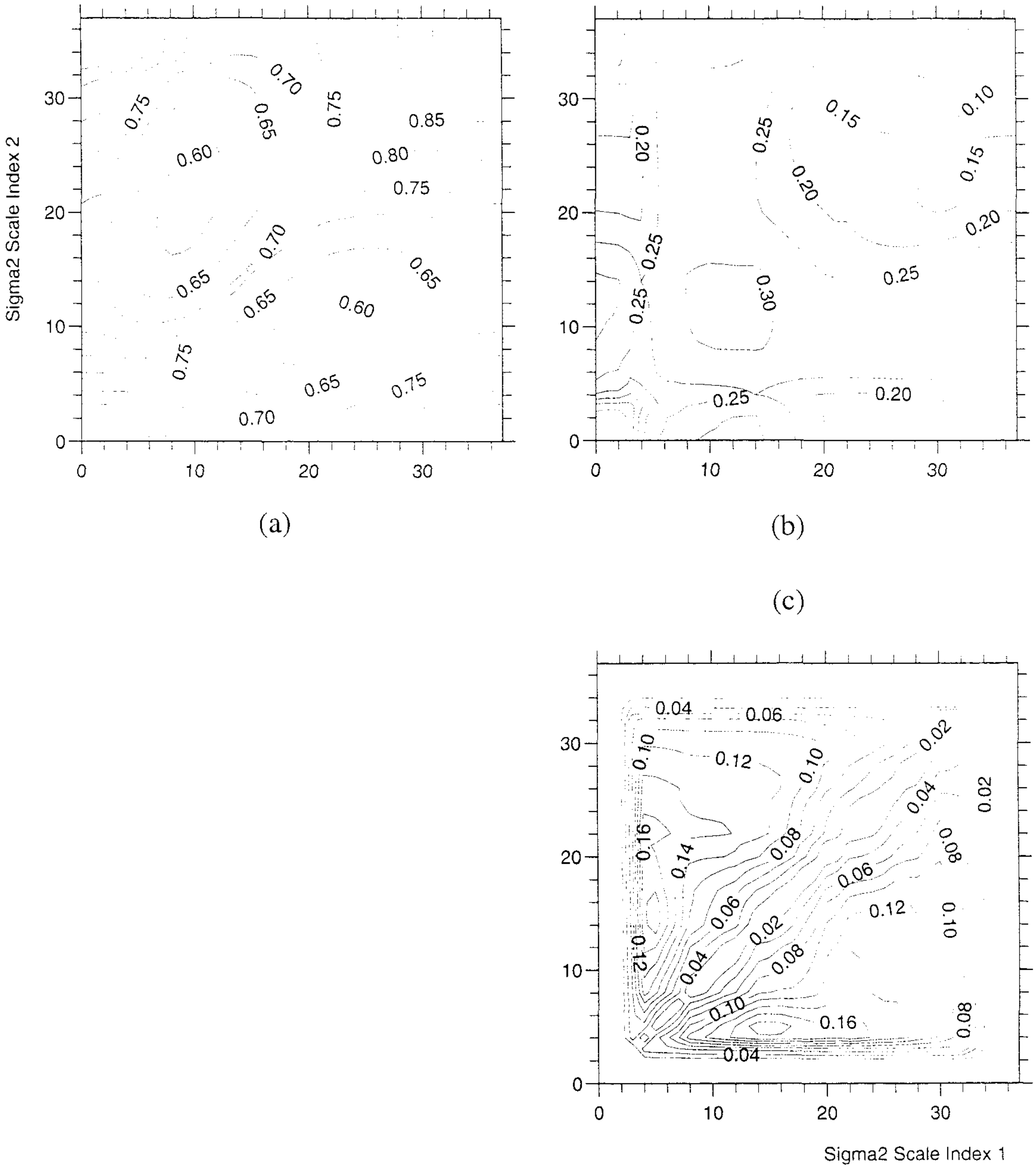

(a)

(b)

(c)

Figure 5.2: Eigenvalue structure of three-layer configuration. There are two degrees of freedom (two separation levels); the x and y axes are to the same non-linear σ_2 scale as in figure 5.1. All three eigenvalues are mapped, as (a), λ_1; (b), λ_2, and (c), λ_3. The figure is symmetric about the main diagonal because of the degenerate labelling of the two separation levels. The corners of each plot show the one-layer case (0,0), (0,37), etc, where $\lambda_2 = \lambda_3 = 0$. The sides show the two-layer case where λ_3 = 0. The optimum is seen at the maximum of λ_3 (5,15).

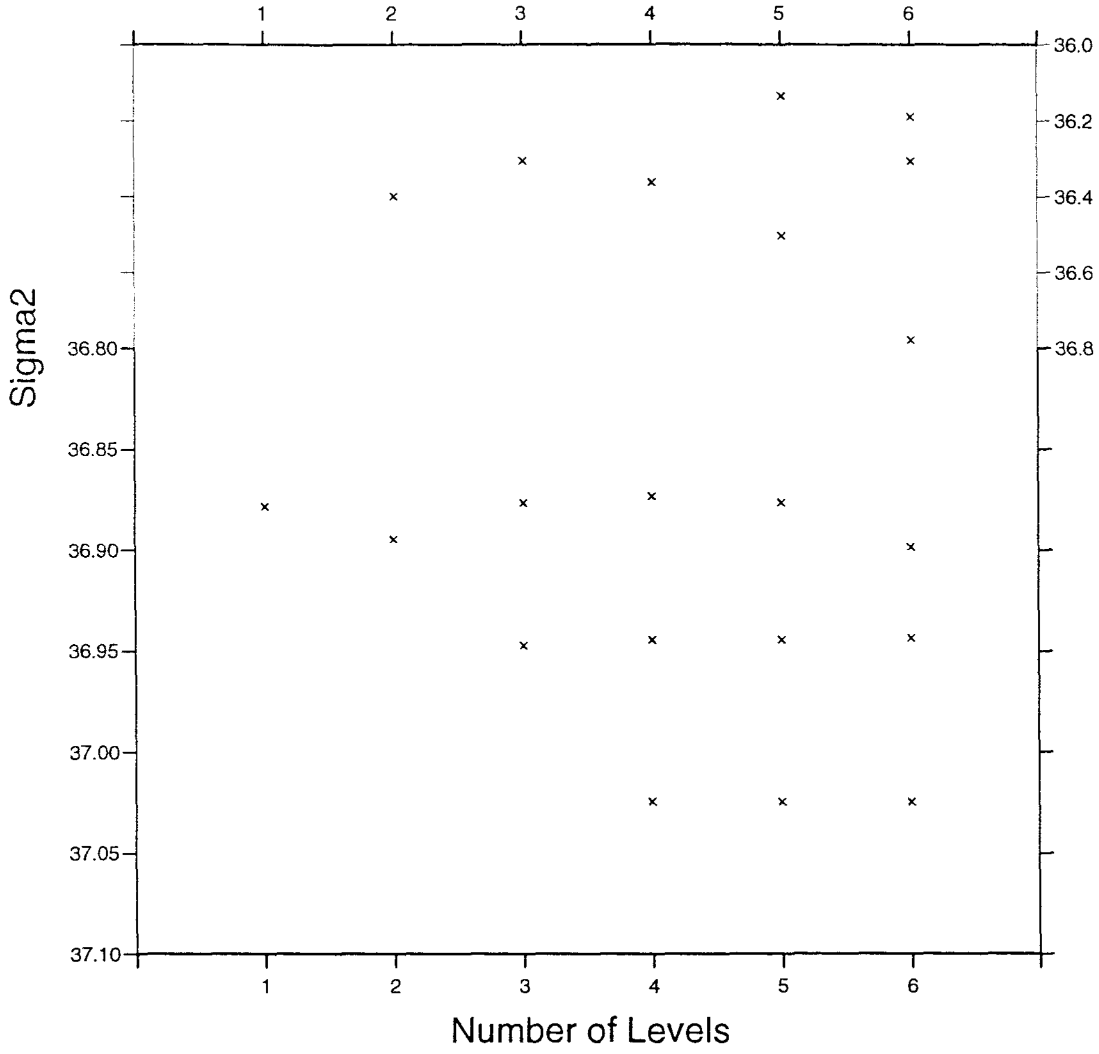

Figure 5.3: Optimal layer structure in σ_2 as a function of number of layers, for up to six separation levels (seven layers). Note the change of scale at $\sigma_2 = 36.8$.

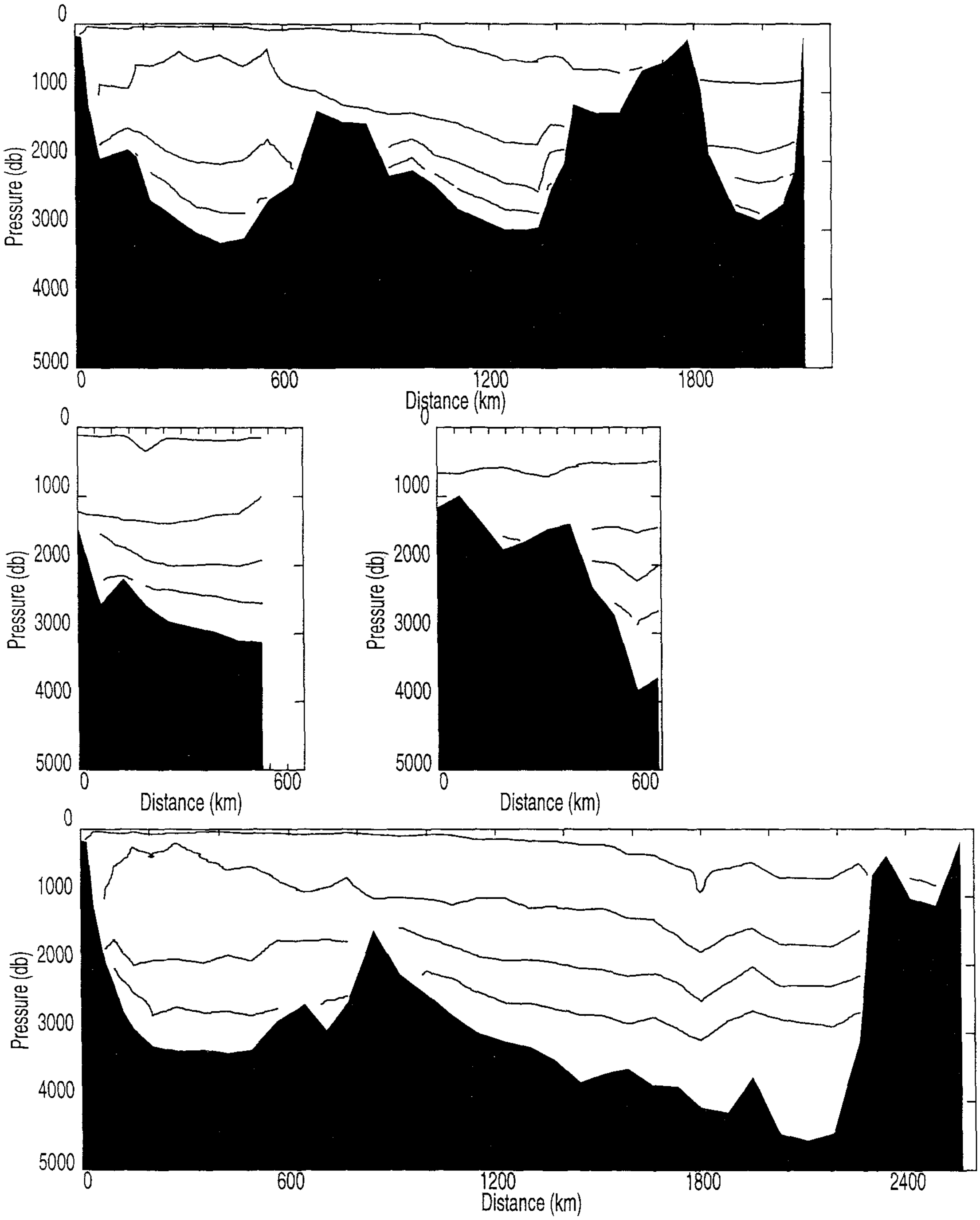

Figure 5.4: Density levels for the five-layer optimal configuration (σ_0=27.425, σ_2=36.873, 36.944, 37.024). The top and bottom panels are the north and south sections respectively, both with west to the left. The centre panels are the west (left) and east (right) sections, both with north to the left.

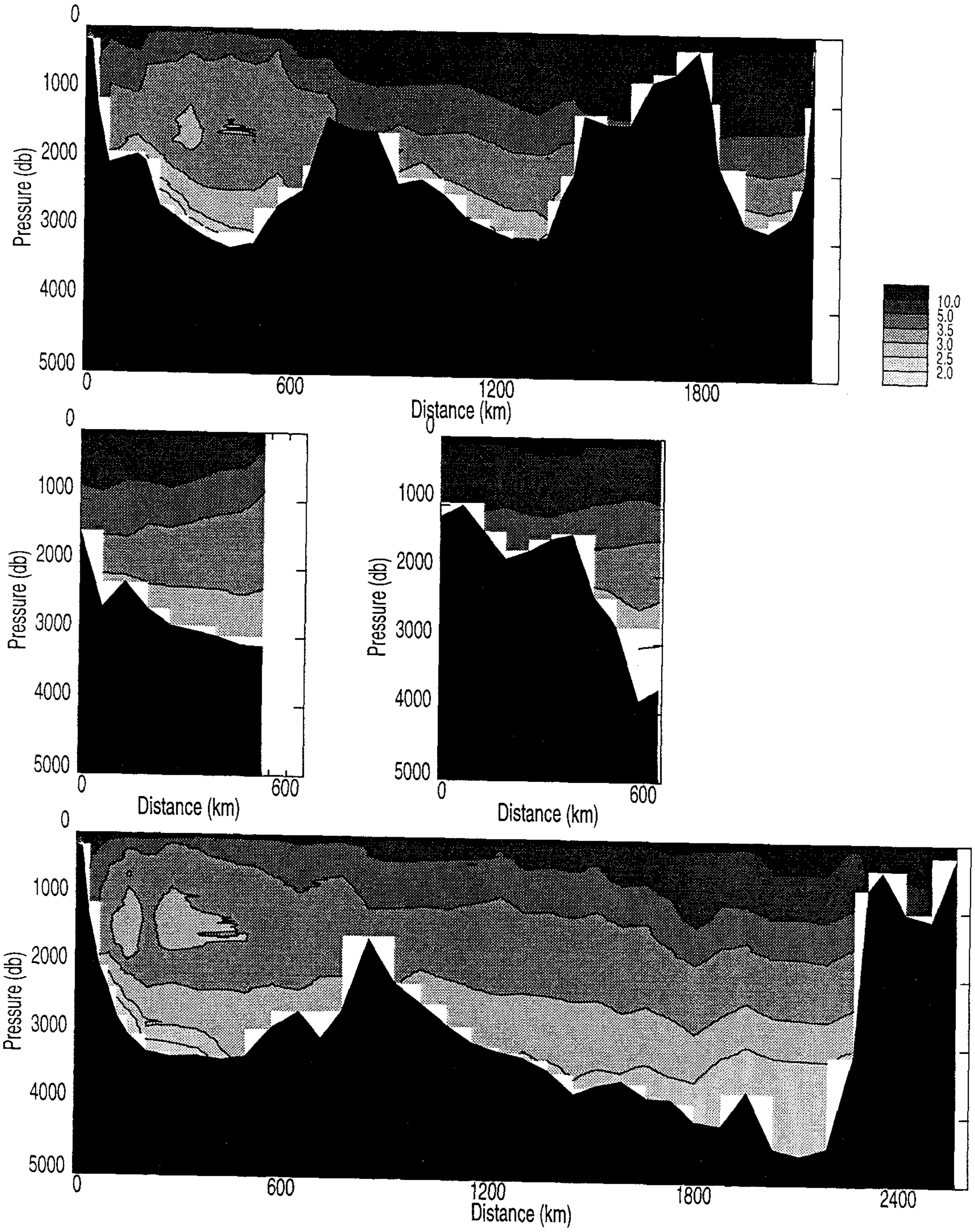

Figure 5.5: Potential temperature (θ); the sections are in the same order as in figure 5.4.

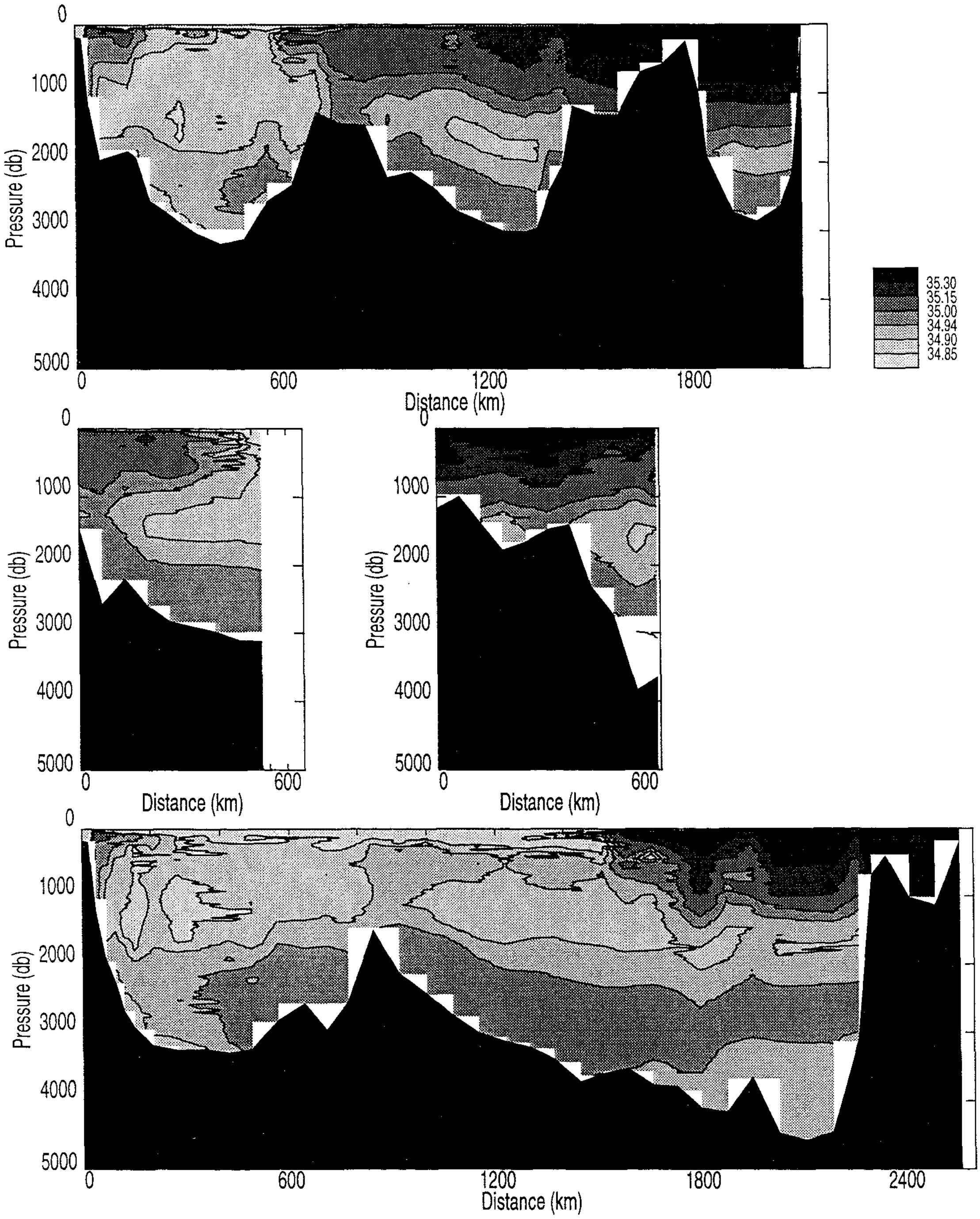

Figure 5.6: Salinity; the sections are in the same order as in figure 5.4.

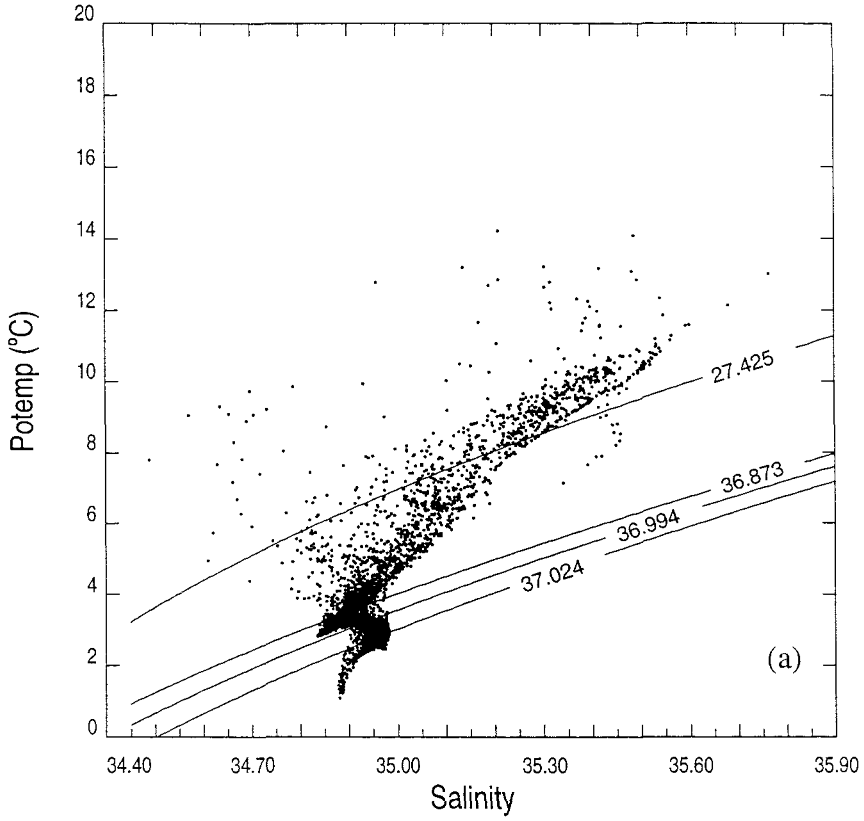

Figure 5.7 (a): θ–S plot of CONVEX and EGC data, omitting just the westernmost EGC data (where salinity goes below 30); points plotted are at 50 m depth intervals; and the optimal density levels are superimposed.

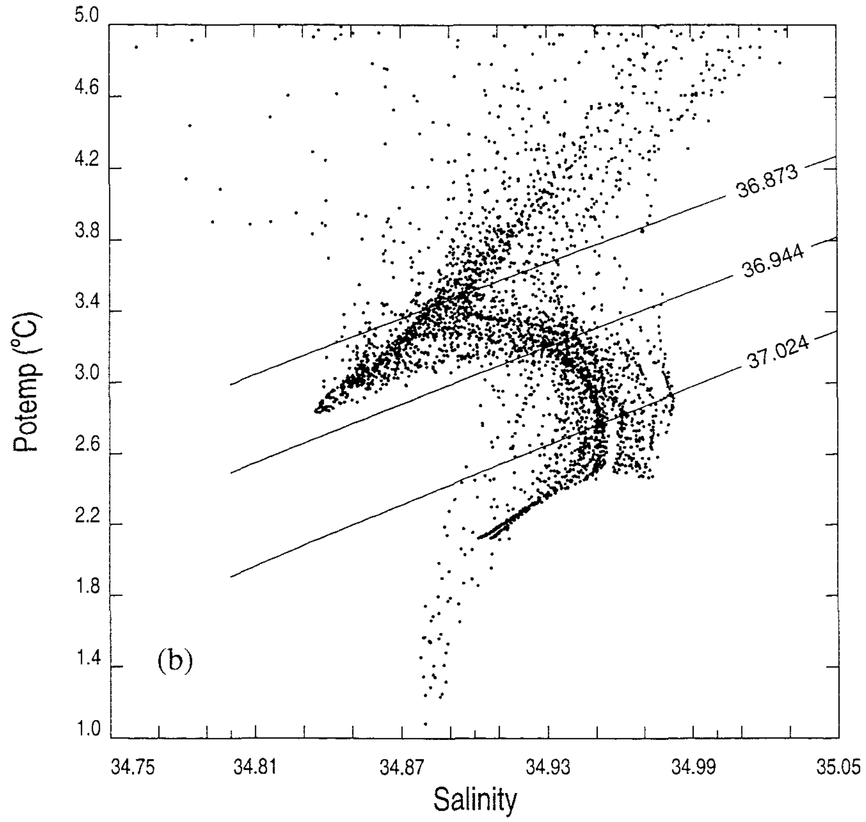

Figure 5.7 (b): θ–S plot of all CONVEX and EGC data, zooming in on the deeper water masses, and with the optimal density levels superimposed, one of which (σ_0=27.425) is now off-scale.

6. CIRCULATION AND FLUXES

In this section we consider some oceanography. We wish to estimate the net (polewards) fluxes of heat and salt across the CONVEX-91 region. This latter is then employed in developing an estimate for the Arctic freshwater gain. At the same time, we also produce a circulation scheme for the region. However, as net fluxes are much less sensitive to the details of circulation than the circulation itself, we have more confidence in the fluxes, for which we estimate errors, than in the circulation scheme. This is all discussed below. Before launching into the calculations, we must plug the gap between the westernmost CONVEX-91 stations and Greenland. Without such infill, we have no East Greenland Current, which is the local western boundary current, so we address this first.

6.1. Fabrication of East Greenland Current data

The first matter which must be addressed, in order that the effort to determine fluxes may progress, is that of the absence of the East Greenland Current (EGC) from the CONVEX data. Foul weather prevented work in the final 70 km of sections whose total length coast-to-coast was over 2500 km; the last westward station in the north section (48, on 17 August) and the subsequent first eastward station in the south section (49, on 19 August) were both just outside the EGC, by about 10-15 km. This was determined by examination of thermosalinograph data (not shown here), which shows the very sharp salinity front at the eastern edge of the EGC. However, we did manage to leave the area with some useful measurements of the EGC: during the two days between stations 48 and 49, and also for 20 hours between stations 47 and 48, the ship was mainly hove-to and collecting good ADCP data. In this section we will show that a reliable estimate of the geostrophic reference current can be made with these data, and that in combination with historical data to provide the vertical current shear, a useful (if hybrid) EGC can be included in this study. Also we will inspect the salt flux between the westernmost station and the beach, to see if the extreme salinities encountered near the coast are likely to have significant effects.

The logical choice of historical data was the part of the International Geophysical Year (IGY) Section 4 (Summer) made on the R/V *Anton Dohrn* in 1958 (Dietrich, 1969), because the tracks of the CONVEX south section and IGY section 4 are nearly coincident in the Irminger Basin. Accordingly, six IGY stations, numbers 2614–2619, were used; their positions, with CONVEX stations, detailed CONVEX ship track and bathymetry are shown in figure 6.1. It is intended to use the pairs 2614–2615 and 2615–2616 for comparison with CONVEX, and to use the geostrophic profiles and associated properties of the three pairs 2616-2619 to represent the EGC contiguously with the CONVEX sections.

We want to compare the IGY and CONVEX vertical current shears. We note first that there have been large changes in water properties. Figure 6.2 shows potential temperature and salinity at stations 49 and 2616, which are close together, and also their separation (~15 km) is in a direction parallel to the isobaths. A cooling and freshening of the water can be seen (cf. Read and Gould, 1992), the magnitudes of which greatly exceed the dominant measurement accuracy, which for IGY salinity was ca. 0.01, and for IGY temperature ca. 0.01°C. To proceed with the comparison, we need two pairs of stations; we take 49 and 2616 as 'matched'; the simplest way to produce a CONVEX 'station' matching 2615 is to average 50 and 51. Then geostrophic profiles were formed, referenced to 1000 m, for the IGY stations (2615 and 2616) and for the CONVEX stations (49 and "50-51"). The resulting profiles are shown in figure 6.3a, from which it can be seen that the vertical shears are remarkably similar above 1000 m; there is a considerable difference in shears below 1000 m, which we discuss later. Although properties have changed, the upper ocean horizontal density gradients have not. This comparison is repeated for CONVEX stations "50-51" and 52, and IGY stations 2614 and 2615; the resulting shear profiles are shown in figure 6.3b.

We will need estimates of these property changes for later use; they are shown in figure 6.4. The CONVEX data are colder (–0.58 °C) and fresher (–0.038 psu) than the IGY data, where the differences are calculated as averages above 1000 m.

We turn now to the ADCP data. Considering the ship's track as shown in figure 6.1, it can be seen that in wandering around while hove-to, the ship covered isobaths at depths of all but the innermost station pair (2618-2619); therefore we expect to extract estimates of reference currents for the mid (2617-2618) and outer (2616-2617) of the IGY geostrophic profiles. Since the shallower of these latter profiles terminates around 170 m depth, we will attempt to estimate the offset (ADCP minus geostrophic) current at a fixed depth; and since it was argued in B94 that rotational currents do not reach down during CONVEX as far as 100 m depth, we will use data at that depth to estimate reference currents. Figure 6.5 shows 15-minute mean absolute current vectors at 100 m depth for %good >50% and for ship speeds through the water less than 2.5 m s^{-1}, in the EGC area. It can be seen that the current is quite steady, with mean magnitude 30.9 cm s^{-1} (sd 11.5 cm s^{-1}) and direction 227° (sd 30°); the direction is nearly perpendicular to the sections. By comparing the three IGY profiles, referenced to zero at the bottom, with the above figure for the current at 100 m, we find offsets of 20 cm s^{-1} (inner), 29 cm s^{-1} (mid) and 15 cm s^{-1} (outer). We have assumed that the mean current value can be applied to the inner, shallowest station pair to derive the above offset, as well as the other two pairs whose bathymetry range is covered by the ADCP data. These values and assumptions are carried forward and examined later in this section.

Now we consider the inshore salt flux, between *Anton Dohrn* station 2619 and the beach. This will be a crude estimate because we have little data. We take the cross-sectional area between 2619 and the beach to be triangular such that the offshore depth is 170 m and the offshore distance is 20 km, resulting in an area of 1.7×10^6 m^2. We assume the currents to be barotropic and decreasing linearly from 40 cm/s at 2619 (westernmost mean current , from profile data) to zero at the beach; and we take a mean salinity profile from 2619, salinity ~ 32.5 psu (westernmost mean salinity, from profile data), from which the salinity anomaly (difference from section mean) is ca. –2.5 psu. Thus we estimate the inshore volume flux to be 0.45 Sv and the resulting salt flux to be 1.13 Svpsu. This is quite large. It is also probably an under-estimate, since as one approaches the beach, one approaches one of the sources of the freshening of the EGC, ie, glacial melt water run-off.

6.2. Reference state definition and sensitivity tests

In this section, we approach determination of heat and salt fluxes across the north and south sections (now understood to include the EGC data) after the manner of Bryden and Hall (1980). A reference state is defined, then its sensitivity to variations in its components is examined by allowing each of them to vary within a prescribed range, and inspecting the effect of the variations on the net heat and salt fluxes. Only one element is allowed to vary from the reference state for each run (unless stated otherwise). These variations are divided below into inverse sensitivity tests and oceanographic sensitivity tests, and the results of all tests are summarised in Table 6.2, which shows net fluxes of potential temperature and salt for both north and south sections.

Salt flux is computed using salinity anomaly, which is salinity minus transport-weighted section mean salinity. These section salinity means are 34.956 (south) and 34.999 (north). The flux differences ($\Delta\theta$ and ΔS) are the differences between each computed state and the reference state, for each section. The divergences are the differences (south minus north) between relevant flux values for each run. A positive value signifies loss, a negative value gain.

6.2.1 Reference state

1) EAST GREENLAND CURRENT.

Following the description in section 6.1 above, we take the IGY data representing the geostrophic velocity shear and adjust it with the reference currents derived from the in-situ ADCP data to form the EGC element of the reference state. We note that the standard error of the mean of the reference currents is rather too small to be taken seriously (1 cm s^{-1}), because the measurements are all very close together in time and space, which has the effect of making the number of independent measurements less than the number of actual measurements (see Challenor and Carter, 1994).

Accordingly we choose a range for the EGC reference currents of ±6 cm s^{-1}, the average of the standard deviation and the standard error of the mean. The total southward volume flux in these three station pairs is then 15.0 Sv, of which 4.2 Sv derive from the velocity shears referenced to zero at the bottom. The reference current range is equivalent to ±3.5 Sv. Potential temperatures and salinities are adjusted by constant offsets to bring the IGY values into line with the modern data. No significant differences resulted from replacing the mean offsets with vertically graduated ones reflecting the difference profiles in figure 6.4.

2) EKMAN FLUXES

Climatological values of wind stress due to Hellerman and Rosenstein (1983) are used to estimate the cross-track Ekman fluxes of volume, temperature and salt. As expected for a region of the northern hemisphere dominated by westerly winds, the Ekman fluxes are southwards and of magnitude 2.0 Sv (south section) and 1.0 Sv (north section), and these values are used as the Ekman flux elements of the reference state. The values of potential temperature and salinity at 10 m are chosen for determination of Ekman contributions to property fluxes. Their track-length-weighted mean values are, for potential temperature, 12.130 °C (south) and 12.249 °C (north); and for salinity, 34.884 (south) and 34.994 (north). The Ekman volume fluxes are allowed to vary by ±25%, approximately the range of the annual cycle.

3) GEOSTROPHIC BASE STATE

As can be seen in figure 3.1, there are three connected boxes of CTD stations. Note that the western box is closed across stations 48–49 and is not made to connect to Greenland. We first want to find a level of no motion for the geostrophic base state at which the net volume fluxes through each box are most nearly balanced to zero. We tried using pressure levels, but with no coherent result, so densities (σ_0 and σ_2) were used instead. The range of density levels which gave minimum net volume fluxes was from $\sigma_2 = 36.93$, for which there were net outflows from all three boxes of 1.3 Sv (west), 0.1 Sv (centre) and 2.5 Sv (east), to $\sigma_2 = 36.95$, for which there net outflows of 2.3 Sv (west) and 1.0 Sv (east), and an inflow of 1.9 Sv (centre). From the likely range of geostrophic base states and the optimal layers identified in section 3 above, we proceed to set up five inverse model states, the first of which contributes to the overall reference state and is described next.

4) INVERSION STATE 1.

All inverse models described below consist of constraints in the form of horizontal flux conservation equations written for each layer (layers as defined below) and for each box (west, centre and east); the conservation equations are coupled at the east and west sections. Unless stated otherwise, solution degree is selected using the method for comparing offsets (where the offset, defined as the ADCP minus base geostrophic current, is used as an estimate of the inversion solution vector; and is called $\mathbf{m}^{\mathrm{ADCP}}$) with inversion solutions ($\mathbf{m}^{\mathrm{est}}$) presented in B94, whereby the results of correlating $\mathbf{m}^{\mathrm{est}}$ with the solution estimate formed from the offset filtered by the model resolution matrix ($\mathbf{m}^{\mathrm{filt}}$), at all solution degrees, is examined. See chapter 3 also for details of the removal of the M2 tidal signal from the ADCP data. The (de-tided) offsets obtained for zero velocity at $\sigma_2 = 36.93$ are shown in figure 6.6.

State 1, which contributes to the reference state, is formed by starting with zero velocity at $\sigma_2 = 36.93$; the water column is divided into the five optimal layers identified in section 3; volume flux and salt flux conservation are required in all layers; temperature flux conservation is required in all layers except the top one: a total of 42 constraints results. Table 6.1 shows the statistics resulting from the correlations of $\mathbf{m}^{\mathrm{est}}$ with $\mathbf{m}^{\mathrm{filt}}$ (and $\mathbf{m}^{\mathrm{est}}$ with $\mathbf{m}^{\mathrm{ADCP}}$), from which can be seen high correlations ($r^2 > 0.8$, except degree 2) up to solution degree 6, and the last evidence of any correlation ($r^2 \sim 0.2$) at degree 8. We choose solution degree 6 (degree 8 makes little difference) for State 1; see figure 6.7.

5) NET VOLUME FLUX

The net volume flux across the north and south sections is fixed to zero. This value is examined more closely below. The flux excess in Table 6.2 is the volume flux which must be added to EGC, CONVEX and Ekman fluxes to return the net volume flux across each section to zero. In runs 1–11 (see Table 6.2), the excess is redistributed uniformly over the whole section. To illustrate the effect on currents, 1 Sv is equivalent to 0.027 cm s^{-1} spread over the whole south section. Note that for runs 1–11, the effect of the flux excess on the potential temperature flux is to transport a quantity equal to the transport-weighted section mean value of the potential temperature multiplied by the flux excess. The section mean potential temperatures are 4.033 °C (south) and 4.906 °C (north). Since we are working with salinity anomaly for the salt flux, the flux excess has no effect on the salt flux.

6) SUMMARY

The five elements described above combine to give a very near flux balance; the excess is about –1.5 Sv (we will argue below that this is probably fortuitous). The temperature and salt fluxes are about 56 Sv°C and 4.6 Svpsu, for both north and south sections.

6.2.2 Inversion sensitivity tests.

1) STATE 2

As the first variant on state 1, we replace the optimal set of layers with a pseudo-random set: sea surface, $\sigma_0 = 27.25, 27.45, 27.6$, $\sigma_2 = 36.8, 36.86, 36.9, 36.94, 37.0, 37.08$, bottom (10 layers). The same flux constraints as in State 1 are applied, from which a total of 87 constraints results. The solution degree is chosen by correlation at degree 11, where $r^2 > 0.8$.

2) STATE 3

As the second variant on state 1, we resume the configuration of five optimal layers, apply volume flux conservation constraints only, and require them to be exact, so solution degree 15 (out of 15) is selected.

3) STATES 4 AND 5

States 4 and 5 are arrived at in a manner identical to that of state 1, with the exception of starting with a different geostrophic base state: zero velocity is set at $\sigma_2 = 36.95$. A similar correlation structure to that shown for state 1 results, and solution degree 6 is chosen again and forms State 4. Also, there is a weak (and rather implausible) secondary correlation maximum at degree 35, which is selected as State 5.

4) STATE 0

This is the first geostrophic base state for both north and south sections, that is with zero velocity at $\sigma_2 = 36.93$ and no inversion.

5) SUMMARY

The above tests are in Table 6.2 as runs 2–6. Over both sections, the temperature flux range is 45–66 Sv°C (mean 54.3, sd 6.2); the salt flux range is 3.85–5.39 (mean 4.50, sd 0.45) Svpsu. All extrema result from State 2. There is no apparently significant difference between net fluxes at north and south sections. These different inverse models indicate an uncertainty of about ±10% in net fluxes due to choice of model.

6.2.3 Oceanographic sensitivity tests

1) EGC AND EKMAN FLUXES

The allowed ranges for the Ekman fluxes and the EGC have been mentioned above. The resulting fluxes are shown in Table 6.2 as runs 7–10, from which it can be seen that the total uncertainty in the potential temperature transport due to uncertainties in the EGC and in the Ekman flux is ±7%, for both sections. The Ekman salinities are little different from the section mean salinities, so the Ekman variations do not affect the salt fluxes; however, the EGC variations have a strong effect on the salt fluxes: ±8–12%.

2) DENMARK STRAIT OVERFLOW

All the above models, based as they are on the reference state, share the feature of clearly separating the surface–intensified EGC from the deep Denmark Strait Overflow (DSO) by a near-stationary LSW layer, resulting in a DSO flux of 3–4 Sv, which appears to be a considerable underestimate of its strength compared to the measurements made by Clarke (1984) in 1978, which were used by Dickson and Brown (1994) to derive a deep ($\sigma_0 > 27.8$) transport of 13.3 Sv southwards. In this section, using a detailed comparison of the current fields near Greenland as shown by

Clarke (his figure 6) with the reference state current field of CONVEX, we search for evidence which might justify increasing the CONVEX DSO transport, noting that in the approximate depth range of the core of the DSO (1800–3000 m), there is a barotropic offset (Clarke greater than CONVEX reference state) of 5–10 cm s^{-1}.

The topography in the depth range 1800–3000 m is resolved in CONVEX by four stations at depth increments of 300 m; therefore the 'bottom triangles' are equivalent to a strip 150 m above the bottom. Extrapolating the last common shear instead of the last common value of velocity gives an additional 0.5 Sv only, and so cannot be held responsible for any gross under-estimate. Therefore we *are* searching for possible missing barotropic flux: under-estimated reference currents, in other words.

By examining the ADCP offsets (figure 6.6) for station pairs in the western side of the Irminger Basin, we see in the westernmost two station pairs of both north and south sections, offsets whose average magnitude is 11 cm s^{-1} and which are coherent in direction. Now the mean offset is near zero (–0.8 cm s^{-1}), with sd large (8 cm s^{-1}); and in chapter 4 we showed that the background amplitude of ageostrophic transients was 5–8 cm s^{-1}, so these measurements are marginally significant. By using 11 cm s^{-1} (southwards) as additional reference current in station pairs 49-50 and 50-51 (south section), and 48-47 and 47-46 (north section), we obtain an extra southward flux of 12.5 Sv, of which 3.5 Sv goes below $\sigma_0 = 27.8$, giving a DSO now about 8 Sv. The net southward flux by Greenland (from the coast to about the centre of the Irminger Basin) is increased thereby from 20 Sv to 32.5 Sv, and we discuss these values in context below.

In terms of the circulation, it may be correct to increase the barotropic flows 100 km or so offshore of the EGC; but it is apparent that attempting to increase the DSO to 13 Sv would entail a massive increase in the circulation; so can we offer any evidence for the current being significantly less in our 1991 estimates than it was in Clarke's 1978 measurements? Consideration of figure 6.3 shows that by matching the remarkably similar upper shears of the CONVEX and IGY data, we see a large reduction between the earlier and later data of the deep shears; in figure 6.3a, demanding matched upper shears, the current at 2000 m is 10 cm s^{-1} lower in the CONVEX data; in figure 6.3b, there is a reduction at 2200 m of 3 cm s^{-1}, which increases by extrapolation due to the rapid divergence near the bottom of the two shears. Topographic resolution is restricted here by the IGY data.

By increasing the near–Greenland southward flow, as described above, an excess of over 14 Sv northwards in both north and south sections results. To compensate, this flux is redistributed as a constant adjustment across the sections. This is run 11 in Table 6.2.

We conclude this section by considering the consequences of reinstating the shear in the DSO. It is possible that we are seeing a change in the mean flow just subsequent to the observations reported in Dickson and Brown (1994), but it is more likely that we are observing one of the extremes in the current range. Referring to figure 6.3, we take the depth range of 1000 m above the bottom to be the reduced-shear area, the mean reduction in current to be 5 cm/s, and the width of the affected area to be 100 km, roughly the size of the current core in Dickson and Brown (1994), resulting in a required extra flux of 5 Sv southwards. We now try to compute the consequences for the heat flux of assuming that our observations are (a) quasi-synoptic, ie, temporarily in balance with zero net flux across the whole section, and (b) asynoptic, ie, temporarily out of balance, with a non-zero net flux across the whole section.

If we force an extra 5 Sv south in the DSO (where the mean temperature is 2.5 °C), we have an extra temperature flux of 12.5 Sv°C south. We then rebalance by distributing 5 Sv northwards over the whole section, which for the south section mean temperature of 4 °C results in a northward temperature flux of 20 Sv°C, giving 7.5 Sv°C northwards net extra flux. So the heat flux estimates developed here would be biased about 10% low.

Alternatively, still considering quasi-synoptic scenarios, we might replace local barotropic flux with the 'new' baroclinic flux. The local water-column mean temperature is not very different from the deep mean temperature, however (3 °C compared with 2.5 °C), so the resulting bias, while of the same sign, is reduced to 3%.

If our observations are asynoptic, then we should have a temporary net flux of 5 Sv northwards (ie, a temporary 'shortage' of 5 Sv southwards) on which we want to impose the extra 5 Sv southwards. The calculation is identical to the balanced case above and again we estimate a bias of 10% low in the present estimates.

We carry forward the estimates of bias as above, but retain our 'weak-shear' data for the purposes of flux calculation in the expectation of being able to compare our estimates with others in the future.

3) EXCESS IN NORTH ATLANTIC CURRENT

We consider now how best to place the flux excess generated by the DSO enhancement, which we repeat in this experiment. The normal process of applying a constant correction to both sections has the peculiar effect here of heating the ocean from the south section to the north. This is due to the geometry of the sections: because proportionately less of the north section than the south section is in the colder waters to the west, its mean temperature is higher. This shows that forcing the net flux to zero by applying a constant correction is wrong here, so the next most sensible thing to do is to apply the northward correction where the water is already going northward: in general, east of the MAR, or more particularly in the North Atlantic Current (NAC). This is clearly defined in the south section by the front in salinity at about 1500 km, figure 5.6. Complicated topography and lateral speading of the salinity signal in the north section make the application of this process less clear-cut there. However, we do not wish to allow through-flow in the Rockall Trough, which is a deep cul-de-sac. The Irminger Basin is the wrong place for it, because extra northgoing flux to the west side annuls the DSO enhancement, and if it is put on the east side, the south-going Iceland-Scotland overflow (ISO) is rapidly over-enhanced. Placing any of it in the west side of the Iceland Basin causes the ISO to disappear, which leaves the east side of the Iceland Basin; particularly, the relatively steep western side of the Rockall-Hatton Plateau. This is masked, or at least confused, by a large eddy; but the density structure (figure 5.3) indicates the possibility of a slope current there, and the ADCP data can be interpreted (figure 6.6) as showing an enhanced current next to an anticyclonic eddy (roughly stations 25 to 20; also, the presence of the eddy is confirmed by tracers). By enhanced we mean a non-zero (net northwards) current at what was the level of no motion in the LSW. More convincingly than our Doppler data, van Aken and de Boer (1995) have current meter data from the previous year (1990) in nearly the same place and depth range, which show a north-east going current of magnitude about 5 cm s^{-1}, similar to the adjustment of 3 cm s^{-1} northwards which we impose here over 5 station pairs (stations 27 to 83). This is run 12 in Table 6.2.

4) INTERMEDIATE

By trying to strengthen the DSO, we have been forced to increase the strength of the general circulation (of the NAC and the sub-Polar gyre). We discuss in more detail in section 7 on circulation the reasons for the most extreme variant of this increase to be hardly acceptable, but for now we state that this run (run 13 in Table 6.2) is useful as having the western boundary flux intermediate between the reference state and runs 11 and 12 above; the distribution of the return flow is the same as in run 12 above.

5) SUMMARY

Although it is rather alarming that the strength of the sub-polar circulation can be increased by up to 50% through modest adjustments to just two station pairs, we believe that the final state described above (run 13), in which the reference state is modified by intermediate enhancement of the Denmark Strait Overflow with consequent enhancement of the North Atlantic Current, represents our best estimate of the circulation, and contributes a basic adjustment to the net property fluxes of the reference state, which are increased by about 20%. However, the net fluxes are less sensitive than the overall circulation to such changes. The DSO enhancement alone increases the temperature flux to 65 (south section) and 74 (north section) Sv°C, from 56 Sv°C (reference state). Placing the flux excess entirely in the NAC increases these values to 74 (south section) and 78 (north section) Sv°C, which is not far off balance; this probably represents an upper limit to the temperature flux, with the forcing of the warmest part of the circulation. In the Intermediate state, both net fluxes are close to balance in both sections: 65.7 and 68.5 Sv°C for temperature; 5.49 and 5.39 Svpsu for salt.

6.3. Errors and fluxes

For the reasons set out above, we believe that modification of the reference state by the enhanced DSO is correct. Furthermore, concentrating the flux excess in the NAC produces either a maximum or maybe an overestimate of fluxes. Consideration of the details of the resulting circulation implies that the increase in the strength of the general circulation is untenable, so we select mean flux values from the Intermediate case, run 13 in Table 6.2, with no apparent significant difference between north and south section fluxes: 67 Sv°C for temperature, and 5.4 Svpsu for salt. We take as extremes therefore the reference state (run 1, minimum) and run 12 (maximum) from which we have a 'subjective' error range of ±7 Sv°C (10%) and ±0.8 Svpsu (15%).

The errors found in the other (deterministic) sensitivity tests above total 17% for temperature flux and 18–22% for salt flux, so the total errors are 27% and 33–37% respectively. We shall use 30% for both, so the salt flux across the section, and total error, is 5.4 ± 1.6 Svpsu. To this value must be added the inshore salt flux estimated previously, 1.1 Svpsu, giving a total salt flux of 6.5 Svpsu. We have no information with which to modify the error estimate. This value is examined in context in the following section.

Next, heat. Since these tests were carried out around a fixed zero net flux, in no case are we transporting the zero of the temperature scale; so the potential temperature flux is a true heat flux, and we may convert to heat units. We take a mean surface value of specific heat capacity c_p (Gill, 1982, table A3.1) of 3987 J kg^{-1} (sd of surface values 3 J kg^{-1}), and a mean in-situ density calculated from the data of 1034.5 kg m^{-3} (sd 4.5 kg m^{-3}) to give 1 PW = 242 Sv°C, where the error in the conversion factor may be estimated from the two sd's as 0.6%. The heat transport between Cape Farewell and Ireland as derived directly from the data is then poleward and equal to 0.28 ± 0.08 PW. We are unable conclusively to tell whether the possible 10% low bias (due to the weak DSO) is real, but if it is, the heat flux should then be 0.31 PW. There is no discernible significant difference between north and south section transports. These values compare very favourably with the Isemer *et al.* (1987) reanalysis of the Bunker heat fluxes, and they are discussed in this context in section 7.1.

We also note that Saunders and King (1995b) find the northward heat flux at the south end of the South Atlantic across WOCE leg A11 (approximately 45°S) to be about 0.5 PW northwards; in conjunction with the result reported here, that the heat flux at the northern end of the North Atlantic is about 0.3 PW northwards, we can therefore say that the Atlantic Ocean as a whole suffers a net loss of heat at about 0.2 PW.

The most cogent previous attempt at estimation of heat transport across the sub-polar gyre is that due to McCartney and Talley (1984); however, we have to make some calculations from their data in order to cast their results in a form comparable with ours. Firstly, they have a three-box model (their figure 5); we are only interested in two of these, representing upper and lower layers in the sub-polar North Atlantic, south of the Greenland–Scotland ridge and north of 50°N. From the temperature and volume flux values in their Table 2, we calculate values of net temperature flux across 50°N which fall into two groups, one 128 (±1) Sv°C (their basic setup), the other 159 Sv°C, which is forced with a high ocean-atmosphere heat flux in the Norwegian Sea. Then in their box model, the difference between the CONVEX fluxes (taken as representative of conditions at the north ends of their two southern boxes) and their 50°N fluxes is given by the heat lost by the ocean to the atmosphere over the sub-polar North Atlantic (their Q_{SPNA}), for which they quote an unpublished value due to Bunker of 87 Sv°C. Thus we find values of about 40 and 72 Sv°C (0.17 and 0.30 PW) for their net heat flux across the CONVEX region, which when compared with the CONVEX heat flux of 0.28 PW implies that the high ocean-atmosphere heat flux case is appropriate here.

6.4 Freshwater flux

Having obtained a modern estimate for the salt flux between Cape Farewell and Ireland, we now proceed in the manner of Hall and Bryden (1982) to examine the freshwater budget of the Arctic basin, and to comment on the estimates of Aagaard and Carmack (1989; AC89 below). It still seems odd to attempt to estimate a freshwater flux; that is to estimate the direct input of pure water to the ocean by evaporation, precipitation, runoff and ice melt, by examining ocean data with a method which can only *measure* net volume fluxes to within a few Sv, and then to attempt to derive a freshwater flux of fractions of a Sv. We convince ourselves with a simple illustration. Imagine two parallel sections across an ocean. Across one there is a net volume flux of 1 Sv at a mean salinity of 35. Between the two there is an input of 0.01 Sv freshwater. There is therefore a total volume flux across the second section of 1.01 Sv, and it must be at a mean salinity of 35/1.01 = 34.653. One may contemplate making oceanic freshwater flux estimates because of the high modern accuracy of salinity measurements, which enable one to measure the effect of the dilution of salinity by even a small amount of freshwater. Running the above example backwards, if one applies a (harsh) standard of accuracy of ±0.01 to salinity measurements, that enables freshwater flux determination to an accuracy (in principle) of ±0.0003 Sv. Plainly the restriction on the accuracy of freshwater flux estimation is not the accuracy of salinity measurement but the accuracy of the estimation of volume fluxes (of saline ocean water) at crucial choke points.

There are three areas where oceanic water can enter or leave the Arctic: through the Bering Strait, where the transport has been reported by Coachman and Aagaard (1989); through the Canadian Archipelago, reported by Fissel *et al.* (1988); and between Greenland and Europe, as ice as well as water, which we discuss below. Firstly we mention the large terms, as reported in the above sources: the Bering Strait inflow to the Arctic is about 1 Sv, the Canadian Archipelago throughflow exports water from the Arctic at about 1–2 Sv, therefore the net flow between Greenland and Europe must be small: probably 0 ± 1 Sv. Therefore the preceding conclusions about heat flux are not significantly affected by our assumption of zero net flux across the north and south sections. Now we continue in greater detail.

Consider the Arctic salt and water budgets. Following AC89, we identify the significant elements in the budget. These are: (i) the Bering Strait inflow T_B (0.8 Sv, ±25%) at salinity S_B (32.5); (ii) Atlantic (south section) net flux T_A at salinity S_A (34.956), where T_A is unknown; (iii) Atlantic (south section) salt flux C (6.5 ± 1.6 Svpsu) for zero net volume flux; (iv) Canadian Archipelago throughflow, T_C at salinity S_C, discussed below; (v) Ice export through the Denmark Strait I; and (vi) Arctic freshwater input F. Then we can write volume flux (6.1) and salt flux (6.2):

$$T_A + T_B + T_C + I + F = 0 \tag{6.1}$$

$$S_A T_A + S_B T_B + S_C T_C + C = 0 \tag{6.2}$$

Considering the Canadian Archipelago thoughflow, we use the Fissel *et al.* (1988) transport of 1.7 Sv south with the Aagaard and Greisman (1975) mean salinity of 34.2 (in the same way as AC89). Ice export in the EGC we estimate by taking the value reported in AC89 for export through the Denmark Strait (560 km^3 yr^{-1}, or 0.018 Sv), and then estimating the reduction in width between Denmark Strait and Cape Farewell of the East Greenland ice extent from Gloersen *et al.* (1992); this is about 40% on an annual basis, leaving ice export off Cape Farewell about 0.007 Sv.

From these we obtain a freshwater gain for the Arctic of 0.17 Sv and a net northward flux across the CONVEX region of 0.73 Sv. If one suspects the Canadian Archipelago throughflow to be too high, then performing the calculation again but with $T_C = 0$ reduces the freshwater gain to 0.14 Sv and reverses the mean Atlantic flux (T_A is 0.97 Sv southwards), so overestimating T_C biases the freshwater gain high.

One may calculate from AC89 the Arctic freshwater gain both by oceanic budgeting (as above) and by their direct estimation of evaporation, precipitation etc.

The former results in a gain of 0.11 Sv (Bering Strait input, Canadian Archipelago export, Denmark Strait ice export, Atlantic water exchange); the latter in a gain of 0.20 Sv (Arctic and GIN sea precipitation minus evaporation, and runoff, and input from the Skaggerak). The direct estimate is similar to that obtained from Baumgartner and Reichel (1975); integrating their data from Bering Strait to 55°N in the Atlantic, one finds a gain of 0.22 Sv. Thus the present estimate of Arctic freshwater gain (0.17 Sv, depending principally on one's belief in values for T_B and T_C) tends towards a value closer to AC89's direct than indirect estimates. The calculation is controlled mainly by C and T_B because S_C is not too dissimilar from S_A.

6.5 Circulation

We conclude with a description of the sub-polar circulation resulting from the calculations above. Note that all flux figures, numbers 6.8–6.11, show fluxes accumulated from west to east.

The circulation of the preferred state (Intermediate: run 13, with enhanced DSO and NAC) will be described, while the states considered as extrema (run 1, the reference state and 'minimum', and run 12, the 'maximum') will be referred to in terms of consequential alterations to inferred flow patterns. Depth-integrated fluxes of volume, potential temperature and salinity are shown for the north section in figure 6.8 and for the south section in figure 6.9; Ekman fluxes and volume fluxes by layer are shown in figures 6.10–6.11. Figure 6.12 shows horizontally-integrated fluxes by layer. The circulation is assembled by considering three parts: upper, from the sum of layers 1 and 2; mid-depth or LSW from layer 3; and deep, from the sum of layers 4 and 5. Figure 6.13 shows sketches of each layer's inferred circulation.

6.5.1 General circulation strength.

The strength of the general circulation of the sub–Polar gyre is deduced from the depth–integrated flux between Cape Farewell and the centre of the Irminger Basin, which we suggest is the best place to do so because the entire (southward) flow, comprising the EGC (the western boundary current) and the DSO (the deep western boundary current, DWBC), is concentrated there and distinctly separated from the more complicated flows to the south and east. We note that Reid (1994) places over 30 Sv there, and Clarke's (1984) measurements show 33.5 Sv, with an alternative of 27 Sv. Schmitz and McCartney's (1993) circulation appears to total 36 Sv (7 Sv greater than 7°C, 14 Sv between 4 and 7°C, 15 Sv below 4°C). Our preferred scheme has 26–27 Sv there, with weak and strong alternatives at 20 and 33 Sv. We emphasise again that this range is caused solely by uncertainty in barotropic flows in just two station pairs which lie immediately east of the front between the EGC and the more saline Irminger Current.

The northward flow on the east side of the North Atlantic is noisier (more eddies) and more wide-spread. On the south section, it is still clearly separated from the southward flow, and is seen between about 25°W and the European continental shelf. On the north section it avoids the Rockall Trough and is squeezed onto the west side of the Rockall–Hatton Plateau, where the flow is complicated by a large eddy and evidence of recirculation. We see three eddies in the northward flow, all well-sampled by the survey, of which two are on the south section and of depth-integrated amplitude 10 and 15 Sv, and one very broad one on the north section of amplitude 10 Sv. All are anticyclonic, and their approximate positions and sizes are shown on the sketch of upper circulation.

We note also that the total salt flux is divided roughly equally between south-going fresh water in the west and north-going saline water in the east; and that nearly one-third of the total occurs in the westernmost station pair of the EGC, which is shallow (less that 200 m), transports about 1 Sv, and has the most extreme salinity of the section, reaching values less than 30 psu. When the inshore salt flux is included (section 2), 2.7 out of 6.5 Svpsu (over 40% of the section total) are transported on the Greenland shelf, and this is 45% of the inferred freshwater gain of the Arctic.

6.5.2 Upper layer flows.

See figure 6.13a. The upper circulation (layer 1 plus layer 2) has 18 (±3, from the alternatives) Sv southgoing in the west. The northgoing flow in the south section we subdivide on the salinity front at about 25°W, calling the flow to the east the NAC proper, which has a magnitude of 19 Sv, and the flow to the west, which is weaker and more widespread, recirculating elements of the sub-Polar gyre, which has a magnitude of 6 Sv. Saunders (1982) has an upper (shallower than 1100 m) transport of 18 Sv northward across 53°N between the European shelf edge and the MAR, which compares favourably with the above. The upper layer net flux is 7 Sv northwards (which is not affected by barotropic adjustments). The magnitude of the Irminger Current (the northward flow west of the MAR) we estimate at 9 Sv at about 59° N, which compares favourably with the Krauss (1995) estimate of 9.6 Sv at 62° N.

6.5.3 Mid-layer (LSW) flows.

See figure 6.13b. There is a concentrated southward flow of 3 Sv in the west partially balanced by a very broad northward return flow of 2 Sv east of the MAR. The southward flow is another direct consequence of the addition of the barotropic component to the westernmost 2 CONVEX pairs on the north and south sections. The presence of the northward flow is supported in general terms by inference from tracers as in Talley and McCartney (1982) and by the analytical study of Cunningham and Haine (1995). The net flow in this layer is 1 Sv southwards. The minimum circulation has near zero fluxes in this layer; the maximum circulation has stronger (5 Sv) southward flow, but similar northward return flows.

6.5.4 Deep flows.

See figure 6.13c. Firstly we note that the top of layer 4 ($\sigma_2 = 36.944$) is nearly exactly coincident with Dickson and Brown's (1994) use of $\sigma_0 = 27.8$ to delineate the division between the DWBC and overlying waters. We apparently find from our data a gross reduction in DSO transport over previous estimates, as mentioned above; our preferred transport is 5.5 (±1.5) Sv. For each 1 Sv we put into the DSO by manual adjustment of barotropic flows, the general circulation is increased by an additional 4 Sv, so trying to increase the DSO from 4 (reference state) to 12 Sv would mean increasing the general circulation from 20 Sv (reference state) to 60 Sv, which is ridiculous. The 12 Sv DSO is untenable.

The patterns of the deep flows are well known (eg, Dickson et al., 1990); there is the southgoing DSO in the west, supplemented by some of the ISOW which, having travelled south down the east side of the MAR, turns in part through the Charlie-Gibbs Fracture Zone, runs north up the west side of the ridge then south along the Greenland shelf edge, and, in overlying the DSO, supplements the DWBC. The elements of our deep flows which are consistently quantified by the three schemes under consideration are the DSO (as above); the northward flow on the west flank of the MAR at about 1.5 Sv on both sections, which is reasonable when compared with Saunders' (1994) long-term mean of 2.0 Sv Charlie-Gibbs throughflow; and the southward flow on the east flank of the MAR, which is 3 Sv on the north section, 5 Sv on the south section. Problems of deep flow balance arise when we attempt to amplify the DSO. Although the reference state deep flows are weak, they are balanced; now the topographic asymmetry of the north and south sections means that, in placing the northgoing flux excess in the NAC, the deep flows are easily unbalanced. Basin-wide net northward flows must go into the eastern basin, which is fine on the south section; we find a deep cyclonic recirculation there of about 2 Sv in consequence; but the north section is more sensitive. Where is a net northward flow to go? Not over the MAR, where it either amplifies the northgoing overflow on the west side and unbalances it with respect to the south section, or it wipes out the overflow on the east side. Not in the Rockall Trough, which is a cul-de-sac; which leaves the east side of the Iceland Basin (the west side of the Rockall-Hatton Plateau). The particular location can be further resolved by matching net north and south section fluxes of temperature and salt. But by increasing the barotropic flows there, the deep flow is also increased; and if the flux excess is increased past the present maximum case, then the northgoing flow is greater than the southgoing overflow on the west side of the basin. Therefore our Intermediate case, which is seen to be a compromise between conflicting requirements, has to the east of the MAR a northgoing input of 4 Sv under the NAC, of which 2 Sv recirculates to join the ISO, which in turn becomes a flow of 5 Sv, of which 1.5 Sv passes through the Charlie-Gibbs Fracture zone and the remaining 3.5 Sv either recirculates in the eastern basin or goes elsewhere in the western basin. 2 Sv are left to proceed northwards up the west side of the Rockall-Hatton Plateau, which is a large figure, if it all joins the ISO, which is thereby set at only 1 Sv. The net deep flux is 5 Sv southwards.

6.5.5 Summary

We believe that on the grounds of the sensitivity of the general circulation to barotropic adjustment, we have described two oceanic states which represent likely circulatory extrema, and an intermediate state which is close to a description of the actual circulation. We note that although details of the circulation can be altered considerably, the relative size of the effect of the alteration on net fluxes is much less than the size of the alteration relative to the original state, so that we are confident that the net fluxes and associated error bounds are correct, even if the circulation scheme may be open to criticism.

We conclude with a total flux balance of zero Sv, comprised of 7 Sv north (upper), 1 Sv south (LSW), 5 Sv south (deep), and 1 Sv south (Ekman).

Table 6.1: Inverse solution correlation statistics. Shown here are the correlations for inverse solution ($\mathbf{m}^{est}$) degrees 1 to 10 with the ADCP-derived solution estimate ($\mathbf{m}^{ADCP}$) and with $\mathbf{m}^{ADCP}$ filtered by the inversion model resolution matrix at the relevant solution degree ($\mathbf{m}^{filt}$). All remaining solution degrees (11-42) are insignificant. This inversion solution is referred to in the text as State 1.

Degree	r^2 ($\mathbf{m}^{ADCP}$–$\mathbf{m}^{est}$)	r^2 ($\mathbf{m}^{filt}$–$\mathbf{m}^{est}$)
1	0.170	1.000
2	0.127	0.421
3	-0.009	0.936
4	0.324	0.869
5	0.319	0.859
6	0.341	0.861
7	0.199	0.283
8	0.169	0.236
9	0.089	-0.067
10	-0.016	-0.264

Table 6.2: Net fluxes. Salt fluxes (S flux) and potential temperature fluxes (θ flux) are presented for two sections, North and South, for a reference state (State 1) and 12 variants, described in the text. The flux excess is the flux required to be imposed to force the relevant state to the imposed zero net volume flux (positive northwards). The flux differences (ΔS and $\Delta\theta$) are the differences between the variants and the respective reference states. The divergences (θ div and S div) are the differences between the South and North section net fluxes for each of the eleven states.

		South Section					**North Section**					**Divergences**	
Run	Description	Excess	θ flux	Δθ	S flux	ΔS	Excess	θ flux	Δθ	S flux	ΔS	θ div	S div
		Sv	Sv°C	Sv°C	Svpsu	Svpsu	Sv	Sv°C	Sv°C	Svpsu	Svpsu	Sv°C	Svpsu
	Reference:												
1	State 1	1.81	56.4	0.0	4.61	0.00	1.35	55.1	0.0	4.58	0.00	1.3	0.03
	Inverse sensitivity tests:												
2	State 0	5.21	57.7	1.3	4.63	0.02	0.26	53.6	–1.5	4.49	–0.09	4.1	0.14
3	State 2	1.65	66.2	9.8	5.39	0.78	4.07	45.2	–9.9	3.85	–0.73	21.0	1.54
4	State 3	–3.33	49.4	–7.0	4.05	–0.56	–4.38	58.4	3.3	4.99	0.41	–9.0	–0.94
5	State 4	0.69	55.0	–1.4	4.43	–0.18	0.26	53.5	–1.6	4.48	–0.10	1.5	–0.05
6	State 5	9.62	46.9	–9.5	4.15	–0.46	8.57	57.3	2.2	4.56	–0.02	–10.4	–0.41
	Oceanographic sensitivity tests:												
7	Low EGC	–1.77	57.8	1.4	4.25	–0.36	–2.24	53.3	–1.8	4.08	–0.50	4.5	0.17
8	High EGC	5.39	55.0	–1.4	4.96	0.35	4.93	56.8	1.7	5.09	0.51	–1.8	–0.13
9	Low Ekman	1.30	54.4	–2.0	4.61	0.00	1.10	53.8	–1.3	4.58	0.00	0.6	0.03
10	High Ekman	2.32	58.5	2.1	4.61	0.00	1.60	56.3	1.2	4.58	0.00	2.2	0.03
11	Enhanced DSO	14.38	64.6	8.2	5.36	0.75	15.77	74.0	18.9	5.88	1.30	–9.4	–0.52
12	Excess in NAC	14.38	73.9	17.5	6.26	1.65	15.77	78.7	23.6	6.07	1.49	–4.8	0.19
13	Intermediate	8.10	65.7	9.3	5.49	0.88	7.00	68.4	13.3	5.39	0.81	–2.7	0.10

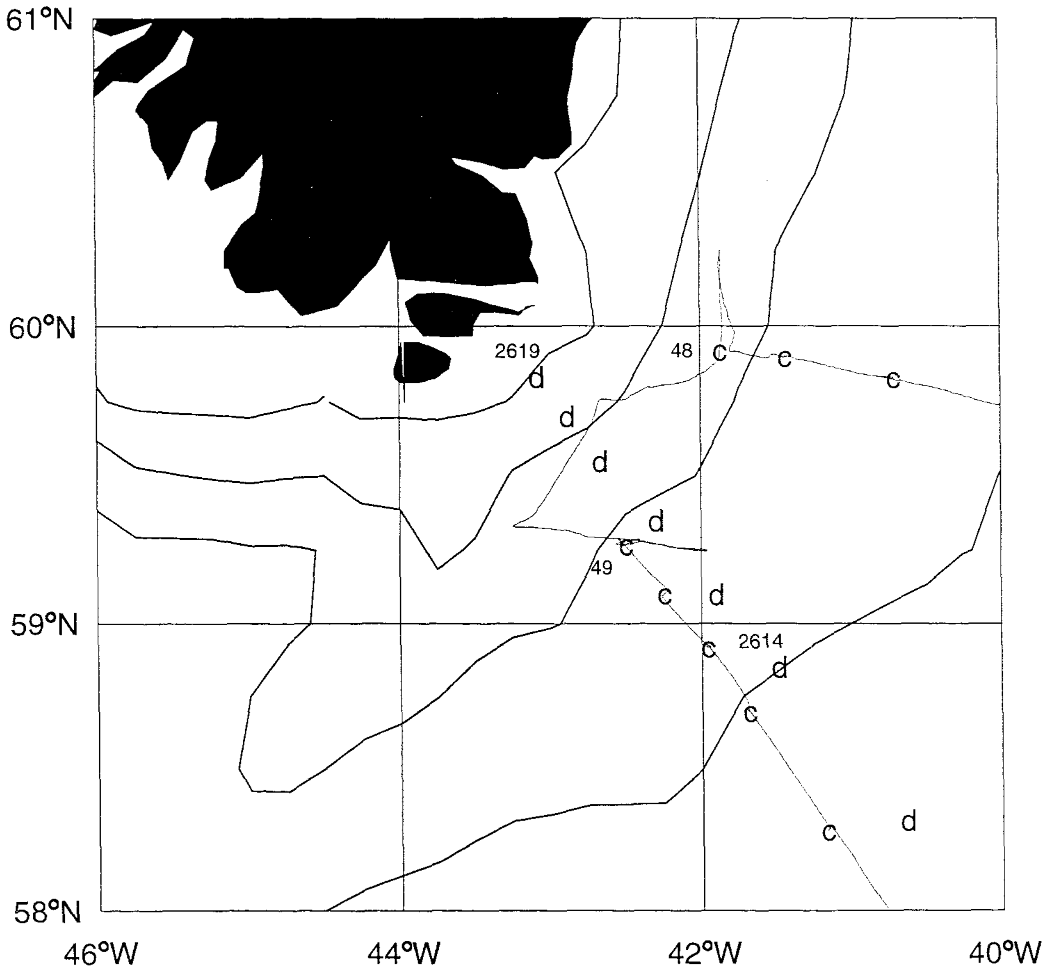

Figure 6.1: Magnified view of western end of CONVEX area. Letter 'c' indicates CONVEX station positions (as figure 1), letter 'd' indicates R/V *Anton Dohrn* station positions. The six of these latter employed in the text are numbers 2614 (south-eastern) to 2619 (north-western). The continuous line joining the CONVEX stations is the track of the RRS *Charles Darwin*. Depth contours shown are 200, 1000, 2000 and 3000 m.

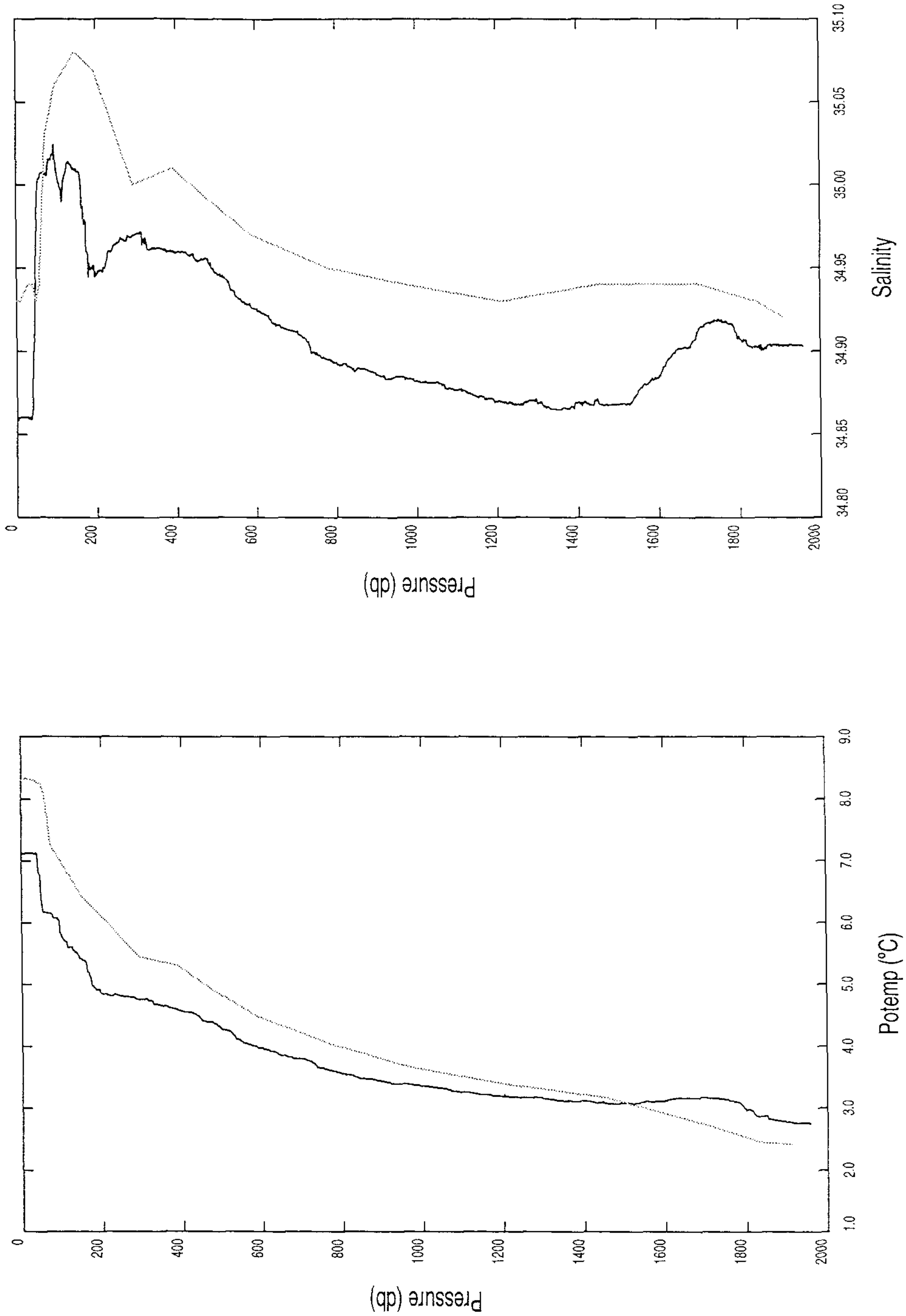

Figure 6.2: Comparison of potential temperature profiles and salinity profiles at CONVEX station 49 and R/V *Anton Dohrn* station 2616. CONVEX profiles are full lines, *Anton Dohrn* profiles faint lines.

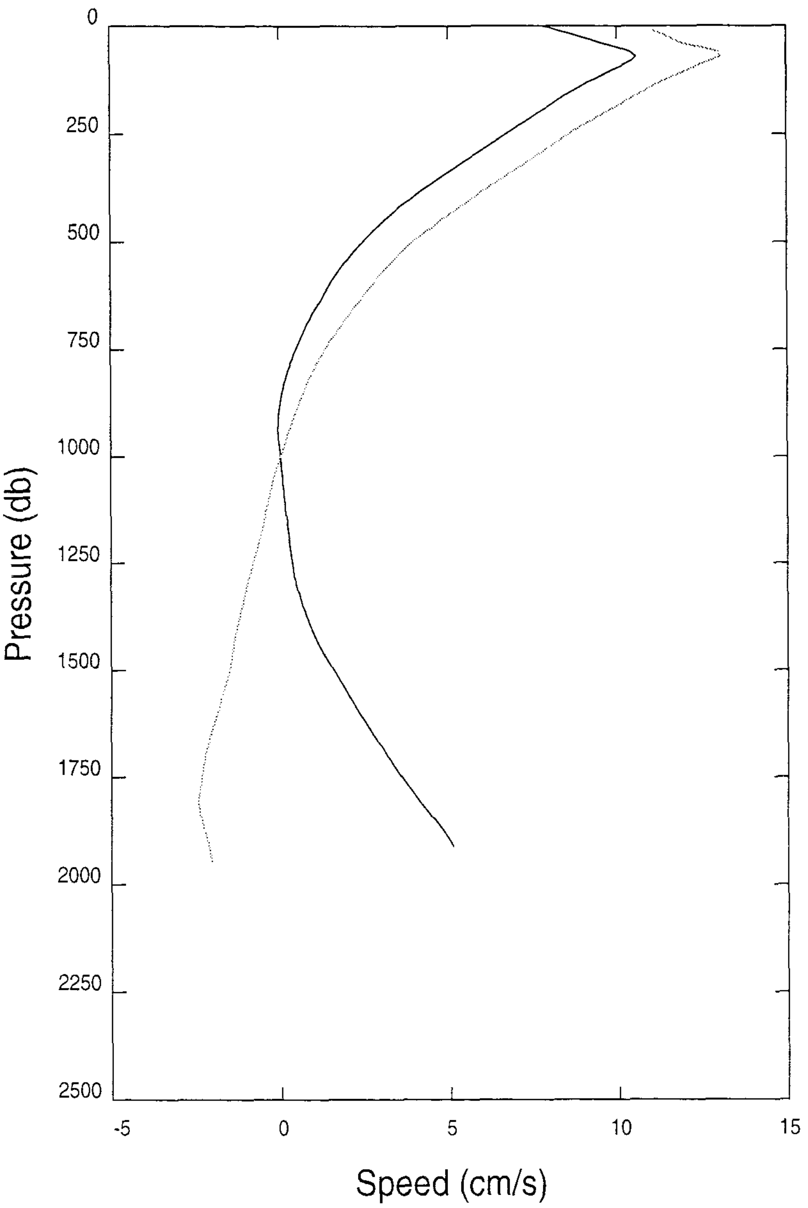

Figure 6.3 (a): Comparison of geostrophic velocity profiles, referenced to zero at 1000 m, formed from *Anton Dohrn* stations 2615 and 2616, and from CONVEX stations 49 and "50–51" (see text for explanation). CONVEX profiles are full lines, *Anton Dohrn* profiles faint lines.

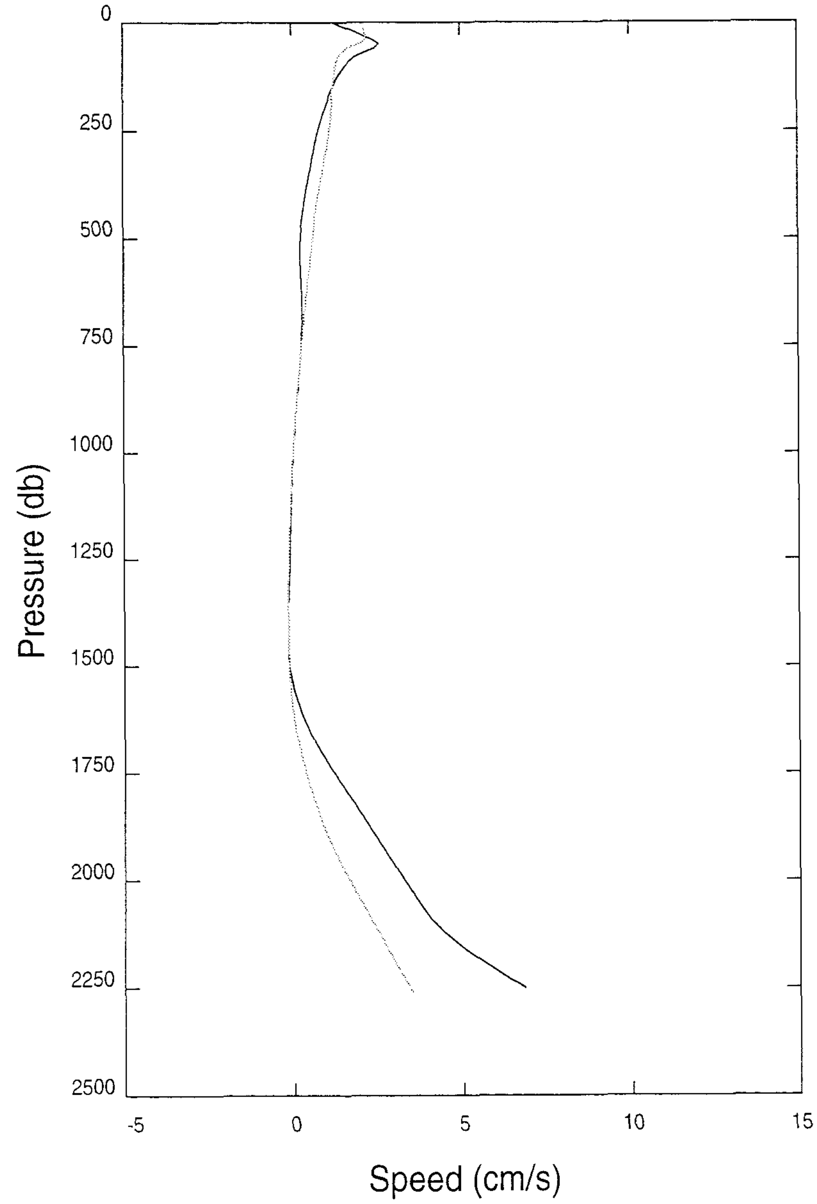

Figure 6.3 (b): Comparison of geostrophic velocity profiles, referenced to zero at 1000 m, formed from *Anton Dohrn* stations 2614 and 2615, and CONVEX stations "50–51" and 52. CONVEX profiles are full lines, *Anton Dohrn* profiles faint lines.

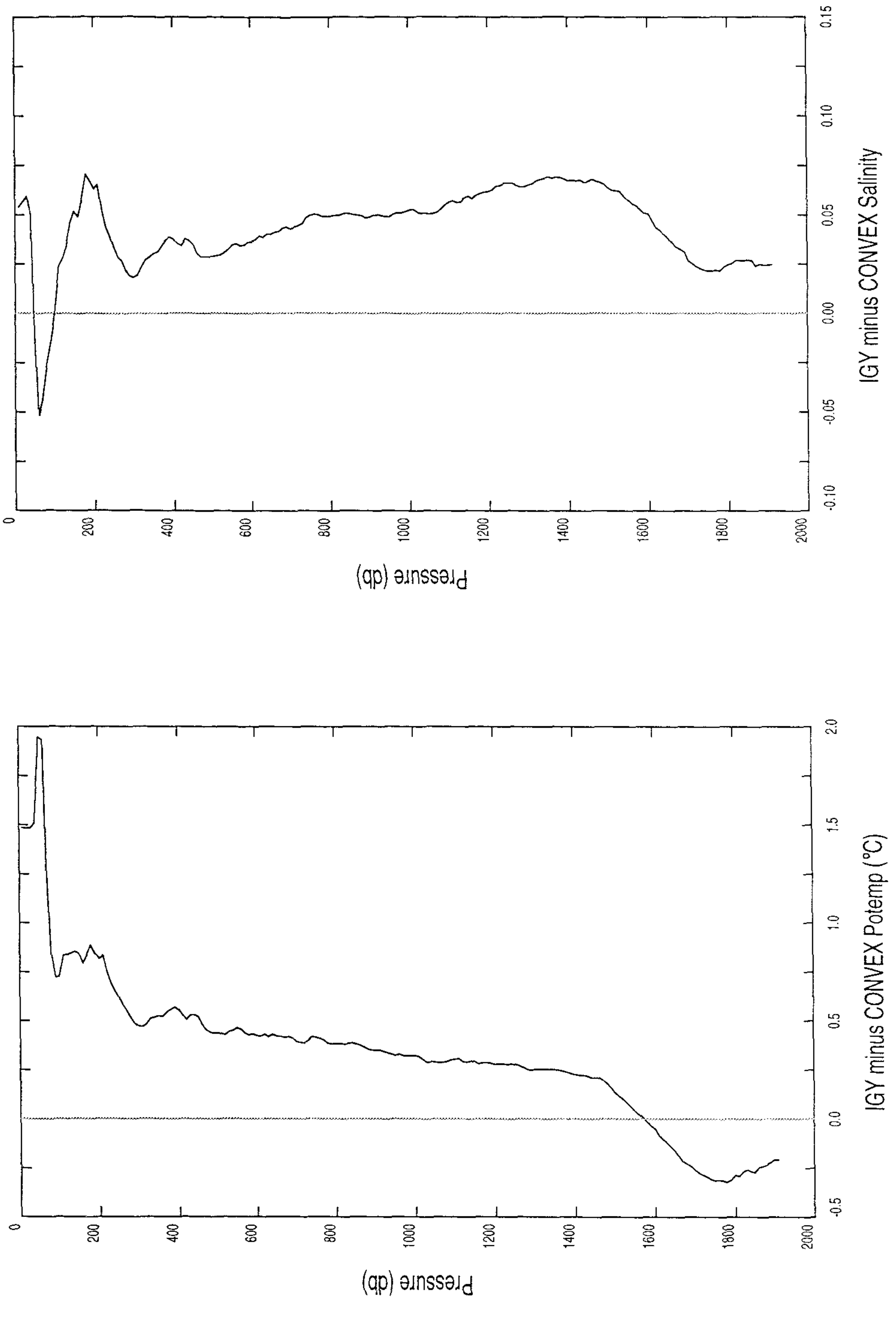

Figure 6.4: Potential temperature and salinity difference profiles. Differences (*Anton Dohrn* minus CONVEX) are calculated between mean property profiles formed from *Anton Dohrn* stations 2615 and 2616, and from CONVEX stations 49 and "50–51" (see text for explanation). Both profiles were averaged / interpolated to 10 m vertical resolution.

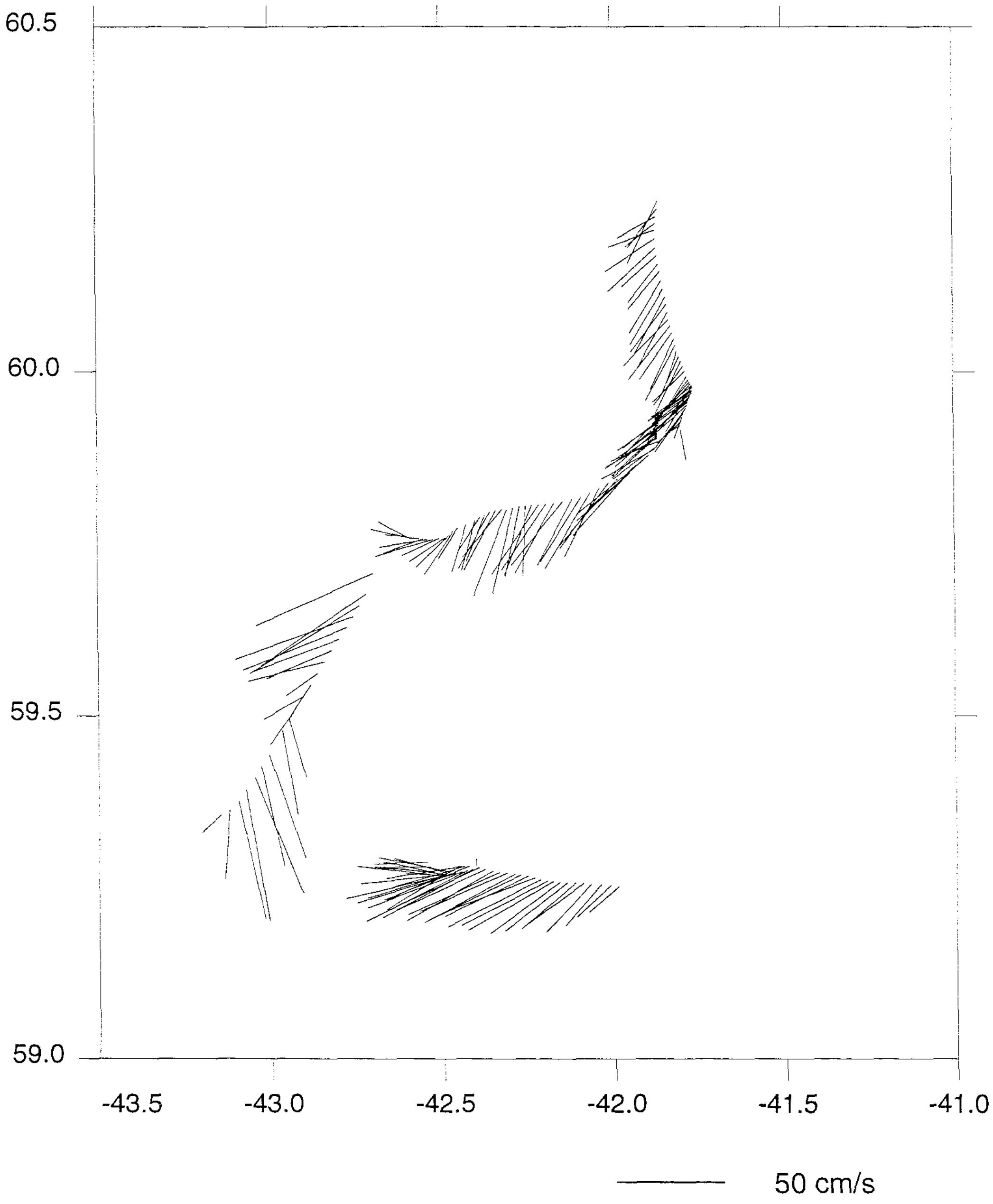

Figure 6.5: ADCP currents in the vicinity of the East Greenland Current. Data shown are of greater than 50 %good, for ship speed less than 2.5 m s^{-1}, at 100 m depth. All good data after and excluding station 47 and before and excluding station 50 are shown.

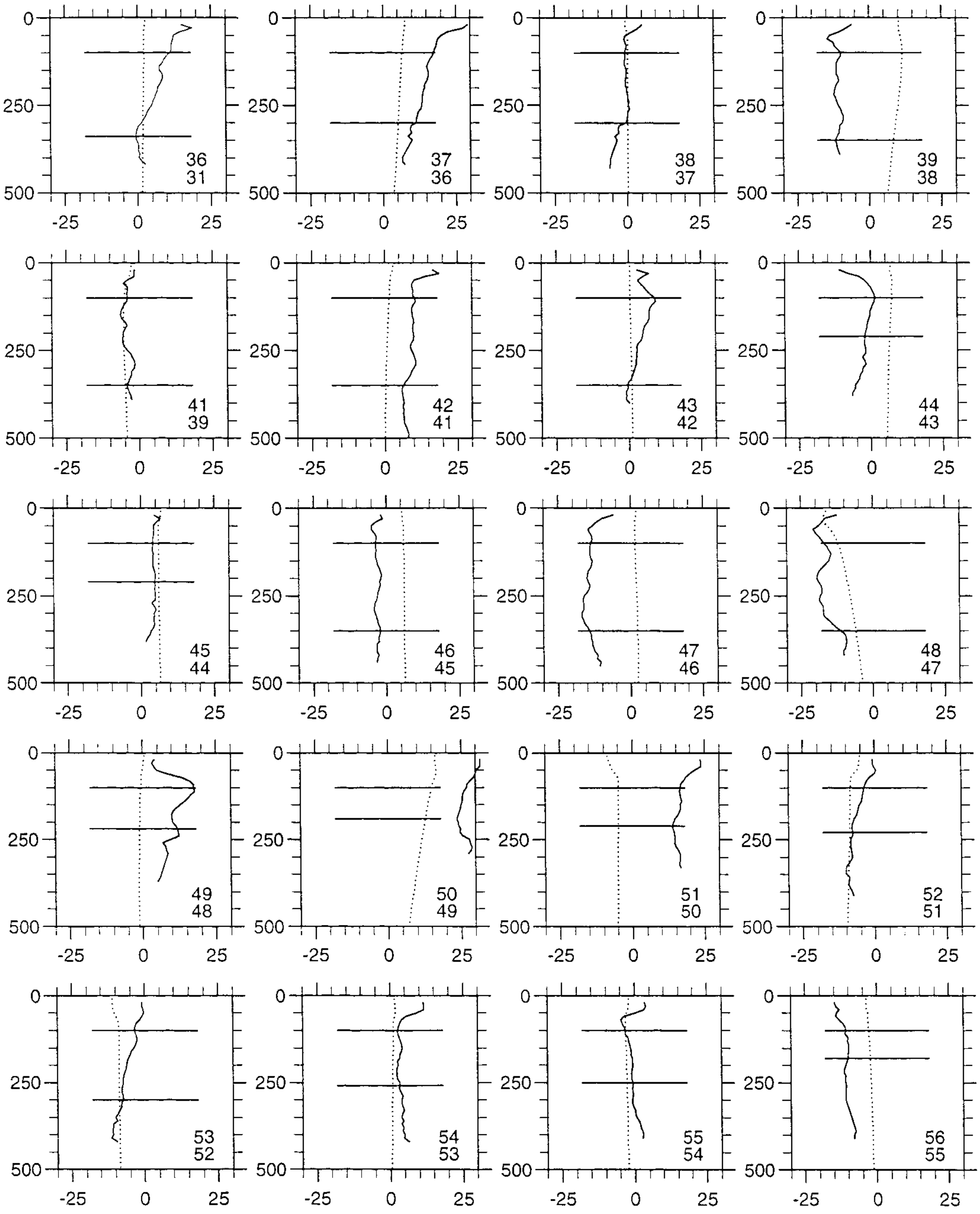

Figure 6.6 (a): ADCP (heavy line) and geostrophic velocity (faint line; referenced to zero at σ_2=36.93) profiles for each station pair for the top 500 m of the water column, with station pair numbers shown and matching range (horizontal bars) for determining offset (ADCP minus geostrophy). Y-axes show pressure (db); x-axes show current speed (cm s^{-1}).

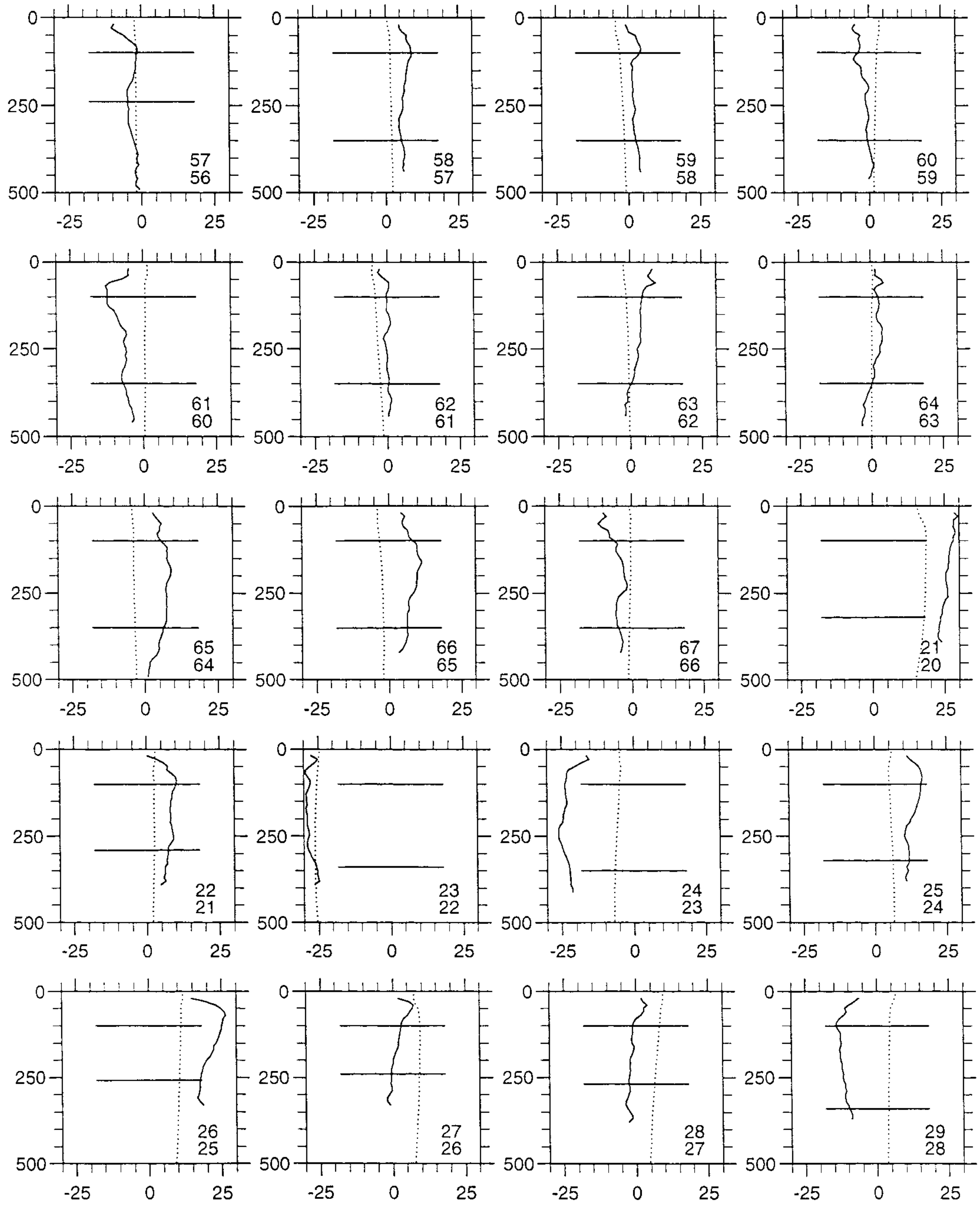

Figure 6.6 (a) continued.

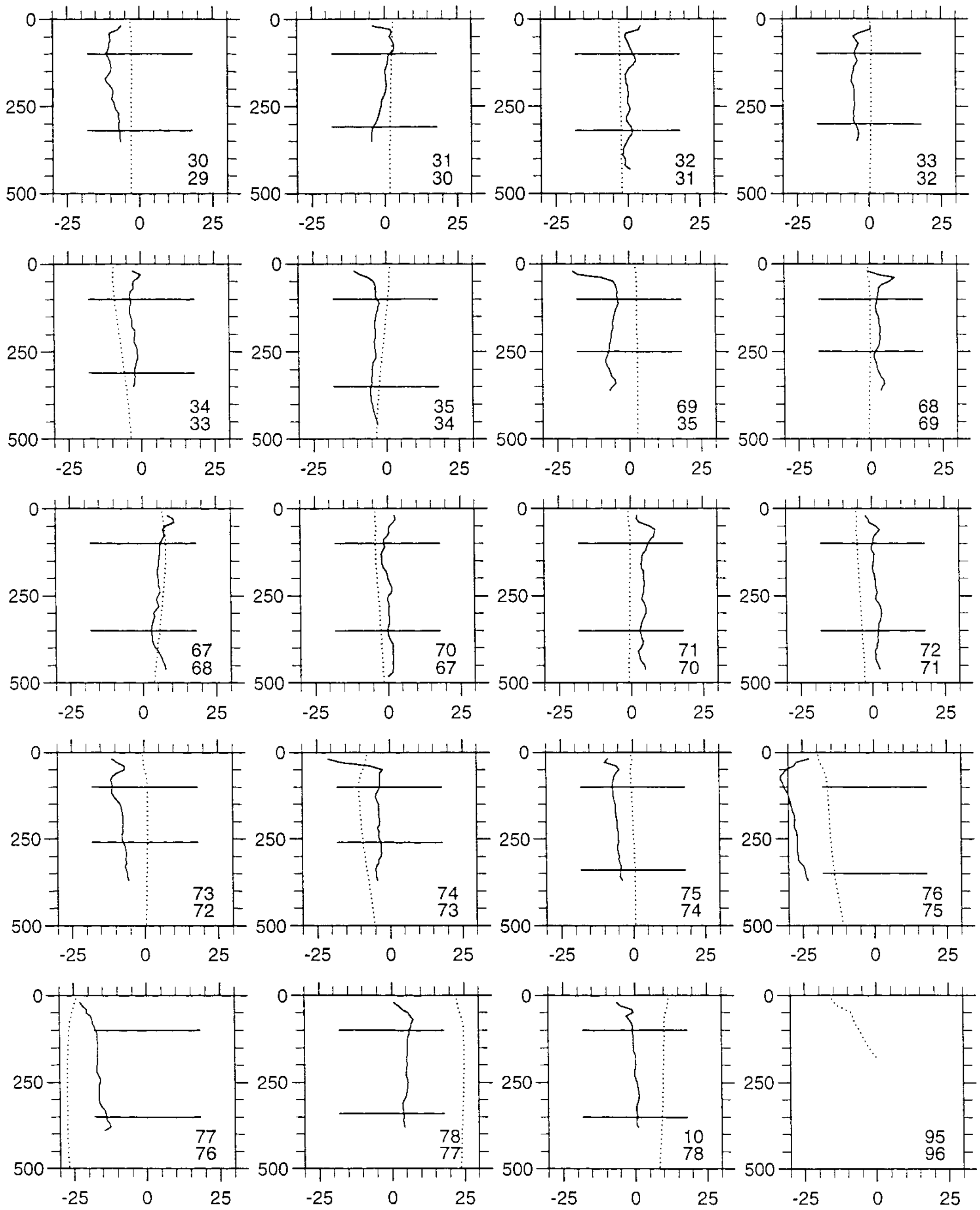

Figure 6.6 (a) continued.

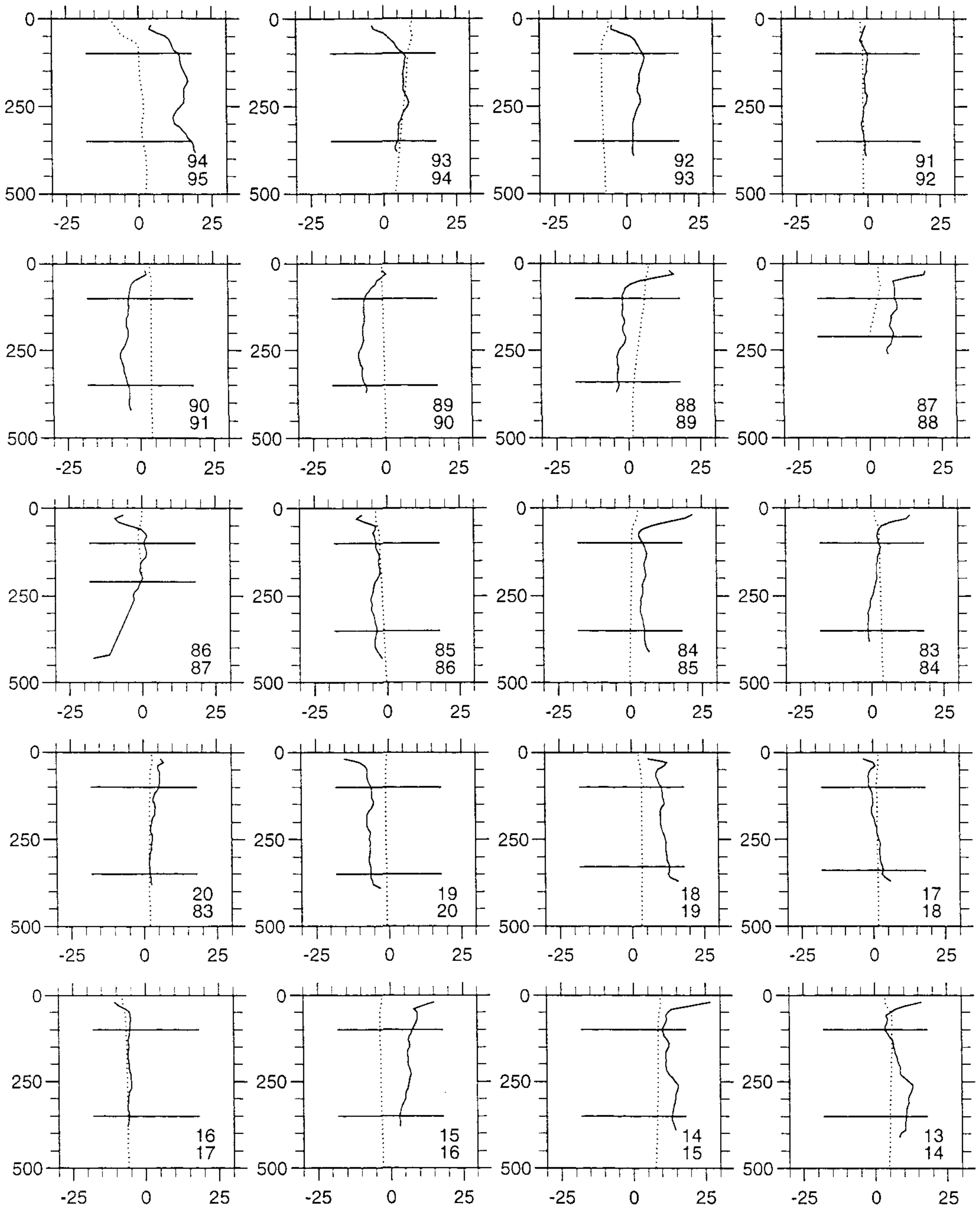

Figure 6.6 (a) continued.

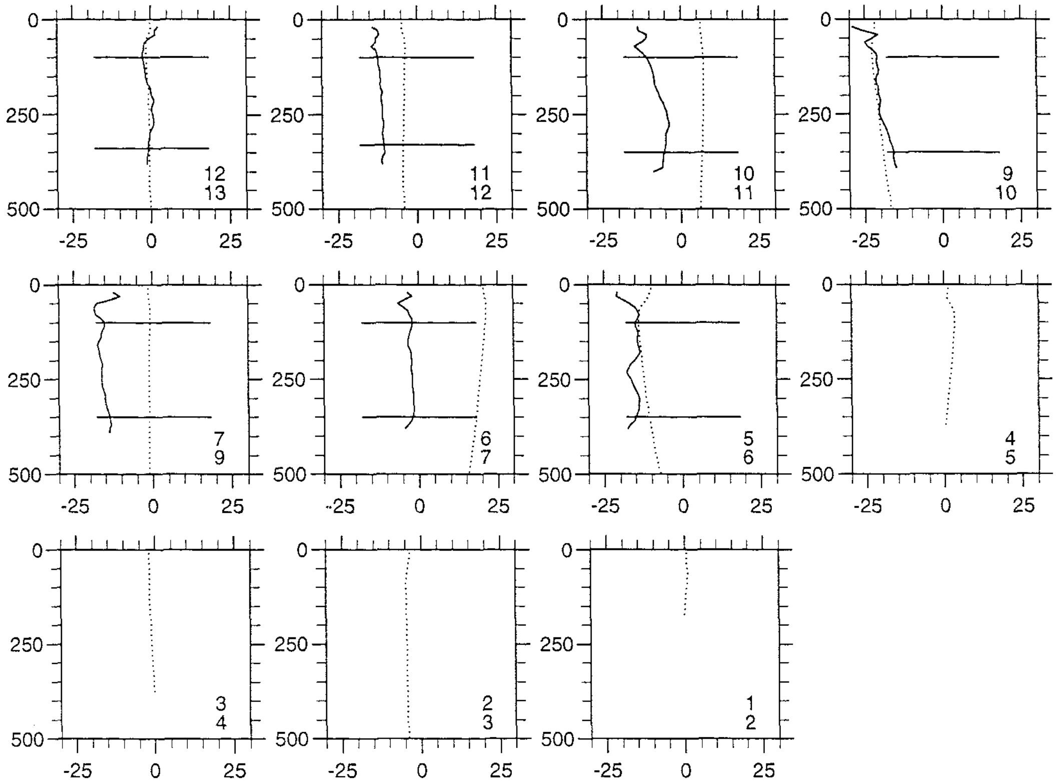

Figure 6.6 (a) continued.

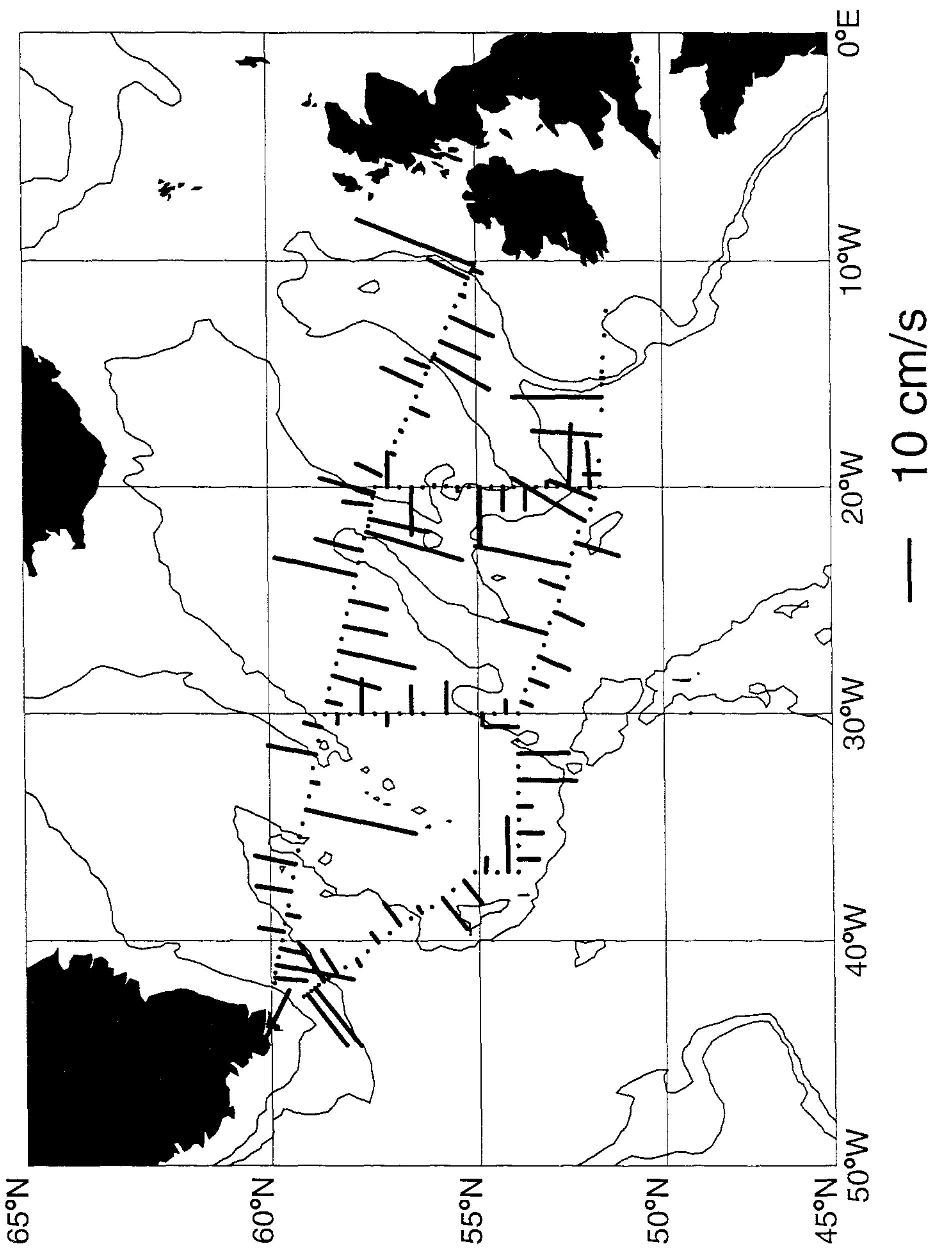

Figure 6.6 (b): Offset (ADCP minus geostrophic current), where the geostrophic current is referenced to zero at σ_2=36.93 and the difference is calculated as the mean between 100 m depth and the depth at which ADCP %good is less than 75%.

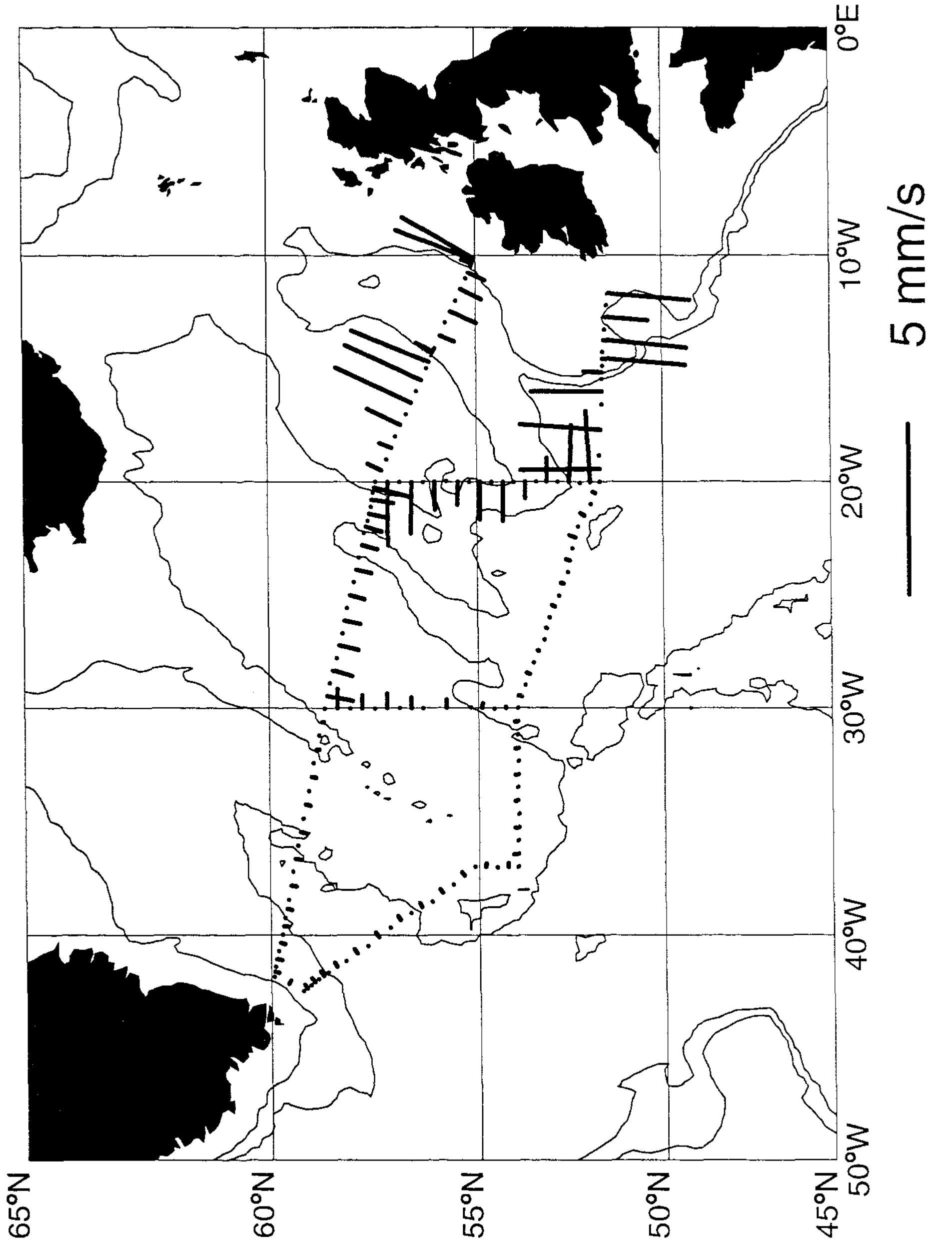

Figure 6.7: Solution vector ($\mathbf{m}^{est}$) for five-layer optimal configuration defined by the surface, σ_0=27.425, σ_2=36.873, 36.944, 37.024, and the bottom, with conservation of volume and salt fluxes in all layers, and heat in all but the top layer, for degree 6; this contributes to State 1 which is used as the reference state.

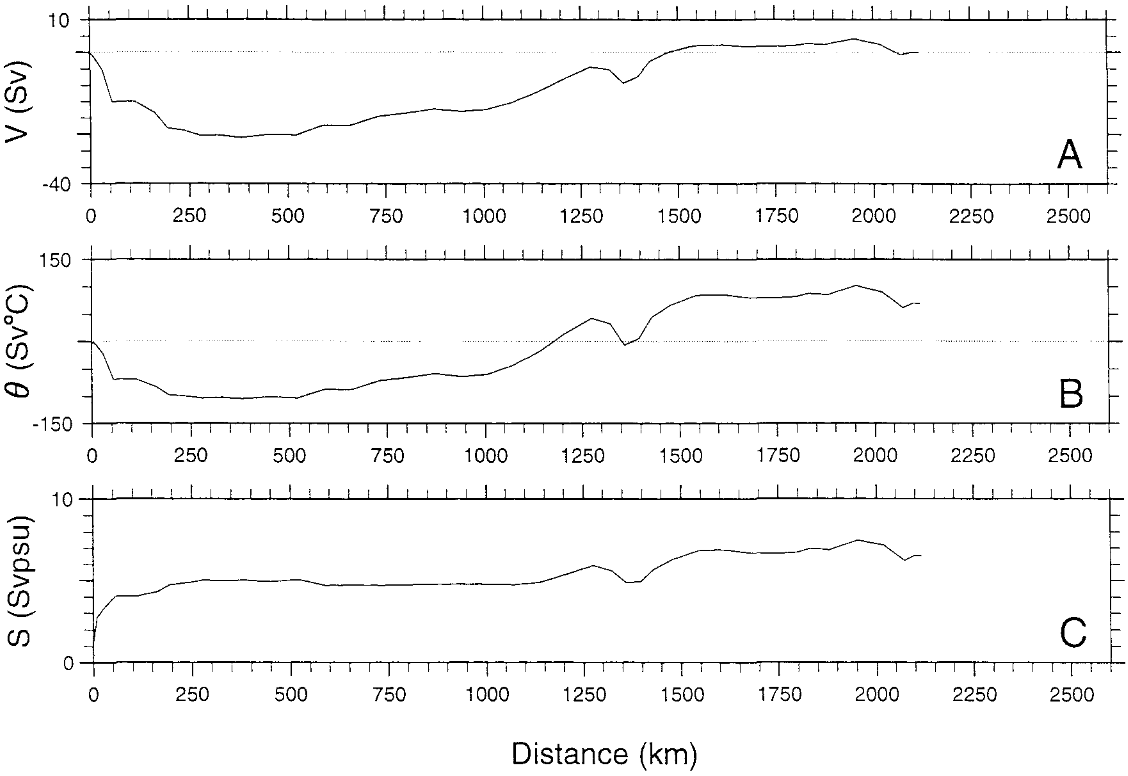

Figure 6.8: Depth-integrated transport for the north section in run 13 (Intermediate; see Table 6.2), accumulated from zero at the west (left), of (A) volume (V, Sv) and (B) potential temperature (θ, Sv°C); and accumulated from 1.1 Svpsu at the west (see section 6.1 for explanation of inshore salt flux), (C) salt (S, Svpsu). Net property flux for the section appears in the easternmost point (the furthest to the right). The faint line is that of zero flux, for reference.

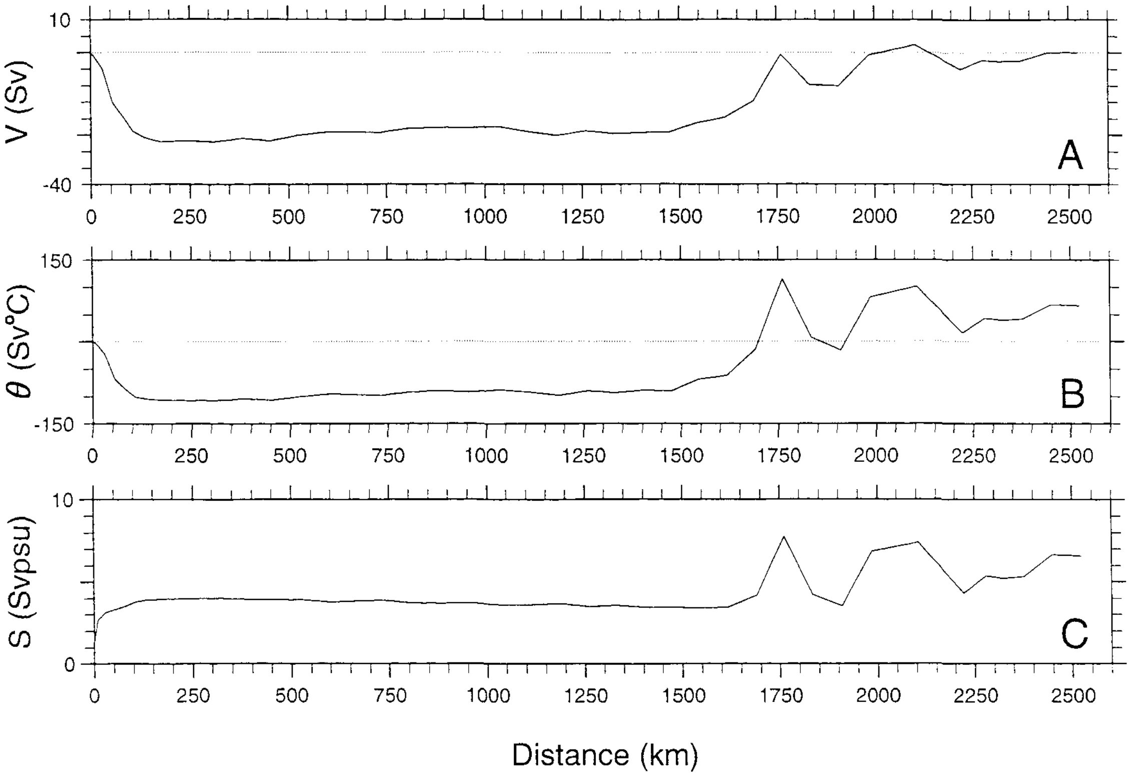

Figure 6.9: Depth-integrated transport for the south section in run 13 (Intermediate; see Table 6.2), accumulated from zero at the west (left), of (A) volume (V, Sv) and (B) potential temperature (θ, Sv°C); and accumulated from 1.1 Svpsu at the west (see section 6.1 for explanation of inshore salt flux), (C) salt (S, Svpsu). Net property flux for the section appears in the easternmost point (the furthest to the right). The faint line is that of zero flux, for reference.

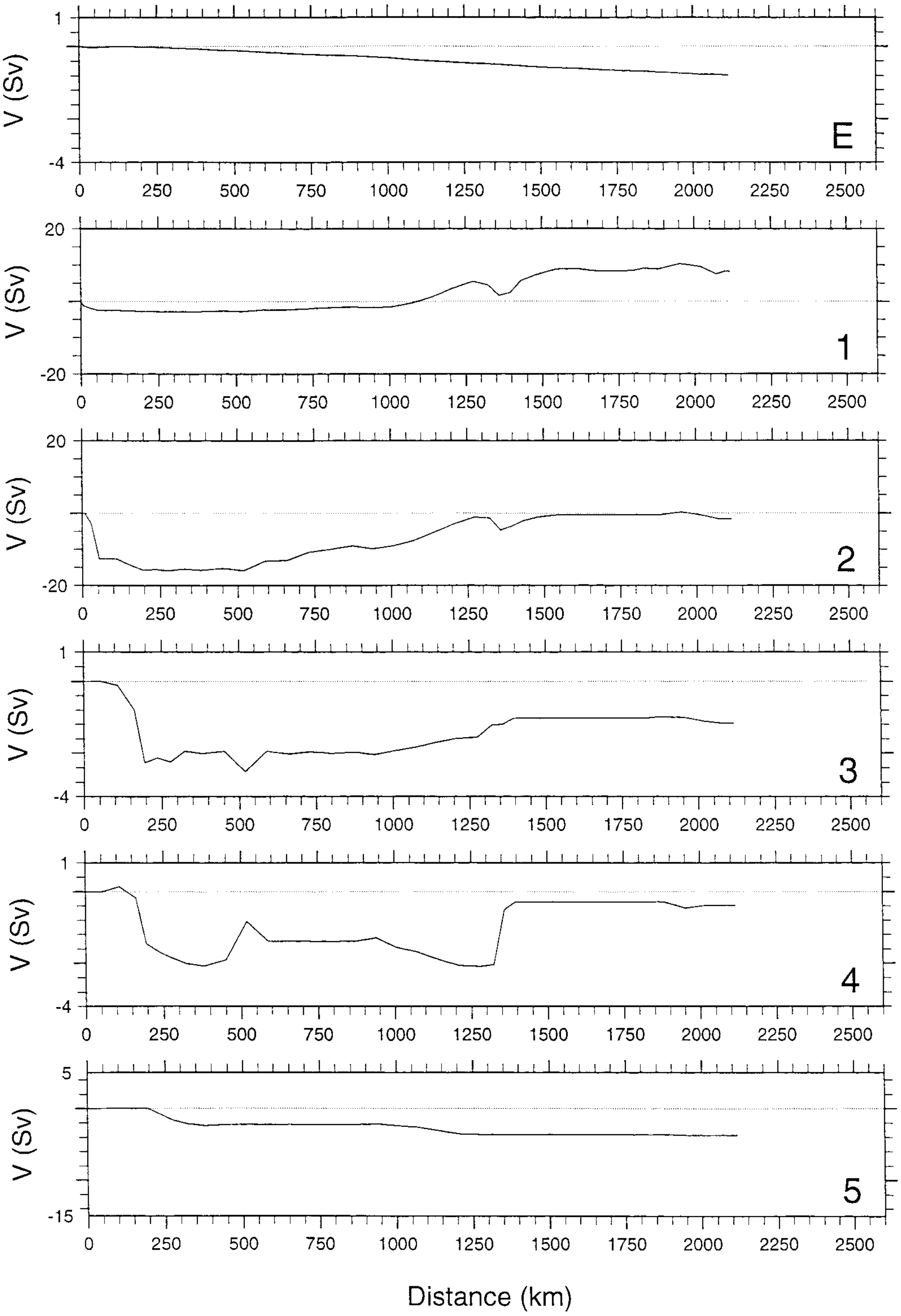

Figure 6.10: Volume transport (Sv) for the north section in run 13 (Intermediate) by layer, accumulated from zero at the west (left), where the first panel (E) is the climatological Ekman flux (Sv), and panels 1-5 correspond to each of the five layers in order. Net volume flux for the Ekman flux or the layer appears in the easternmost point (the furthest to the right).

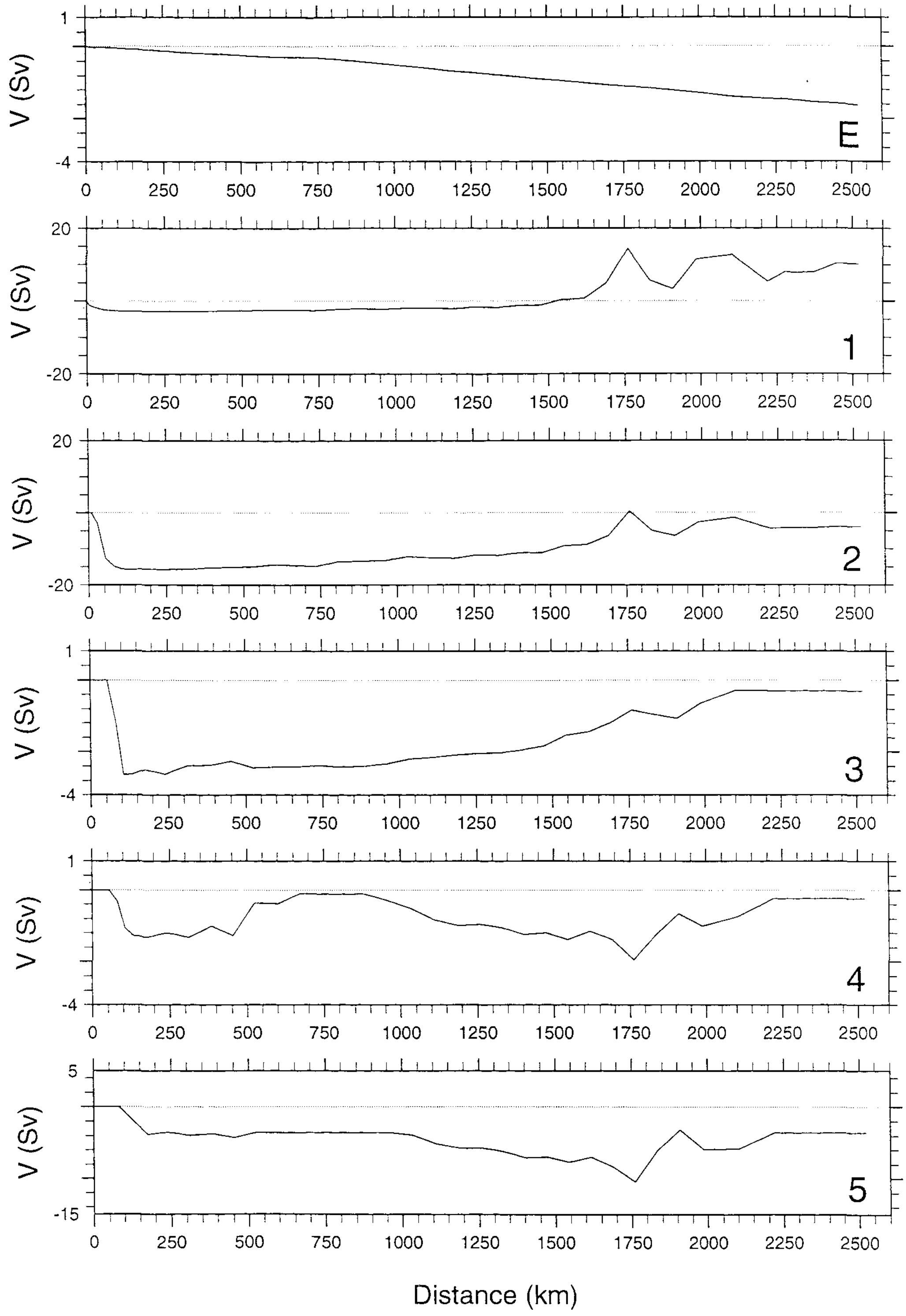

Figure 6.11: Volume transport (Sv) for the south section in run 13 (Intermediate) by layer, accumulated from zero at the west (left), where the first panel (E) is the climatological Ekman flux (Sv), and panels 1-5 correspond to each of the five layers in order. Net volume flux for the Ekman flux or the layer appears in the easternmost point (the furthest to the right).

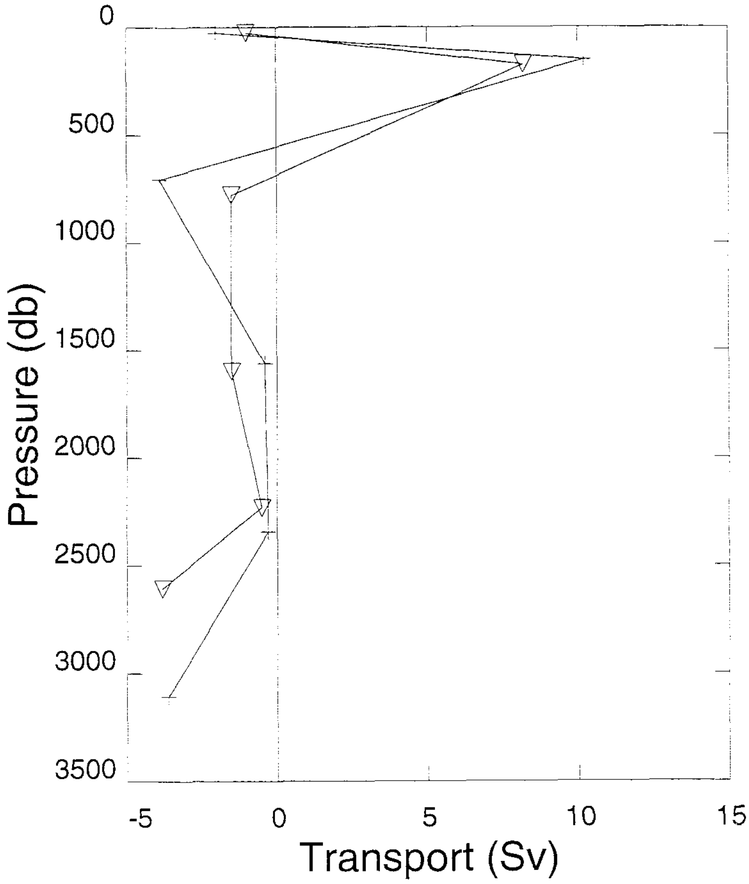

Figure 6.12: Horizontally-integrated transport for run 13 (Intermediate) in the Ekman layer and the five optimal layers; south section marked by plus signs, north section by triangles. Pressure axis constructed from cumulative mean layer thickness.

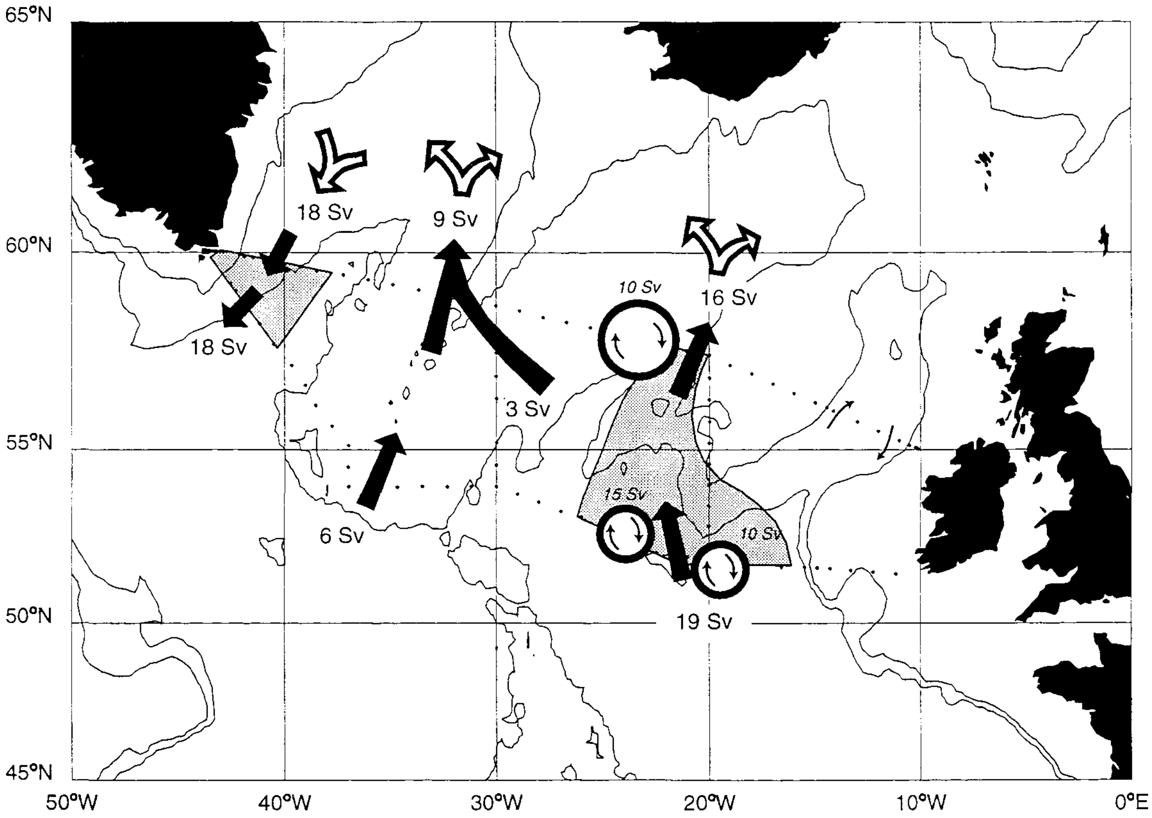

Figure 6.13 (a): Upper circulation sketch, formed from the sum of layers 1 and 2, for run 13 (Intermediate). The rings show approximate sizes, positions and rotational senses of eddies, whose magnitude is given in small italic type. The filled arrows show approximate locations and directions of currents whose magnitude is given in large type. The approximate extent of the southgoing currents in the west is shown shaded, as is the NAC in the east, which is broad in the south and narrower in the north. A small amount appears to join the 'central' recirculation, which is a broad flow filling the region (unshaded) between the western currents and the NAC. Unquantified senses of currents are given north of the CONVEX region (unfilled arrows), and in the Rockall Trough (small arrows), where there is a weak recirculation (probably 1–2 Sv).

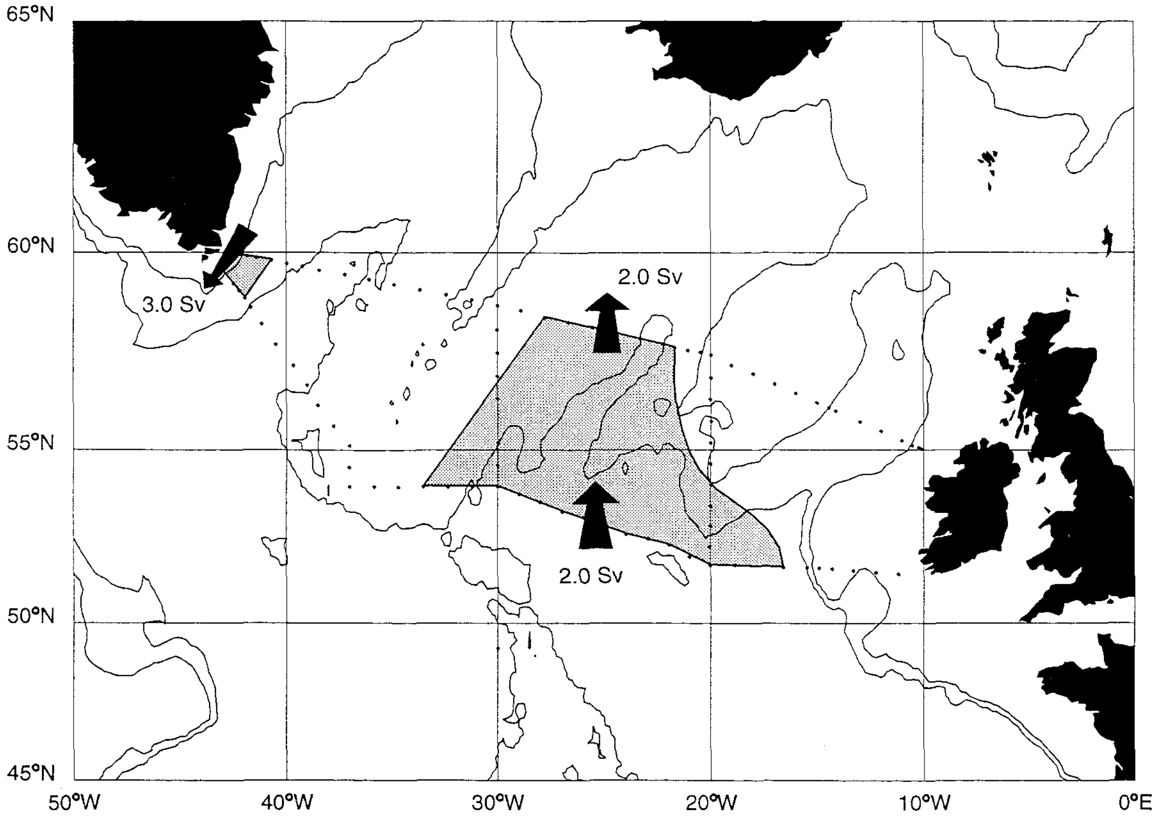

Figure 6.13 (b): Mid-depth (LSW) circulation (layer 3), for run 13 (Intermediate). The approximate lateral extent of the regions of measurable flow are shown shaded. Arrows show flow direction, and associated magnitude is indicated.

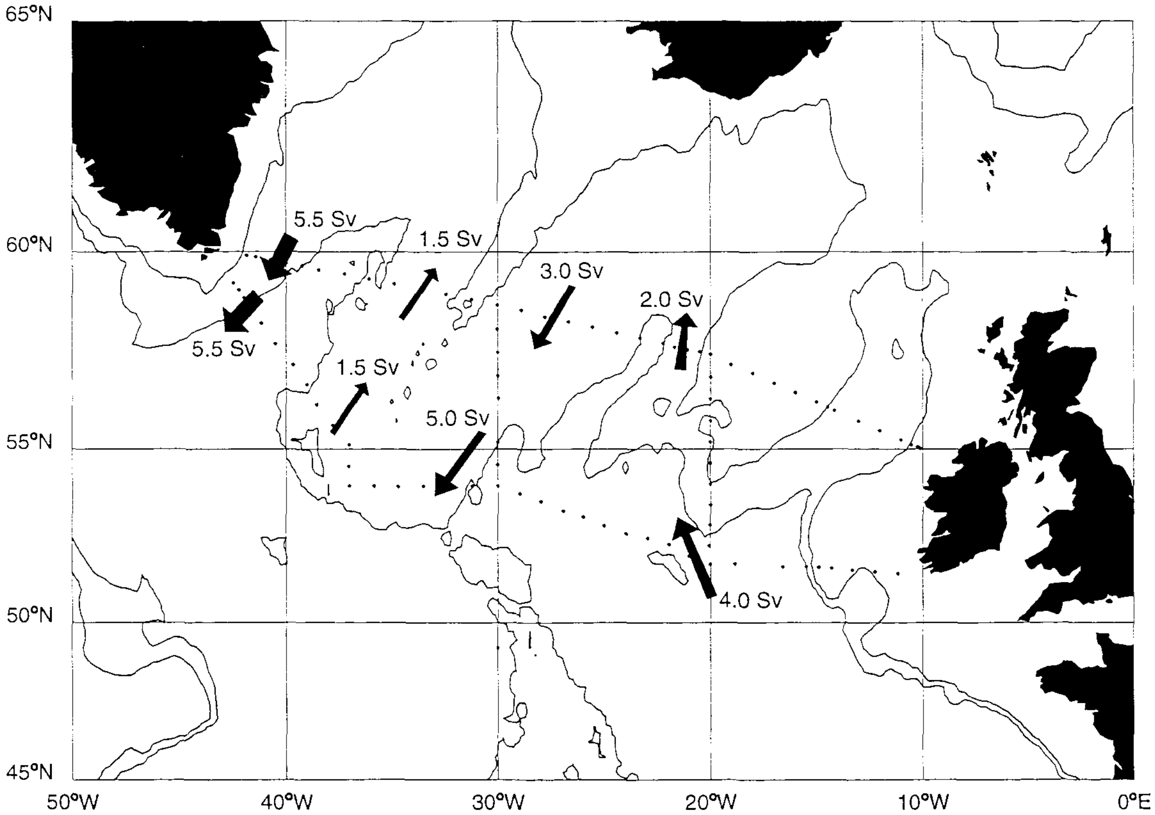

Figure 6.13 (c): Deep circulation sketch, formed from the sum of layers 4 and 5, for run 13 (Intermediate). The Denmark Strait Overflow is shown to the west by Greenland. The 1.5 Sv on the west flank of the Reykjanes Ridge is assumed to have passed through the Charlie-Gibbs Fracture Zone. In the north Madeira Basin and Iceland Basin, half of the northgoing 4 Sv appears to recirculate between the north and south sections, and half north of the CONVEX region. This is supplemented by 1 Sv of Iceland-Scotland Overflow on the east flank of the ridge.

7. FINAL REMARKS

In this final chapter, we use the first section (7.1) to summarise the work of this thesis. In 7.2, we voice a few points to do with the mechanics of inverse methods which we are unable to prove, but which may express some of the idiosyncrasies of a useful data handling method; and finally (7.3), we suggest some directions in which related work may progress.

7.1 Summary

In section 2.2 of the review chapter, we identify an inconsistency in the standard method of calculating oceanic heat fluxes, and suggest a means of rectification. Instead of converting a potential temperature flux to a heat flux by multiplying by *in-situ* specific heat capacity, one should use surface heat capacity. This can be viewed as a matter of consistency. One uses potential temperature referenced to the surface; for thermodynamic purposes, the water parcel has been raised adiabatically to the surface; so it should take the surface value of heat capacity also. There is in 2.2 a more proper mathematical argument to accompany this gloss.

Next in chapters 4 and 5 we set about the inverse method, and two improvements are developed. One enables objective comparison between inversion solution estimates and independent estimates of the solution (ADCP data here), from which there are two benefits: proof of skill in the inversion solution (only the second demonstration of skill as such since inversions arrived on the oceanographic scene in the late '70's); and assistance in selection of solution degree. The other improvement entails the identification and application of a criterion whereby the inversion can be said to be optimal: in essence, selection of layers into which the water column in the study area is divided for the application of flux conservation constraints.

Finally in chapter 6 there is the application of the above to the CONVEX-91 data for the determination of matters of hydrographic interest: net (meridional) fluxes of heat and salt across the region, the circulation of the region, and the freshwater flux of the Arctic Basin. Errors are generally estimated by means of sensitivity studies applied to the hydrographic and inversion-related components of the calculations. It is these net fluxes which are the main results from this thesis, and we conclude this section by showing how the present results fit in with previous work on the transport of heat and freshwater by the Atlantic.

Isemer *et al.* (1987) show their reanalysis of the Bunker heat fluxes, plotted as net meridional heat flux in the North Atlantic from the Equator northwards as their figure 4a, which we reproduce as our figure 7.1, on which we superimpose the CONVEX estimate of 0.28±0.08 PW at 55° N. Our estimate reproduces the values and ranges of Isemer *et al.* rather well. There are three other direct oceanic estimates on the figure. That due to Wunsch (1984) is for the Equator, and is the result of an experiment to produce bounding limits for meridional heat fluxes throughout the North Atlantic. These limits are rather broad over much of the domain, but the Equatorial value is sufficiently narrow to be useful. That due to Hall and Bryden (1982) for 24° N (sometimes referred to as 25° N) is accepted as being carefully done and accurate in mean and error. That due to Rago and Rossby (1987) for 32° N appears both quite high and to have rather low estimates of errors. There appears to be some question over the adequate sampling by the 'Pegasus' technique of the bottom of the water column over the Gulf Stream, meaning (most significantly) possible underestimates of the southward Deep Western Boundary Current. One can see overall that the North Atlantic meridional heat flux is beginning to acquire consistency between surface-derived and direct estimates. This is not (yet) true of the South Atlantic. Saunders and King (1995b) estimate 0.5 PW northward at 40° S (nominal), whereas the latest indirect estimate formed from satellite net fluxes minus atmospheric net fluxes (Trenberth and Solomon, 1994) is about zero.

Wijffels *et al.* (1992) show the results of similar calculations for meridional variation of oceanic freshwater flux, and we reproduce part of their figure 1 as our figure 7.2, on which are superimposed three freshwater flux estimates: $0.95 \pm 0.10 \times 10^9$ kg s^{-1} (CONVEX at 55° N), $0.8 \pm 0.10 \times 10^9$ kg s^{-1} (Hall and Bryden, 1982, at 24° N), and $0.8 \pm 0.10 \times 10^9$ kg s^1 (Saunders and King, 1995b, at 40° S). As

Saunders and King (1995b) remark, it is interesting to note how little oceanic freshwater divergence appears to occur from the direct estimates; the magnitude of the flux is apparently dominated by the Bering Strait throughflow. As in the heat flux case, the major discrepancies lie in the southern hemisphere.

Bryden (1993), in the context of considering total oceanic heat flux (Atlantic plus Pacific) at 24° N, argues that discrepancies between total net heat flux and the available estimates of the atmospheric and oceanic components are likely to be due to errors in atmospheric estimates, or maybe to a bias in satellite radiation measurements. He puts his case succinctly: "to make the ocean contribute an extra 1PW in meridional heat transport across 24° N would require that oceanographers have entirely missed the equivalent of a Gulf Stream in their understanding of ocean circulation. Such myopia is unlikely".

7.2 Impressions

This section is for a few things which seemed worth mentioning about inversions, as a tailpiece. The idea behind inversions is that you start from a point in state space, defined by the 'first guess', which is more or less wrong; the inversion process is then an operator which, ideally, transports one's estimate of the location in state space to the vicinity of the 'right answer'. There is at least one important case, that of shallow barotropic flow such as is found on-shelf and on the shelf-edge of a WBC, where the inversion cannot cope on its own (see section 2.1.7), when the first guess has geostrophic velocities referenced to zero at the bottom. For it to produce an answer which is close to correct, it needs a state which is close to correct to be input. This begs the question, of course, because this is the very reason for one's use of inverse methods: the finding of the 'right answer'. If one lacks *a priori* information on barotropic flows, the inversion is unlikely to discover them. Now we were forced by circumstance to treat the WBC specially in this thesis; and one of the singular aspects of the 24° N Atlantic section is that the WBC (the Gulf Stream) flows not in the open ocean but through a confined channel, the Florida Straits, where it has proved susceptible to frequent measurement. It appears therefore that this point impinges on experiment design: if one wishes to carry out a large-scale ocean section, one must concentrate some effort into making special provision for such areas as the WBC, as Saunders and King (1995a, 1995b) did for their South Atlantic transect. An interesting corollary to this is described by Mercier *et al.* (1993) in their inversion of the whole North Atlantic constrained by float data: such is the speed of the Gulf Stream compared with the mean speed of the interior circulation that individual floats do not reside for long enough within some of their WBC grid boxes for them to be able to assemble in those boxes reliable mean velocities for use as constraints in the inversion!

Returning briefly to consideration of the inversion proper as described in section 6, it was seen therein that the inversion solution did not contribute greatly to the final circulation scheme, because **d** was small (the first guess was nearly non-divergent). The main contribution of the inversion process to the final results was seen in the estimation of the error in the net fluxes due to uncertainty in the reference velocities (the solution vector); the inversion was a good means of producing, under control, differing and plausible reference velocities. The corollary to this observation is that if one requires **d** to be large while still requiring the 'best' (least divergent) first guess, in order to expect significant reference velocities to result from the inversion, one needs to use larger areas of ocean than were employed here, so that significant water-mass transformation may have taken place between inflows and their corresponding outflows in the control volume under consideration. Our reference state in section 6 (state 1) used solution degree 6 from the inversion of a 5-layer set-up, which one can interpret as deriving information from volume constraints in all layers, plus one other, probably derived from salinity, whose distribution is much more different from the density distribution than that of potential temperature. In a larger region, potential temperature and salinity constraints should 'improve' the solution more than was the case here.

My present impression of the inverse method *per se* is that it is the opposite of the back-of-the-envelope calculation. The latter should provide one with order-of-magnitude information, but no subtleties. The former, in contrast, is quite capable of revealing subtleties, but only if started near the right spot, which includes forcing it to go to near the right spot by including measurements, such as of boundary currents, as constraints. Otherwise, one will obtain a small movement from a wrong answer to another, slightly different, wrong answer. I think that the real utility of the method lies not its being any sort of magic recipe for enhancing the useful information content of insufficient data (although it can do that to some extent), but rather in its power to force consistency on asynoptic data: and for the forseeable future, most significant oceanographic data are going to be more or less asynoptic.

7.3 What next?

We produced late in 1994 (Bacon and Bryden, 1994) a highly-graded proposal for shiptime which we hope to carry out in summer of 1996 or 1997 as part of the WOCE resurvey of the North Atlantic. It entails a return to the Sub-Polar Gyre but not, like CONVEX-91, to define its interior circulation, but rather to define the input and output through its boundaries, by reoccupying an IGY section (No. 4; Dietrich, 1969; figure 7.3) from Cape Farewell in Greenland to Cape Finisterre in Spain, and paralleling this with a northern section from Greenland across the Denmark Strait to Iceland, then to Scotland via Rockall. This will enable investigation of transfer of properties between the Sub-Tropical and Sub-Polar Gyres, and between the Sub-Polar Gyre and the Arctic, estimation of inputs to and outputs from the Sub-Polar Gyre, and, of course, the change in the oceanic climate along IGY 4 over nearly 40 years. In the few years since CONVEX-91, various crucial technologies have advanced significantly: particularly in ship's heading and position from satellite data (King and Cooper, 1993; King, Alderson and Cromwell, 1995) which results in improved current estimates from all vessel-mounted acoustic current measurement systems; and in those current measurement systems themselves. In addition to the vessel-mounted ADCP, we now have ADCPs which can be attached to the CTD frame to profile currents from top to bottom in the water column, called Lowered ADCP (LADCP; Fischer and Visbeck, 1993); and a trial instrument, an Acoustic

Correlation Current Profiler (ACCP; Griffiths *et al.*, 1995) which offers the prospect of underway current profiling to depths in excess of 1000 m. We hope that we will be able considerably to sharpen up our estimates of circulation and fluxes thereby.

We also retain an interest in 'performance-testing' of inverse methods on real ocean data, and to that end, we would like to see if we can detect skill in the estimation of vertical fluxes. It seems that a good way to do this would be to try to detect a 'large' signal and to compare it with a 'small' signal, so we might get a 48° N Atlantic section to go with a section like the CONVEX-91 south one, put a meridional boundary in the vicinity of Mid-Atlantic Ridge, and see whether the net effects of the Labrador Sea convection are visible in contrast with the more quiescent eastern basin areas.

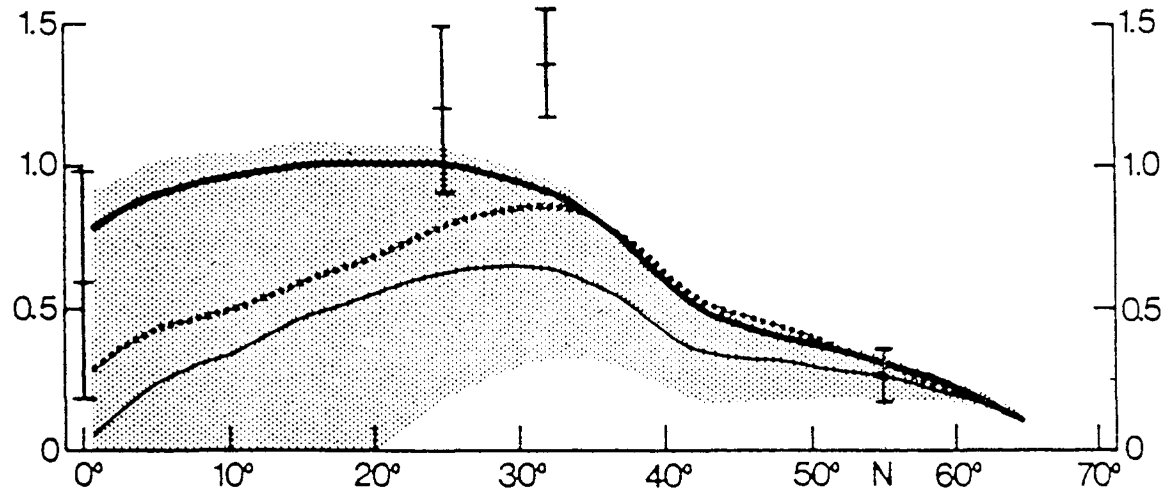

Figure 7.1: Figure 4a from Isemer *et al.* (1987). Meridional oceanic heat transport in PW (W × 10^{15}) as a function of latitude in the North Atlantic. Dotted line: original results of Bunker. Thin line: revised parameterisations of Bunker by Isemer *et al.* Shaded area: range of total rms error of the net air-sea heat exchange according to the uncertainties of the parameters. Solid line: aforementioned revised parameterisations, also including as a constraint that the heat flux at 25° N should be 1.0 PW. Vertical bars give direct estimates plus errors of Wunsch (1984) at the equator, Hall and Bryden (1982) at 25° N and Rago and Rossby (1987) at 32° N. The CONVEX heat flux estimate has been added at 55° N (nominal).

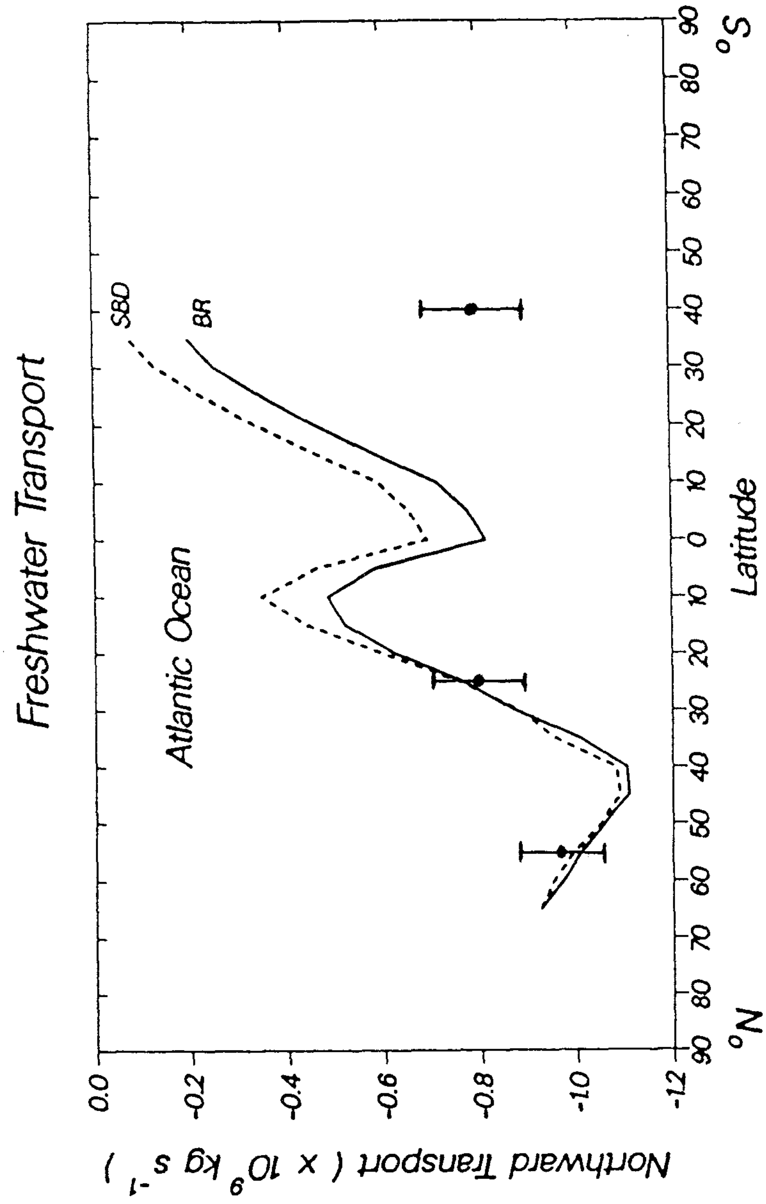

Figure 7.2: Part of figure 1 from Wijffels *et al.* (1992), showing variation of oceanic freshwater flux with latitude in the Atlantic. Superimposed are data from CONVEX at 55° N, Hall and Bryden (1982) at 25° N and Saunders and King (1995b) at 40° S (nominal). BR = Baumgartner and Reichel (1975); SBD = Schmitt, Bogden and Dorman (1989).

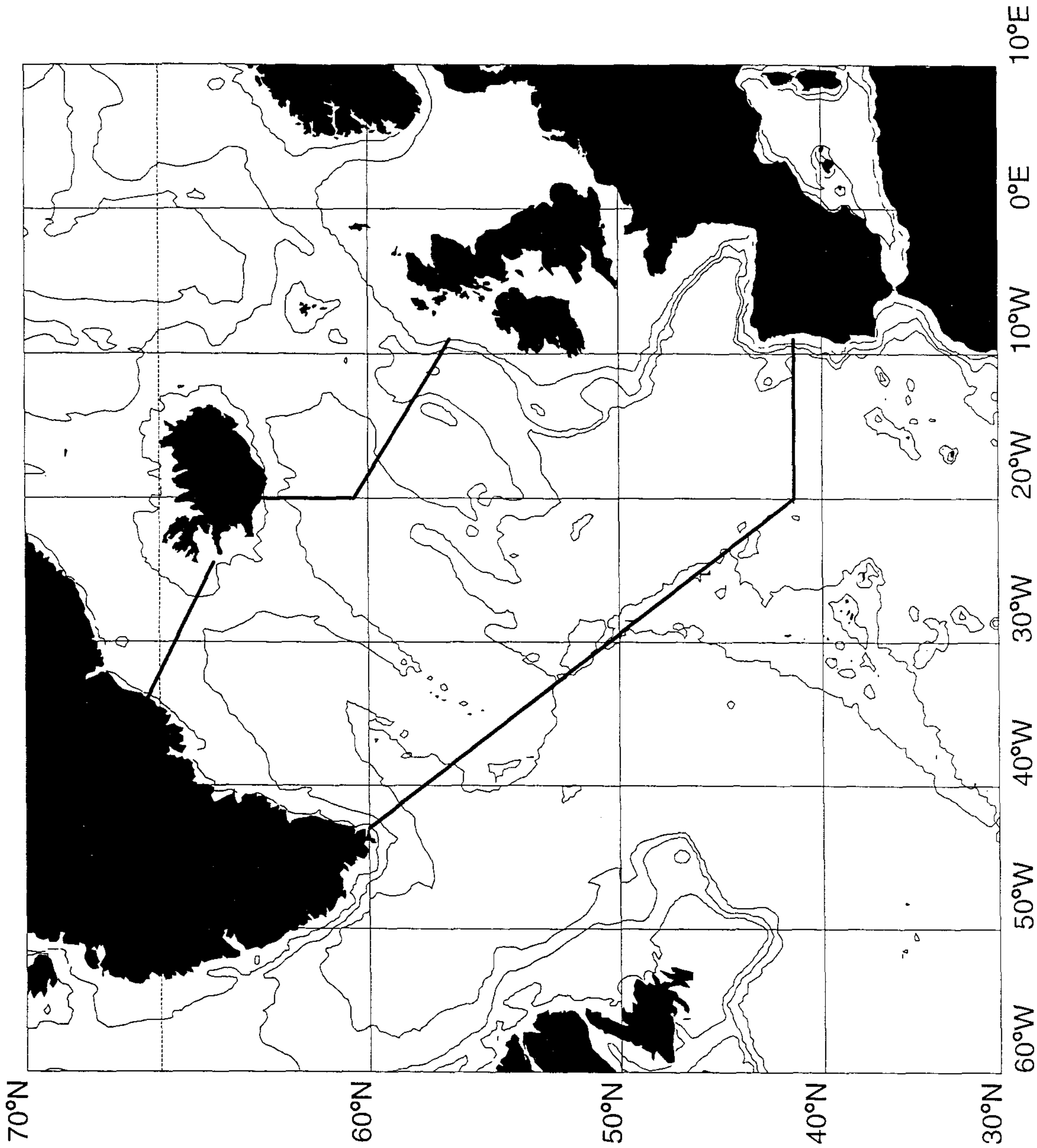

Figure 7.3: Map of North Atlantic, showing IGY Section 4 track (Cape Finisterre, Spain to Cape Farewell, Greenland), Denmark Strait section track and Iceland–Rockall–Scotland section track. Depth contours are 200 m, 1500 m and 3000 m.

NOTE ON PUBLICATIONS

The work reported in this thesis has been prepared concurrently for publication in the refereed press. The titles and author(s) are given below. Reference 1 is based on chapters 3 and 4; reference 2 on chapter 5; reference 3 on chapter 6; and reference 4 chapter 2.2.

1. Bacon, S., 1994: Skill in an inversion solution: CONVEX-91 hydrographic results compared with ADCP measurements. *J. Atmos. Oceanic. Tech.,* **11** (6) 1569-1591.

2. Bacon, S., 1996a: Circulation and fluxes in the North Atlantic between Greenland and Ireland. *J. Phys. Oceanogr., accepted.*

3. Bacon, S., 1996b: Optimising an inversion. *J. Atmos. Oceanic Tech., submitted.*

4. Bacon, S. and N. Fofonoff, 1996: Oceanic heat flux calculation. *J. Atmos. Oceanic Tech.,* in press.

REFERENCES

Aagaard, K. and E. C. Carmack, 1989: The role of sea ice and other fresh water in the Arctic circulation. *J. Geophys. Res.,* **94** , 14485-14498.

Aagaard, K. and P. Greisman, 1975: Toward new mass and heat budgets for the Arctic Ocean. *J. Geophys. Res.,* **80**, 3821-3827.

van Aken, H. M., 1988: Transports of water masses through the Faeroese Channels determined by an inverse method. *Deep-Sea Res.,* **35** (4) 595-617.

van Aken, H. M. and C. J. de Boer, 1995: On the synoptic hydrography of intermediate and deep water masses in the Iceland Basin. *Deep-Sea Res.,* **42** (2) 165-189.

Bacon, S. and H. L. Bryden, 1994: Two Transatlantic Hydrographic Sections Across the Boundaries of the Sub-Polar Gyre. Shiptime proposal (unpublished manuscript); 13 pp. + 4 Annexes + 6 figures.

Backus, G. and F. Gilbert, 1967: Numerical application of a formalism for geophysical inverse problems. *Geophys. J. R. astr. Soc.,* **13** 247-76.

Backus, G. and F. Gilbert, 1968: The resolving power of gross earth data. *Geophys. J. R. astr. Soc.,* **16** 169-205.

Backus, G. and F. Gilbert, 1970: Uniqueness in the inversion of inaccurate gross earth data. *Phil. Trans. R. Soc. Lond.,* **266A** 123-192.

Barth, N. and C. Wunsch, 1990: Oceanographic experiment design by simulated annealing. *J. Phys. Oceanogr.,* **20**, 1249-63.

Batchelor, G. K., 1967: *An Introduction to fluid dynamics.* Cambridge University Press, London, 615 pp.

Baumgartner, A. and E. Reichel, 1975: *The world water balance.* Elsevier, New York, 179 pp.

Bingham, F. M. and L. D. Talley, 1991: Estimates of Kuroshio transport using an inverse technique. *Deep-Sea Res.,* **38**, Suppl. 1, S21-S43.

Broecker, W. S., 1991: The great ocean conveyor. *Oceanography,* **4** (2) 79-89.

Broecker, W. S., T.-H. Peng, J. Jouzel and G. Russell, 1990: The magnitude of global fresh-water transports of importance to ocean circulation. *Climate Dynamics*, **4**, 73-79.

Bryan, K., 1962: Measurements of meridional heat transport by ocean currents. *J. Geophys. Res.*, **67** (9) 3403-3414.

Bryden, H. L., 1993: *Ocean heat transport across 24°N latitude.* AGU Geophysical Monograph 75, 'Interactions between global climate subsystems, the legacy of Hann', ed. G. A. McBean and M. Hantel, pp. 65-75.

Bryden, H. L. and M. M. Hall, 1980: Heat transport across 25°N latitude in the Atlantic Ocean. *Science,* **207**, 884-886.

Bunker, A., 1976: Computations of surface energy flux and annual air-sea interaction cycles of the North Atlantic Ocean. *Monthly Weather Review,* **104**, 1122-1140.

Clarke, R. A., 1984: Transport through the Cape Farewell–Flemish Cap section. *Rapp. P.-v. Réun. Cons. int. Explor. Mer*, **185**, 120-130.

Challenor, P. G. and D. J. T. Carter, 1994: On the accuracy of monthly means. *J. Atmos. Oceanic Tech.,* **11**, 1425-1430.

Coachman, L. K. and K. Aagaard, 1989: Transports through Bering Strait: annual and interannual variability. *J. Geophys. Res.,* **93**, 15535-15539.

Cunningham, S. A. and T. W. N. Haine, 1995: Labrador Sea Water in the eastern North Atlantic. Part I: A synoptic circulation inferred from a minimum in potential vorticity. *J. Phys. Oceanogr.,* **25** (4) 649-665.

Defant, A., 1941: *Die absolute Topographie des physikalischen Meeresniveaus und der Druckflachen sowie die Wasserbewegungen in Raum des Atlantischen Ozeans.* Wissenschaftliche Ergebnisse der Deutschen Atlantischen Expedition auf den Forschungs- und Vermessungsschiff "Meteor" 1925-1927, **6**, 191-260. (In English translation by W.J.Emery, I.D.O.E. and N.S.F.)

Dickson, R. R. and J. Brown, 1994: The production of North Atlantic Deep Water: sources, rates and pathways. *J. Geophys. Res.,* **99** (C6) 12319-41.

Dickson, R. R., E. M. Gmitrowicz and A. J. Watson, 1990: Deep-water renewal in the northern North Atlantic. *Nature* **344** 848-850.

Dietrich, G., 1969: *Atlas of the Hydrography of the northern North Atlantic Ocean, based on the Polar Front survey of the International Geophysical Year, winter and summer 1958.* Conseil International pour l'Exploration de la Mer, Denmark, 140 pp.

Feistel, R., 1993: Equilibrium thermodynamics of seawater revisited. *Prog. Oceanog.*, **31** (2) 101-179.

Fiadero, M. E. and G. Veronis, 1982: On the determination of absolute velocities in the ocean. *J. Mar. Res.*, **40** (supp.) 159-182.

Fiadero, M. E. and G. Veronis, 1983: Circulation and heat flux in the Bermuda Triangle. *J. Phys. Oceanogr.*, **13** (7) 1158-69.

Fischer, J. and M. Visbeck, 1993: Deep velocity profiling with self-contained ADCPs. *J. Atmos. Oceanic Tech.*, **10** (5) 764-773.

Fissel, D. B., D. D. Lemon, H. Melling and R. A. Lake, 1988: *Non-tidal flows in the North-West Passage.* Can. Tech. Rep. Hydrogr. Ocean. Sci. No. 98, IOS, Sidney, B. C., Canada, 143 pp.

Fofonoff, N. P., 1962: Physical properties of sea water. In "The Sea", vol. 1 (M. N. Hill, ed.), pp. 3-30. Wiley, New York.

Fu, L.-L., 1981: The general circulation and heat transport of the subtropical South Atlantic determined by inverse methods. *J. Phys. Oceanogr.*, **11** (9) 1171-1193.

Ghil, M. and P. Malanotte-Rizzoli, 1991: Data assimilation in meteorology and oceanography. *Advances in Geophysics* **33** 141-266.

Gill, A. E., 1982: *Atmosphere-Ocean Dynamics.* Academic Press, San Diego, 662 pp.

Gleckler, P. J. and D. A. Randall, 1995: On the sensitivity of the oceanic meridional heat transport implied by AGCMs to simulated cloud effects. *International WOCE Newsletter,* No. 20, 28-30.

Gloersen, P., W. J. Campbell, D. J. Cavalieri, J. C. Comiso, C. L. Parkinson and H. J. Zwally, 1992: *Arctic and Antarctic sea ice 1978-1987: satellite passive-microwave observations and analysis.* NASA, Washington, 290 pp.

Gould, W. J., 1992: *RRS Charles Darwin Cruise 62 1 August - 4 September 1991. CONVEX - WOCE Control Volume AR12.* IOS DL, Cruise Report, No. 230, 60 pp.

Griffiths, G., B. Dupee, G. Watson, P. Spain and T. Nguyen, 1995: *Trials and evaluation of an RD Instruments Acoustic Correlation Current Profiler in the Agulhas Current on RRS Discovery Cruise 214.* IOS DL, Internal Document, No. 349, 61 pp.

Hall, M. M. and H. L. Bryden, 1982: Direct estimates and mechanisms of ocean heat transport. *Deep-Sea Res.,* **29** (3) 339-359.

Hartman, M. C., 1992: *Shipboard ADCP observations during RRS Charles Darwin Cruise 62.* IOSDL, Report, No. 298, Wormley, 27pp.

Harvey, J. and M. Arhan, 1988: The water masses of the central North Atlantic in 1983-84. *J. Phys. Oceanogr.,* **18**, 1855-75.

Hellerman, S. and M. Rosenstein, 1983: Normal monthly wind stress over the world ocean with error estimates. *J. Phys. Oceanogr.,* **13**, 1093-1104.

Hoerl, A. E. and R. W. Kennard, 1970a: Ridge regression: biased estimation for nonorthogonal problems. *Technometrics* **12** (1) 55-67.

Hoerl, A. E. and R. W. Kennard, 1970b: Ridge regression: applications to nonorthogonal problems. *Technometrics* **12** (1) 69-82.

Huang, R–X., 1993: Real freshwater flux as a natural boundary condition for the salinity balance and thermohaline circulation forced by evaporation and precipitation. *J. Phys. Oceanogr.,* **23**, 2428-2446.

Isemer, H-J., J. Willebrand and L. Hasse, 1989: Fine adjustment of large-scale air-sea energy flux parameterisations by direct estimates of ocean heat transport. *J. Climate,* **2** (10) 1173-1184.

Jackson, D. D., 1972: Interpretation of inaccurate, insufficient and inconsistent data. *Geophys. J. R. astr. Soc.,* **28** 97-109.

Jackson, D. D., 1979: The use of a priori data to resolve non-uniqueness in linear inversion. *Geophys. J. R. astr. Soc.,* **20** 137-157.

Joyce, T. M., C. Wunsch and S. D. Pierce, 1986: Synoptic Gulf Stream velocity profiles through simultaneous inversion of hydrographic and acoustic doppler data. *J. Geophys. Res.,* **91** (C6) 7573-7585.

Killworth, P. D., 1983: Absolute velocity calculations from single hydrographic sections. *Deep-Sea Res.,* **30** (5A) 513-542.

Killworth, P. D., 1986: A Bernoulli inverse method for determining ocean circulation. *J. Phys. Oceanogr.,* **16** 2031-2051.

Killworth, P. D. and G. R. Bigg, 1988: An intercomparison of inverse methods using an eddy-resolving general circulation model. *J. Phys. Oceanogr.,* **18** (7) 987-1008.

King, B. A. and E. B. Cooper, 1993: Comparison of ship's heading determined from an array of GPS antennas with heading from conventional gyrocompass measurements. *Deep-Sea Res.*, **40**, 2207-2216.

King, B. A., S. G. Alderson and D. Cromwell, 1995: Enhancement of shipboard ADCP data with DGPS position and GPS heading measurements. *Deep-Sea Res.*, in press.

Krauss, W., 1995: Currents and mixing in the the Irminger Sea and in the Iceland Basin. *J. Geophys. Res.,* **100** (C6) 10851-10871.

Lanczos, C., 1961: *Linear differential operators.* Van Nostrand, 564 pp.

Lawson, C. L. and R. J. Hanson, 1974: *Solving Least Squares Problems.* Prentice-Hall.

Leetmaa, A., P. Niiler and H. Stommel, 1977: Does the Sverdrup Relation account for the mid-Atlantic circulation? *J. Mar. Res.,* **35** (1) 1-10.

Le Traon, P. Y., M. C. Rouquet and C. Boissier, 1990: Spatial scales of mesoscale variability in the North Atlantic as deduced from Geosat data. *J. Geophys. Res.*, **95**, 20267-20285.

Luyten, J. R. and H. M. Stommel, 1991: Comparison of M2 tidal currents observed by some deep moored current meters with those of the Schwiderski and Laplace models. *Deep-Sea Res.*, **38** (Suppl.1), S573-S590.

Macdonald, A. M., J. Candela and H. L. Bryden, 1994: An estimate of the net heat transport through the Strait of Gibraltar. In *Seasonal and Interannual Variability of the Western Mediterranean Sea*, P. E. La Violette, Ed., Coastal and Estuarine Studies, Vol. 46, American Geophysical Union, 13-32.

Manabe, S. and R. J. Stouffer, 1995: Simulation of abrupt climate change induced by freshwater input to the North Atlantic Ocean. *Nature*, **378** 165-167.

McCartney, M.S. and L. D. Talley, 1984: Warm-to-cold water conversion in the northern North Atlantic Ocean. *J. Phys. Oceanogr.,* **14**, 922-935.

Menke, W. 1989 *Geophysical data analysis: discrete inverse theory.* Academic Press; International Geophysics Ser. **45**.

Mercier, H., 1986: Determining the general circulation of the ocean: a nonlinear inverse problem. *J. Geophys. Res.*, **91** (C4) 5103-5109.

Mercier, H., M. Ollitrault and P. Y. Le Traon, 1993: An inverse model of the North Atlantic general circulation using Lagrangian float data. *J. Phys. Oceanogr.,* **23,** 689-715.

Parker, R. L., 1977: Understanding inverse theory. *Ann. Rev. Earth Planet. Sci.,* **5** 35-64.

Penrose, R., 1955: A generalised inverse for matrices. *Proc. Cambridge Phil. Soc.*, **51**, 406-413.

Pierce, S. D. and T. M. Joyce, 1988: Gulf Stream velocity structure through inversion of hydrographic and acoustic doppler data. *J. Geophys. Res.*, **93**, 2227-2236.

Pollard, R. T., 1970: On the generation by winds of inertial waves in the ocean. *Deep-Sea Res.*, **17**, 795-812.

Pollard, R. T. and J. F. Read, 1990: A method for calibrating shipmounted Acoustic Doppler Profilers and the limitations of gyro compasses. *J. Atmos. Oceanic Tech.* **6**, 859-865.

Rago, T. A. and H. T. Rossby, 1987: Heat transport into the North Atlantic Ocean north of 32° N latitude. *J. Phys. Oceanogr.,* **17** (7) 854-871.

Rahmstorf, S., 1994: Rapid climate transitions in a coupled ocean-atmosphere model. *Nature*, **372** 82-85.

Rahmstorf, S., 1995: Bifurcations of the Atlantic thermohaline circulation in response to changes in the hydrological cycle. *Nature,* **378** 145-149.

Read, J. F. and W. J. Gould, 1992: Cooling and freshening of the subpolar North Atlantic Ocean since the 1960s. *Nature*, **360** (6399) 55-57.

Reid, J. L., 1994: On the total geostrophic circulation of the North Atlantic Ocean: flow patterns, tracers, and transports. *Prog. Oceanog.*, **33**, 1-92.

Richardson, P. L., 1977: On the crossover between the Gulf Stream and the Western Boundary Undercurrent. *Deep-Sea Res.*, **24**, 139-159.

Roemmich, D., 1980: Estimation of meridional heat flux in the North Atlantic by inverse methods. *J. Phys. Oceanogr.*, **10**, 1972-83.

Roemmich, D. and C. Wunsch, 1985: Two transatlantic sections: meridional circulation and heat flux in the subtropical North Atlantic Ocean. *Deep-Sea Res.*, **32** (6) 619-664.

Saunders, P. M., 1982: Circulation in the eastern North Atlantic. *J. Mar. Res.*, **40** (supp.), 641-657.

Saunders, P. M., 1994: The flux of overflow water through the Charlie-Gibbs Fracture Zone. *J. Geophys. Res.,* **99** (C6) 12343-55.

Saunders, P. M. and B. A. King, 1995a: Bottom currents derived from a shipborne ADCP on WOCE cruise A11 in the South Atlantic. *J. Phys. Oceanogr.*, **25** (3) 329-347.

Saunders, P. M. and B. A. King, 1995b: Oceanic fluxes on the WOCE A11 section. *J. Phys. Oceanogr.,* **25** (9) 1942-1958.

Schmitt, R. W., P. S. Bogden and C. E. Dorman, 1989: Evaporation minus precipitation and density fluxes for the North Atlantic. *J. Phys. Oceanogr.,* **19** (9) 1208-1221.

Schmitz, W. J., Jr., 1976: Observation of a new abyssal current. *Geophys. Res. Lett.*, **3**, 373-374.

Schmitz, W. J. and M. S. McCartney, 1993: On the North Atlantic circulation. *Rev. Geophys.,* **31**, 29-49.

Schwiderski, E. W., 1979: Global Ocean Tides, Part II. The semidiurnal principal lunar tide (M_2). Atlas of tidal charts and maps. Naval Surface Weapons Center, Dahlgren, Virginia, Technical Report TR 79-414, 87pp.

Sherliker, P., in prep.: The Bernoulli Inverse method. Ph. D. Thesis, Oxford University.

Stephens, G. L., G. G. Campbell and T. H. Vonder Haar, 1981: Earth radiation budgets. *J. Geophys. Res.,* **86** (C10) 9739-9760.

Stommel, H., 1965: *The Gulf Stream: A physical and Dynamical Description.* Cambridge University Press, 248pp.

Schott, F. and H. Stommel, 1978: Beta spirals and absolute velocities in different oceans. *Deep-Sea Res.,* **25** (11) 961-1010.

Scripps Institution of Oceanography, 1986: Transient Tracers in the Ocean, North Atlantic Study, 1 April - 19 October 1981, Shipboard Physical and Chemical Data Report. Scripps Institution of Oceanography Report, SIO Reference 86-15, 714 pp. and appendix.

Talley, L. D. and M. S. McCartney, 1982: Distribution and circulation of Labrador Sea water. *J. Phys. Oceanogr.,* **12** (11) 1189-1205.

Thompson, R. O. R. Y. and G. Veronis, 1980: Transport calculations in the Tasman and Coral Seas. *Deep-Sea Res.*, **27**, 303-323.

Trenberth, K. E. and A. Solomon, 1994: The global heat balance: heat transports in the atmosphere and ocean. *Climate Dynamics,* **10** (3) 107-134.

Webster, P. J., 1994: The role of hydrological processes in ocean-atmosphere interactions. *Rev. Geophys.,* **32** (4) 427-476.

Wells, N., 1986: *The atmosphere and ocean: a physical introduction.* London: Taylor and Francis, 347 pp.

WCRP, 1988a: *World Ocean Circulation Experiment Implementation Plan, I: Detailed requirements.* WOCE IPO, Wormley.

WCRP, 1988b: *World Ocean Circulation Experiment Implementation Plan, II: Scientific Background.* WOCE IPO, Wormley.

Wiggins, R., 1972: The general linear inverse problem: implications of surface waves and free oscillations on earth structure. *Rev. Geophys. Space Phys.,* **10** 251.

Wijffels, S. E., R. W. Schmitt, H. L. Bryden and A. Stigebrandt, 1992: Transport of freshwater by the oceans. *J. Phys. Oceanogr.,* **22** (2) 155-162.

Worthington, L. V. and W. R. Wright, 1970: *North Atlantic Ocean Atlas of potential temperature and salinity in the deep water including temperature, salinity and oxygen profiles from the Erika Dan cruise of 1962.* Woods Hole Oceanographic Institution Atlas Series 2: 24 pp. and 58 plates.

Wunsch, C., 1972: The spectrum from two years to two minutes of temperature fluctuations in the main thermocline at Bermuda. *Deep-Sea Res.,* **19** 577-593.

Wunsch, C., 1978: The North Atlantic circulation west of 50°W determined by inverse methods. *Rev. Geophys.,* **16**, 583-620.

Wunsch, C., 1984: An eclectic Atlantic Ocean circulation model. Part I: The meridional heat flux. *J. Phys. Oceanogr.,* **14** (11) 1712-1733.

Wunsch, C., 1986: Reply. *J. Phys. Oceanogr.,* **16** , 1731-2.

Wunsch, C. and B. Grant, 1982: Towards the general circulation of the North Atlantic Ocean. *Prog. Oceanog.,* **11** 1-59.

Wunsch, C. and D. Roemmich, 1982: On combining satellite altimetry with hydrographic data. *J. Mar. Res.,* **40** (supp.) 605-619.

Wunsch, C., D. Hu and B. Grant, 1983: Mass, heat, salt and nutrient fluxes in the South Pacific Ocean. *J. Phys. Oceanogr.,* **13** (5) 725-753.

Wüst, G. 1935 *Schichtung und Zirkulation des Atlantischen Ozeans. Die Stratosphäre.* Wissenschaftliche Ergebnisse der Deutschen Atlantischen Expedition auf den Forschungs- und Vermessungsschiff "Meteor" 1925-1927, **6**, Parts 1, 2, 180pp. (In English translation by W. J. Emery, I.D.O.E. and N.S.F.)